Masterarbeit

Zur Erlangung des akademischen Grades Master of Science
Global Change Geography

Spectral features of Earth's Atmosphere in Observations
- Strengths, Limits, Applications and Side Benefits of an Empirical Correction Method from an interdisciplinary perspective

Eingereicht von: Joana Wokittel
Matrikel-Nummer: 566457
Eingereicht am: 26.07.2023

Gutachter/innen: Prof. Dr. Tobias Sauter
                     Klimatologie, Geographisches Institut, Humboldt-Universität zu Berlin

                     Prof. Dr. Katja Poppenhäger
                     Stellare Physik und Exoplaneten, Leibniz-Institut für Astrophysik Potsdam

                     Dr. Rene Preusker
                     Strahlung und Fernerkundung, Meteorologisches Institut,
                     Freie Universität zu Berlin

Eingereicht am Geographischen Institut der Humboldt-Universität zu Berlin
Mathematisch-Naturwissenschaftliche Fakultät

Abstract

The Correction for spectral absorption features from Earth's atmosphere is a key part of observations with Earth Observation satellites, or with ground-based Astrophysical Telescopes. This requires either a robust knowledge of Earth's atmospheric constituents for model-based correction approaches. This is challenging especially for the spatially and temporally highly variable atmospheric water vapor concentrations. This study investigates an Empirical Correction approach based on the inherently different behavior of the spectral features in a time series of observations. The suggested method normalises for the expected temporal trends with a Univariate Smoothing Spline Interpolation. The method is applied to ground-based astrophysical spectroscopic observations of a stellar system that hosts the exoplanet HD 189733b. The efficiency of the method to remove Earth's transmission features is quantified in this Thesis from (i) the astrophysical perspective, by retrieving an artificial benchmark signal that was hidden in the observations, and from (ii) the perspective of Earth Observation and Atmospheric Sciences, with regard to future reciprocal effects. The Thesis uses a multitude of atmospheric data bases to establish the atmospheric properties. This Thesis makes use of simulated transmission spectra provided by TAPAS. The comparison of the temporal trend of the simulations to the trend of the available atmospheric data, and to the trend of the observed astrophysical spectra provided a meaningful analysis interface. The spectral features from Earth's atmosphere could be removed effectively, and the comparison can indeed provide reciprocal benefits for Earth Observation and Atmospheric Sciences; the Correction method also yielded good results from the astrophysical perspective by removing the contaminating features and simultaneously leaving enough of the target's spectral features for analysis. These results were quantified for different test scenarios.

Zusammenfassung

Die spektralen Spuren von Absorption in der Erdatmosphäre müssen aus Beobachtungen herauskorrigiert werden, dies gilt für Erdbeobachtung mit Satelliten wie für astrophysikalische Beobachtung mit bodengebundenen Teleskopen. Modell-basierte Korrekturmethoden brauchen robuste Atmosphärendaten, was vor allem für örtlich und zeitlich variable Bestandteile wie atmosphärischer Wasserdampf schwierig ist. Diese Thesis nutz eine rein empirische Methode, die das grundlegend unterschiedliche Verhalten von Spektrallinien verschiedenen Ursprungs in einer Zeitreihe von Beobachtungen untersucht und sie so unterscheidet. Der zeitlich Trend wird mit einer Univariaten Spline Interpolation geglättet und normalisiert. Angewandt wird die Methode auf astrophysikalische Beobachtungen eines Sternsystems, in dem sich ein Exoplanet befindet. Der Erfolg der Methode wird aus zwei Perspektiven quantifiziert: der astrophysikalischen damit, ob ein verstecktes künstliches Signal rekonstruiert werden kann, und der Perspektive der Erdbeobachtung und Atmosphärenwissenschaft im Hinblick auf zukünftige wechselseitige Nutzen. Genutzt werden diverse Atmosphärendaten, und simulierte Transmissionspektren von TAPAS. Der Vergleich zwischen den zeitlichen Verläufen der Atmosphärendaten mit den simulierten und den beobachteten Spektren bietet eine gute Schnittstelle für die Analyse. Die Spektrallinien der Erdatmosphäre konnten effektiv korrigiert werden, und der Vergleich bietet tatsächlich wechselseitige Nutzen für die Erdbeobachtung und Atmosphärenforschung; die Korrektur konnte auch von astrophysikalischer Perspektive die Spektrallinien der Erde von denen des Zielobjektes trennen und ließ genug Signalstärke für eine Analyse übrig. Die Ergebnisse wurden für verschiedene Testszenarien quantifiziert.

Contents

List of Figures

List of Abbreviations

AU   Astronomical Units

CCD   Charge-coupled device

CD   Cross-disperser

COSMIC   Constellation Observing System for Meteorology Ionosphere and Climate

DEC   Declination

DOY   Day of the Year

ECMWF   European Center for Mid-Range Weather Forecast

E.g.   Exempli gratia

ERA5   ECMWF's 5th Re-Analysis

ESA   European Space Agency

GNSS   Global Navigation Satellite System

GPS   Global Positioning System

HITRAN   high-resolution transmission molecular absorption database

I.e.   Id est

LBLRTM   Line-by-line Radiative Transfer Model

LBT   Large Binocular Telescope

LOS   line-of-sight

NOAA   National Oceanic and Atmospheric Administration

OLCI   Ocean Land and Color Instrument

PEPSI   Potsdam Echelle Polarimetric Spectrograph Instrument

PWV   Precipitable Water Vapor

RA   Right ascension

RT   Radiative Transfer

RV   Radial Velocity

SNAP   SeNtinel Application Platform

SNR   Signal to Noise Ratio

TAPAS   Transmissions Atmosphériques Personnalisées pour l'AStronomie

TCWV   Total Column Water Vapor

TOA   Top-of-the-Atmosphere

UCAR   University Corporation for Atmospheric Research

VLT   Very Large Telescopes

ZHD   Zenith Hydrostatic Delay

ZTD   Zenith Total Delay

ZWD   Zenith Wet Delay

Chapter 1

Introduction

Earth's atmosphere is almost or fully opaque at most wavelengths of the electromagnetic spectrum, impairing the observations through it. Radiation is only able to pass through in narrow wavelength sections, called 'atmospheric windows' (Ulmer-Moll et al., 2019), where the gases in the atmosphere cause considerably lower absorption. In the 'atmospheric window' in the visible wavelength range, the transmissivity of our atmosphere is very high (Turchi et al., 2018). The wavelength dependent absorption behavior of the various molecular and atomic constituents create a spectral pattern hereafter referred to as 'Earth's transmission spectrum'. In a spectroscopic observation, the transmission spectrum is compounded with the target's true spectrum, which cannot be observed 'as it is' (Bertaux et al., 2014; Ulmer-Moll et al., 2019). Disentangling the spectral features of different origins is called an 'Atmospheric Correction'. This thesis engages in the topic of atmospheric corrections, and examines in particular one novel Correction Method (Strassmeier et al., 2015, 2017; Ilyin et al., 2018).

The absorption spectrum of a gas can be reproduced under laboratory conditions, like a spectral fingerprint. If the volume mixing ratio in the line-of-sight is known and the position of the absorption can be modelled with the current state of research (Platt and Stutz, 2008; Husser and Ulbrich, 2013; Allart et al., 2022). For some well mixed gases, such as O_2 the volume mixing ratio is indeed a function of temperature and pressure, thus altitude (Bertaux et al., 2014; Kerber et al., 2014; Allart et al., 2022). A 'Model-based Correction Method' is based on a robust knowledge of the atmospheric state at the time of the observation and then generates a prediction of the spectral contamination. While the concentration of many atmospheric constituents can be measured precisely enough to model their absorption behavior, this is not the case for all. Outside of lab conditions multiple molecular species' absorptions overlap, and scatter and wind affect the transmission (Platt and Stutz, 2008; Figueira et al., 2010). And most importantly, some gases are *not* homogeneously distributed. The concentrations of water vapor, for example, can vary on short timescales (Kerber et al., 2014). This complicates the correction for spectral water vapor features in observations. A second type of correction approach - an 'Empirical Correction Method' does not require prior knowledge of the atmospheric state. Such a correction is rather based on systematic effects in the observed data, from which the contamination can be inferred. This is also the case for the Correction Method closely examined in this study, suggested by Strassmeier et al. (2017); Ilyin et al. (2018). It exploits the systematic differences in the temporal behavior of the spectral features that originate from multiple sources; the underlying trends in

a time series of observations are normalised with a Univariate Smoothing Spline Interpolation, described in Section 3.3.2.

This Correction Method was already successfully applied by Keles et al. (2022). However, the limits and potential constraints of this method have not been assessed to the current state of research. This will be done carefully for specific aspects of the method in this thesis. The Correction will be applied to ground-based astrophysical observations of a stellar system hosting an exoplanet. This is one of the application examples for this method, where an especially high accuracy of the correction is required. Hidden in the observational data will be an artificial exoplanet signal to be reproduced after the correction for Earth's transmission. This allows a precise quantification of potential losses or distortions of the signal. The efficiency to remove Earth's transmission spectral features from observations is also quantified in this study, in regard to possible future reciprocal benefits or applications in Earth Observation or Atmospheric Sciences.

Water vapor in the atmosphere is certainly not monitored only for the accurate correction of Earth/Space Observation imagery. Even more so, the concentrations and dynamics of atmospheric water vapor are important parameters for the production of weather forecasts, on short timescales; and on longer timescales for the production of climate models and climate predictions. Water vapor is classified as an extremely potent greenhouse gas (Allan et al., 2022; Neelin et al., 2022). The high spatial and temporal variability of atmospheric water vapor, however, aggravates the continuous surveillance (Diedrich et al., 2016; Kalakoski et al., 2022). The dense monitoring of atmospheric water vapor is of interdisciplinary interest. And the results of this study will be examined with respect to potential reciprocal benefits. The main Research Question of this Thesis is therefore *Can the Empirical Telluric Correction Method by Univariate Smoothing Spline Interpolation remove Telluric spectral features from observations effectively, and preserve the spectral features of interest therein?*. And *What are the reciprocal benefits of this Method to Earth Observation and Atmospheric Sciences?* The following Objectives describe how the Research Questions were answered.

1. Establish the atmospheric properties for the time and location of the observation.

2. Perform a full Telluric Correction by Univariate Smoothing Spline Interpolation, and establish how much of the Telluric Contamination was corrected for.

3. Establish how many exoplanetary features were preserved.

The following Chapter 2 provides the core concepts, wider field of literature and background to this research, Chapter 3 describes the various data sets, processing and analysis methods used. The results are presented in Chapter 4 and discussed and concluded in Chapter 5.

Chapter 2

Background

2.1 Motivation

Julius Comroe coined a term 'Blue Sky Research' in 1976, describing research that is exploratory and curiosity-driven, contrasting narrow goal-driven research with practical use. He advocated for a science climate open for questions as trivial - and as fundamental - as 'Why is the sky blue?' (Linden, 2008). The research for this Thesis was certainly Blue Sky Research for me.

The following Chapter provides the concepts of Exoplanets, Spectroscopy and Atmospheric Corrections built upon in later Chapters, compares Astrophysical and Earth Observation, and discusses their common academic interests in Earth's atmosphere, expanding on the initial problem statement.

2.2 Introduction to Exoplanets

In 1995, the two now-Nobel prize-holders Michel Mayor and Didier Queloz published a paper on the first confirmed detection of a planet (51 Pegasi b, or Dimidium) outside our solar system orbiting the sun-like star 51 Pegasi (Mayor and Queloz, 1995). Even though there had been two other detections prior to theirs, 51 Pegasi b was the first to be confirmed. And soon, many more followed (Perryman, 2014). Since 1995, almost 5500 more of such extra-solar planets have been discovered, short: exoplanets Exoplanet Archive. With the current state of knowledge it is reasonable enough to say that planets exist around most stars, an that there is more planets than stars in our Galaxy (Van Hoolst et al., 2019).

Typically, exoplanets cannot be observed directly, because they are very faint objects, that don't emit radiation. They only reflect the radiation of their host star, with a much smaller surface than the star itself. That star is located already at an immense distance from Earth. The closest stellar neighbour, for example, is Proxima Centauri, located at a distance of 4.2 light years (approx. 1.3 parsec), this equals roughly 39.74 billion km, or 265,606.74 'Astronomical Units' (AU), 265,606.74 times the distance from Earth to the sun (ca 150 mio km) (Carroll and Ostlie, 2014). Imagine trying to directly observe a dark object located at even one AU next to its bright stellar companion. The majority of confirmed exoplanets is located much closer to their host stars than one AU. Direct imaging as a method of detection or observation is thus

Edge-on   Face-on
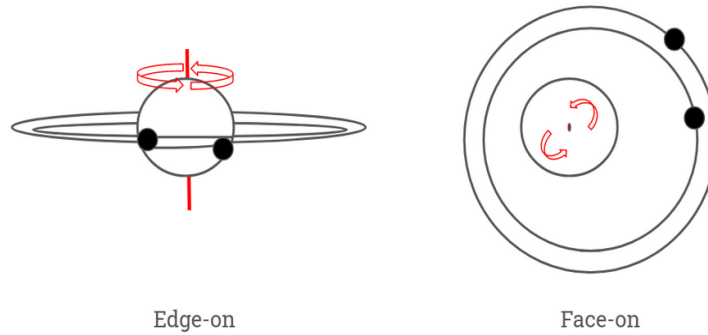
Figure 2.1: Apparent inclinations of planetary systems, own illustration.

feasible only for planets further out and with own considerable radiation - for example as thermal emission during their formation phase. Most exoplanets are detected and studied through indirect observation of the light of the star, and how this is affected by exoplanets in its orbit (Birkby, 2018).

2.2.1 Transit Method

The so far most successful detection method (quantitatively) is the Transit method (Charbonneau et al., 2000; Henry et al., 2000). For some exoplanets that are very favourably aligned in their orbit around their host star, our point of view on the system is 'edge-one' and we can observe how the planets transit in front of their host star (Birkby, 2018). This is depicted in the Figure 2.1 below, where we see the apparent inclination: the favourable observing geometry is not a result of the alignment of the planet's orbital plane with their host star's spin, which is very common. The favourable geometry is a result of the observers' coincidental point of view on that system. This is either 'edge-on', or 'face-on', or - most likely - something in between. In fact, the statistical probability of a system observed edge-on with the orbiting planets creating a transit is estimated at < 2% (Borucki and Summers, 1984; Barnes, 2007; Birkby, 2018). And yet, this method has yielded the highest detection rates (Madhusudhan, 2019).

Figure 2.1: Apparent inclinations of planetary systems. Shows the inclination of the star's own rotation (red) and the inclination of the ecliptic plane of the orbiting planets. Own illustration.

In an ideal observing geometry, directly 'edge-on', the planet transits perfectly in front of the center of its star, and can also be observed just before and just after it disappeared behind the star in the so-called secondary eclipse. During transit it visually blocks a fraction of the bright stellar surface, dimming the light of the star. This darkening effect is not large, but occurring periodically, again and again (Perryman, 2014; Madhusudhan, 2019). Using the geometry and architecture of the solar system as a reference, a planet such as Jupiter would cause a dimming of the sun's light by about 1% to an extrasolar observer; Earth would cause a dimming of $< 0.01\,\%$ (Borucki and Summers, 1984; Van Hoolst et al., 2019). Just before and just after the secondary
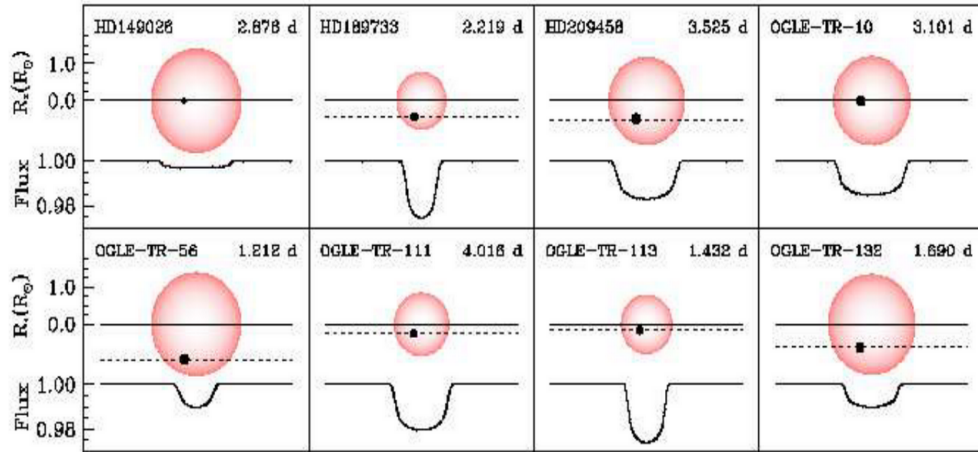
Figure 2.2: Transiting exoplanets, with stars and planets to scale, with the planets' impact parameters (dotted lines), transit light curves and the orbital periods (Torres et al., 2008).

eclipse, the planet appears like a full moon: fully illuminated by the stellar light. Adding its reflected light to that of the star, the entire star-planet-system appears slightly brighter just before and just after the secondary eclipse; during the eclipse we see only the light of the star (Perryman, 2014; Madhusudhan, 2019). Planets that don't transit exactly along the equator of their star, might not create a secondary eclipse; or vice versa, although this is much more challenging to confirm (Perryman, 2014; Madhusudhan, 2019).

This method is favourable to planets at $< 1\,\text{AU}$. These planets complete their orbit in much < 365 days, rather in a few days or even a few hours. A few hours of observation can therefore cover the entire orbital period of the planet. Planets on an Earth-like orbit require longer monitoring periods - something that can be extremely challenging for a ground-based telescope on a rotating planet Earth (Birkby et al., 2013b). The Transit method is equally favourable to planets with large radii, that can block off a greater fraction of their host star's surface, such as Jupiter-sized or Saturn-sized Gas Giants. This leads to a detection bias that does not necessarily reflect the true occurrence rates of the different planet types (Gaudi et al., 2021) shown in Figure 2.3.

How much the overall luminosity of the star is reduced during the transit of a planet depends on several orbital parameters and can vary significantly. This is shown in Figure **??**, comparing the known parameters of 8 exoplanets. In the case of the exemplary exoplanet HD 189733b (Top row, second to the left), the transit causes an overall reduction of $< 2\,\%$ of the flux of its host star. This transit light curve depth depends on (i) the radius of the exoplanet relative to the radius of its host star; and on (ii) the 'impact parameter', indicating where the planet transits in front of its star - perfectly past the center, or merely grazing the edges. The 'impact parameter' is illustrated as the dashed line. HD 189733b indeed doesn't transit directly in front of the central parts of its star, but rather towards the edges (Torres et al., 2008).

2.2.2 Radial Velocity Method

Alternatively, exoplanets are detected with the Radial Velocity method (Mayor and Queloz, 1995). Observed are small variations in the radial velocity of the star itself, as it orbits around the common center of mass of the entire system. Since most of the mass of the stellar system is concentrated in the star, its orbit is considerably smaller than the orbit of the low-mass planets, performing a somewhat reflex motion, like a lever (Perryman, 2014). This motion can be described through Kepler's laws and explained with the principles of Newtons gravitation laws, where gravity is never one-sided, but bilateral: it exerts a pull in mutual directions between two bodies. The magnitude of the gravitational pull that a body experiences is proportional to the product of *both* masses, decreasing inversely proportional to the square of the distance between them (Carroll and Ostlie, 2014; Perryman, 2014):

$$F_{\mathrm{A,B}} = \frac{G\,\mathrm{m_1 m_2}}{\mathrm{r}^2}, \tag{2.1}$$

$$F'_{\mathrm{A}} = -F_{\mathrm{B}}, \tag{2.2}$$

where G is the Gravitational Constant ($6.673\,10^{-11}\,\frac{m^3}{kg\,s^2}$) and $F_{\mathrm{A,B}}$ can be used to describe the gravitational pull of body A on body B.

The star's reflex motion can be detected through the 'Doppler Effect'. The light of the star moving towards the observer is squeezed and perceived at a shorter - bluer - wavelength; the light of a star moving away from an observer is stretched and perceived at a longer - redder - wavelength. Albeit, these variations are so small, that the blue and red shifts of the light of the star can only be detected spectroscopically, with the shift of absorption lines in the spectrum of the star slightly towards to redder or bluer parts of the spectrum (Perryman, 2014; Carroll and Ostlie, 2014). Detectable through 'Doppler Spectroscopy' is only the component of the stellar motion towards or away from the observer, the lateral/perpendicular components are virtually invisible. This excludes the detection of planetary systems which we observe entirely 'face-on' (2.1), but the geometry of detectable systems is larger than with the Radial Velocity method (Van Hoolst et al., 2019). The detection possibilities for 'face-on' observation geometries are only slowly advancing with Astrometry observations, such as with the Gaia space mission (Brown, 2021). The Radial velocity method for detection is most sensitive to massive exoplanets that exert a stronger gravitational effect on their host stars (Gaudi et al., 2021; Zhu and Dong, 2021). This introduces a detection bias favouring more massive planets with larger radii on closer orbits around their host stars. This can be seen in the Figure 2.3 below. Compared to the Solar System Planets, most indeed have shorter orbital periods and Jupiter-Earth-radii. The detections indicated as 'Kepler' are detections by Transit Method by the Kepler Space Telescope; the planets indicated as 'Other Transit' and 'Radial Velocity' were detected by other space-based or ground-based telescopes by Transit Method or Radial Velocity Method, respectively; the quantitatively less successful 'Other' detection methods include gravitational microlensing (Mao and Paczynski, 1991), transit timing variations (Miralda-Escude, 2002), and direct imaging (Close
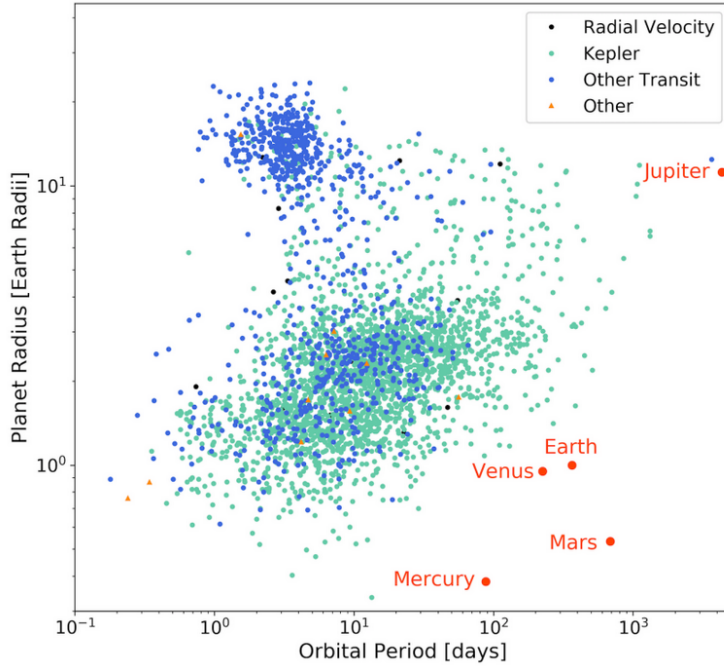
Figure 2.3: Demographics of known exoplanets by radius over orbital period. The colour indicates the detection method. (Red) the Solar System Planets by radius over orbital period for orientation. Figure excludes (i) a group of 25 additional directly-imaged exoplanets and (ii) exoplanets detected after 2021 (Gaudi et al., 2021).

et al., 2014).

Moving systems

This thesis does make use of transit data; however, the principles of radial velocities play a fundamental role in the suggested correction approach. Specifically, the fact that the multiple systems involved experience different radial velocities.

As explained above, the **star** induces a heavy gravitational pull on the planet, causing it to orbit the system's center of mass in a wide orbit. But the planet equally induces a gravitational pull on the star, causing a small reflex motion. During one half of the orbital Phase, a transiting planet's relative motion is toward us (positive RV), the second half away from us (negative RV). This produces a periodic amplitude. What magnitudes do we know from the Solar System?
Earth's gravitational pull causes a reflex motion of the Sun $K_\odot$ of 9 cm/s along our (ideal) line-of-sight (LOS). This might sound small, but is in fact already in the lower detection limit of ground-based instruments such as the ESPRESSO instrument installed at the Very Large Telescopes in Chile (Sedaghati et al., 2021). A much more massive planet, such as **Jupiter** induces a radial velocity amplitude $K_\odot$ along our LOS at the order of $12.4\,\mathrm{m\,s^{-1}}$ (Birkby, 2018; Van Hoolst et al., 2019). The planet Jupiter is orbiting our Sun at a distance of ca 780 million kilometers (roughly 5 Astronomical Units/AU). The architecture of other planetary systems is in many cases unlike ours, with Giant Jupiter-like planets orbiting their host stars much closer,
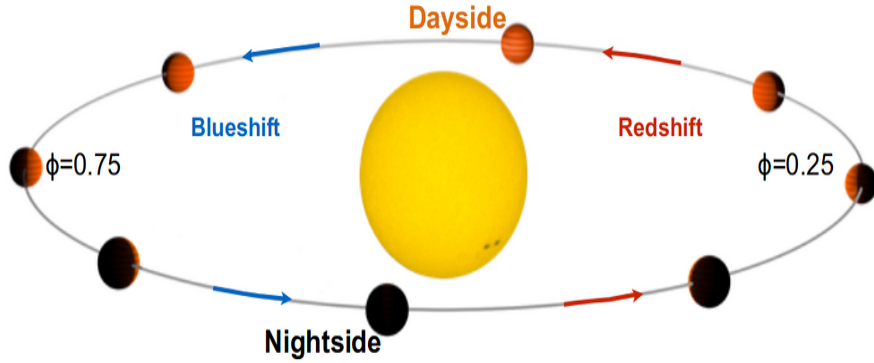
Figure 2.4: The orbital phase of a planet and the Doppler shifts it experiences. Image credit: Ernst de Mooij, from Birkby (2018).

with entire orbital periods of $P < 10$ days. These are called 'Hot Jupiters' (Wang et al., 2015). Such a massive planet, on such a close orbit can induce a radial velocity amplitude $K_\star$ of a sun-like star along our LOS at a $100\,\mathrm{ms}^{-1}$ level (Birkby, 2018).

Still, the radial velocity amplitude of a planet is several orders of magnitude larger. **A planet's**, e.g. Earth's amplitude $K_\oplus$ is ca $30\,\mathrm{kms}^{-1}$ (Birkby, 2018); **Jupiter's** amplitude K_{Jup} caused by the sun is ca $13.1\,\mathrm{kms}^{-1}$ (NASA NSSDCA; and a close-in orbiting **Hot Jupiter** up to hundreds of kms^{-1} (Birkby, 2018).

The term 'Radial Velocity' is observed as a spectral effect. It always refers to the relative movement of an object towards or away from an observer. And indeed, only the component of the motion in LOS. Any relative motion perpendicular or lateral to the observer - where the true inclination cannot be differentiated anyway - is non-detectable as Radial Velocity. The observed velocity K will be a function of the true velocity v and the apparent inclination of the object's movement towards the observer: $K = v \sin i$. The greater the radial velocity component in LOS of an object relative to the observer's own velocity, the larger its spectral 'Doppler Effect' (Mayor and Queloz, 1995). The Doppler Effect describes the apparent and observed change in wavelength (or frequency) of the light of a body, when it is moving toward or away from an observer. The observed wavelength of an object moving away from an observer will appear longer (redder), as shown in Figure 2.4 below. This does not mean that the entire spectral fingerprint is shifted towards the blue or red end of the spectrum, because the Doppler Effect is wavelength dependent and can be described as follows:

$$\Delta\lambda = \frac{v}{c}, \tag{2.3}$$

where λ is the true wavelength of the light, $\Delta\lambda$ the difference between the observed and the true wavelength, v the velocity component in LOS of the observer (the radial velocity) and c the speed of light (Carroll and Ostlie, 2014).

On top of the measurable relative orbital velocities of the observed bodies comes a rotational velocity component from the diurnal rotation. This is true for the Sun and for Jupiter like
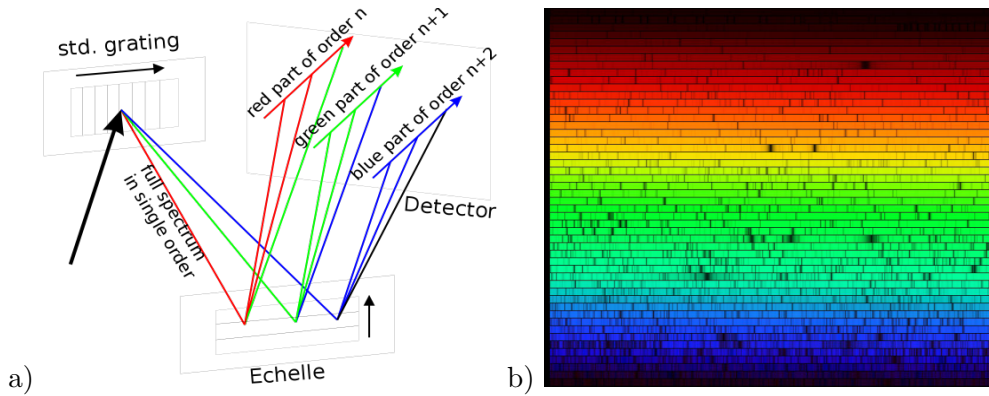
Figure 2.5: a) Echelle diffraction grating principle. Image credits: Boris Považay (Cardiff University, UK); b) Example Echelle spectrum, which shows almost the cross-dispersed optical Solar spectrum, produced by the HIRES Echelle spectrograph (on the 10 m Keck telescope, Hawaii). Image credits: Vik Dhillon (University of Sheffield, UK).

planets as well, whose rotational velocities will be discussed later. What matters most, however, is Earth's diurnal rotation, which causes an equatorial speed of 465.10 metres per second (1,674.4 km/h) (Carroll and Ostlie, 2014). Additionally, the entire Solar System is moving through the galaxy. As are the other stars, but not at equal velocities. Again, what matters are the components of the velocities along our LOS (Strassmeier et al., 2017; Keles et al., 2022).

2.3 Spectroscopy

In spectroscopy, absorption and emission of light are measured by wavelength, instead of merely by colour. Opposed to photometry, there is no need for filter after filter; instead the electromagnetic radiation is split and dispersed, and the light of specific wavelengths measured individually. This can be done for example with a glass prism, where the incident light is refracted according to its wavelength and scattered at a specific angle. The scattered light can be observed or collected segment by segment on photographic plates, or rather in digital format on CCDs (charge-coupled devices) - photosensitive electronic modules (Carroll and Ostlie, 2014). The optimisation of the process of refractive dispersion in high-resolution spectroscopy involves broadening the scatter of light and recording smaller segments, representing smaller wavelength ranges. But to avoid recording the broad stretches of dispersed light on longer and longer chains of CCDs, a so-called 'Echelle' diffraction grating can be applied. Here, two layers of dispersers are arranged in sequence, illustrated in Figure 2.5 a. The incident light is diffracted on a first order grating (discrete dispersion) and reflected onto the second order grating, which is oriented perpendicular to the first and which further refracts the already dispersed light. The second order grating is thus called a cross-disperser. The otherwise broad stretch of dispersed light can now be collected in multiple rows on a single squared CCD (Figure 2.5 b). The 'ladder' and 'rung' like appearance gave this type of diffraction grating its name. 'Echelle' gratings are typically used in high-resolution spectroscopy (Figueira et al., 2010; Eversberg and Vollmann, 2014; Zhang et al., 2022).

A 'Spectrograph' is the instrument that includes the diffraction grater and the CCDs. It's

typically located behind the lens or mirror, where the incoming light is detected, or in some cases, the light is fed via fibers to the instrument (Strassmeier et al., 2015). Spectrographs find many applications, by no means limited to Earth or space observation. They are commonly applied in quantum research, magnetic resonance imaging (MRI), or analytical chemistry. For the spectroscopic observer, light simply carries information; for example information about temperature of the radiating body, and the material with which the light interacted between emission and detection. Depending where we we try to observe from (ground-based or space-based), or in which direction we wish to observe (Earth-bound or space-bound), we will see traces of all these interactions in the observed spectra. Whatever spectral effect is known to us beforehand, can be accounted for in the actual observation, and disentangled from what we really wish to see: the spectrum of the observed target.

2.3.1 Earth Observation with space-based satellites

If we imagine a scene, as observed by an Earth Observation satellite, what will be part of the measured spectrum?

Active vs. Passive sensors

Earth Observation satellites can generally have two sensor types installed on board: active or passive (Skolnik, 1990). In the case of an **active sensor**, the satellite carries a Lidar instrument (Light detection and ranging), or more specifically a Radar instrument (Radio detection and ranging). This instrument emits primary signals of electromagnetic pulses (e.g. in radio frequencies) that are reflected on the ground or any other object's surface structures. The reflected secondary signal, or echo is received again at the satellite. Since the properties of the emitted radiation - flux and wavelength - are known, any change of the incoming irradiation provides information: the distance to the object (from the time lag of emission and measurement), the relative motions of sender and object (from a Doppler-shift between emitted and received signal), or the scattering/reflective properties of the object (from flux variation or polarisation). Radar/Lidar systems are commonly used as altimeters to produce Digital Elevation Models/Digital Surface Models (Skolnik, 1990; Weitkamp, 2005; Richards et al., 2010).

The functionality of a **passive sensor** is different. The properties of the light received at the sensor are not purely a function of change from known properties of the light, because the light source is not a controlled variable. The passive sensors on board of Earth Observation satellites collect the Earth's reflectance during the day, illuminated from the Sun as light source. The measurement at the sensor is a function of the solar radiation, the object's reflective properties and the interactions along **two** paths (Windle et al., 2022). The first path and the total incoming solar radiance at the surface L_{rad} can be described as:

$$L_{\mathrm{rad}} = L_{\mathrm{toa}}\, T_\lambda + L_{\mathrm{p}_\lambda}, \tag{2.4}$$

where L_{toa} is the solar radiation at the Top of the Atmosphere (TOA), where T_λ is the atmospheric transmission (mostly absorption effects), and L_{p_λ} the atmospheric path radiance (mostly scattering effects); both are wavelength dependent (adapted from Windle et al. (2022)). The second path and the radiance measured at the sensor L_{s} can be described as:

$$L_{\mathrm{s}} = L_{\mathrm{rad}}\,\rho\,T + L_{\mathrm{p}_\lambda}, \tag{2.5}$$

where ρ is the reflectance of the target. ρ itself is a function of the reflectance regulated by surface interactions of the incident irradiance $L\mathrm{w}$ and by type of optically active surface constituents (thermal irradiance) E_{d}, based on Windle et al. (2022):

$$\rho = \frac{L_{\mathrm{w}}}{E_{\mathrm{d}}} \tag{2.6}$$

The following section illustrates the interactions along both paths, as well the source of the light.

Solar Radiation

Initially, and for the sake of simplicity, let's regard the sun as a star as an ideal black-body. As such, all incident radiation is absorbed and not reflected. The shape of the light curve and the peak wavelength are determined by its temperature alone. The effective temperature of the sun of approximately 5780 K (Lang, 2006) produces a black-body radiation with a peak at (ca) 600 nm in the visible range of the electromagnetic spectrum, emitting mostly photons of this energy. The black-body radiation of a cooler star (e.g. 3000 K) peaks at 900 nm, much further in the infrared spectral range. This radiation is emitted specifically from the photosphere - the most deep-seated part of the solar atmosphere with an average thickness of 100 km, often described as the visible surface of the sun. Since photons are emitted from the photosphere at roughly the same rate as new photons from the core make their way to the stellar surface, the photosphere of the sun can be regarded as 'in thermal equilibrium' (Carroll and Ostlie, 2014).

Absorption

The solar radiation is idealised as a Blackbody radiation, but in reality shows a multitude of absorption lines, reducing the solar light at very specific colors. These occur from interactions of the photons with elements present in the sun. As the photons make a random walk through the layers of the sun, they excite the elements they encounter. The electrons in the atoms jump up to a higher energy level when excited - which takes a very specific amount of energy for the electrons of different elements. The photons are absorbed during this process, but only those with the specific energy (corresponding to a specific wavelength). The elements are hereby leaving their fingerprint in the solar spectrum.
Back to the question: why are the solar photons emitted from the photosphere and not from the core? The temperature and pressure conditions in the sun make the interior practically

completely opaque to photons, because they permanently encounter elements on their random walk, being absorbed and re-emitted. Until it makes its way to the photosphere, where the mean free path is so much longer, that the photons actually get a chance to escape. The elements in the solar photosphere that absorb photons at visual wavelength are mostly iron and sodium (Platt and Stutz, 2008; Carroll and Ostlie, 2014).

Emission

Elements can also emit photons when their electrons fall to a lower energy level and release this specific energy. This occurs above the photosphere, in the outer solar atmosphere: the chromosphere (up to 3,000 km above the sun's 'surface') and the corona (up to 20,000 km). These regions are transparent to visual light, but temperatures are so high, that the gas emits photons. These emission lines are also present in the solar spectrum; in the visual range, they are caused by the Helium gas in the sun's chromosphere (Platt and Stutz, 2008).

Solar irradiance at Top-of-Atmosphere (TOA)

The energy flux density dissipation f is a function of luminosity of a source L (radiant power over time and area, measured in Watt m^2) over a spherical angle Ω (idealised) and over a distance r^2, without considering absorption effects from interaction:

$$f = \frac{L}{\Omega\, r^2} \tag{2.7}$$

Over the course of its annual slightly elliptical orbit, Earth is not equally distanced to the sun. This varies between perihelion - the closest distance to the sun (147,098,070 km) - and aphelion - its furthest distance to the sun (152,097,700 km). This difference in distance theoretically reduces the solar radiation at TOA at aphelion by roughly 6.45% compared to perihelion (Berger, 1978).

The luminosity of the sun however also undergoes several periodic changes itself. Multiple long-term activity cycles are known, the most imminent being the approximately 11 year solar magnetic activity cycle. During this time, the number of darker *sunspots*, as well as bright *faculae* regions on the solar surface, as well as other solar surface activities fluctuate between the solar minimum and the solar maximum of the activity cycle. This fluctuation is caused by the magnetic field, which is building up and increasing its strength at/after solar minimum, then getting increasingly entangled and instable, until it ultimately flips at solar maximum. With the increasing instability of the magnetic field dark features such as sunspots, or bright features such as faculae can appear on the solar surface. From solar minimum to solar maximum, the sun's overall radiation increases by about 0.1%. The solar irradiance, however, as perceived at Earth's Top-of-the-atmosphere (TOA), varies additionally to that overall increase on a much shorter time period of approximately 27 days, whenever bright or, respectively, dark features on the solar surface rotate into and out of view, with the sun's own - latitude dependent -

differential rotation. This differential rotation can vary from 24.5 at the solar equator to 38 days at the solar poles (Zhivanovich et al., 2021; Snodgrass and Ulrich, 1990). The apparent variation of brightness from the overall radiation amplitude between solar minimum and maximum, that is rotation-dependent, can increase and decrease the sun's luminosity by additional -0.3% and + 0.05%. The space-based monitoring of the sun to determine the solar irradiance at the TOA has improved over the past decades (Willson and Hudson, 1991; Reinhold et al., 2020).

Interactions in Earth's atmosphere

Having reached Earth's atmosphere, the photon's mean free path is shortened again, with increasing densities of elements and thus an increasing possibility for interaction. This can be described with the 'Beer-Bouguer–Lambert law' that determines the optical thickness: the attenuation of light in relation to the (material and density) of the material it passes through (Platt and Stutz, 2008; Mayerhöfer et al., 2020). The interactions of the photons in Earth's atmosphere resemble the interactions in the solar atmosphere: the different element species in the atmosphere absorb only the photons with the specific energy required for the electron in their core to jump to a higher energy level.

Above the thermosphere, in the exosphere (the region hosting most satellites), the atomic and molecular density is so low, that the mean free path of photons, before they collide with another element is approximately 10 km (Schorghofer, 2020). In the upper layers of the thermosphere (85 - 600 km), higher energy photons in the ultraviolet, X-ray and gamma wavelengths get fully absorbed and the atmosphere is entirely opaque. Towards the stratosphere (ca 12 - 50 km), the atmospheric density increases strongly. Especially the concentration of O_3 is high, but absorption occurs also because of O_2. The ozone absorption in the stratosphere protects surface life from the harmful shortwave UV radiation. The spatial and temporal concentration of ozone is governed by both photochemical and advection/dynamical processes. Albeit, we can consider it stable on short time scales, with most ozone (90%) concentrated in the stratosphere (Neale et al., 2021; Langematz, 2019). The troposphere (0 - ca 12 km), the lowest atmospheric layer, holds 80% of the total mass of the atmosphere and is dominated by CO_2, O_2 and water vapor. The concentration of water vapor is almost exclusively limited to the troposphere. Its distribution is strongly dependent on temperature and pressure, and the saturation-specific humidity of the air (Randall et al., 2007). Not only absorption matters, but also several scattering processes play a role, mostly Rayleigh scattering (Young, 1981) - stronger in the blue wavelength regime - and Mie scattering (aerosol particle scattering) (Platt and Stutz, 2008; Nguyen et al., 2015) For solar light, Raman scattering also plays a role (Young, 1981).

The incident solar irradiance at the surface L_{rad} now interacts with the surface material. The absorption or reflectance behavior is measured as surface reflectance ρ, which also accounts for any thermal irradiance of the surface E_d (Windle et al., 2022). On dark pixels, both absorption *and* scattering effects are stronger (Nguyen et al., 2015; Preusker et al., 2021). The outgoing radiation is once again attenuated by atmospheric transmission T_λ through absorption of its constituents, and the atmospheric path radiance (mostly scattering effects) L_{p_λ}. Ultimately, the

reflected light of the observed surface reaches the sensor (as radiance at the sensor L_s) on board of the Earth Observation satellite, with many satellites in an altitude of around 800 km in the Exosphere. To avoid the contamination of the measured L_s by e.g. thermal emission from the instrument itself, thermal insulation and temperature-conditioning is important (Sentinel 3 OLCI).

2.3.2   Space Observation with ground-based telescopes

If we imagine a different scene, as observed from a ground-based instrument, how does that differ? One such ground-based instrument could be a Radiometer. Such an instrument observes the thermal radiation of the sky in radio-frequencies, which gets attenuated with the presence of water vapor. This makes Radiometers very useful for direct measurements of atmospheric water vapor. In specific measurement-configurations, Radiometers can even produce a vertically resolved profile of water vapor in the atmosphere (Rosenkranz, 1998; Matzler and Morland, 2009; Payne et al., 2011).

Observing other stars

Ground-based astrophysical telescopes seek to observe *through* the atmosphere, for example the light of other stars. In this case, the source of the light is less known, compared to the light of the Sun. But the main character of the light curve - its peak - is dependent on the near-black-body radiation from the temperature in its photosphere. This can be determined well enough with physical principles (Carroll and Ostlie, 2014). Although the inner structure of stars varies greatly, the stellar light experiences absorption and emission effects from, e.g. the photosphere or chromosphere, corona. As the stellar photons travel to an observer on Earth, the light is dissipated over a large area, and again attenuated with the 'energy flux density dissipation' function (2.7). What remains is the apparent luminosity of the star, which is dim by comparison to the sun.

Interactions in the line-of-sight (LOS)

The interactions in the LOS might include interactions with interstellar gas (Ward-Thompson and Whitworth, 2011), although these are not relevant to this study. Relevant are the interactions in the immediate stellar neighborhood, with its orbiting planets. A transiting planet - observed with a favourable geometry 'edge-on' - periodically dims the light of its star. If the planet has an atmospheric envelope, only the solid part of the planet blocks the stellar light uniformly. Light of different wavelengths can penetrate different depths until absorbed. Following the same principles of the 'Beer-Bouguer-Lambert Law' applicable for Earth's Atmosphere, the amount of absorption in the exoplanet's atmosphere depends on the properties and density of the attenuating species (Platt and Stutz, 2008; Mayerhöfer et al., 2020). Since our observations cannot spatially resolve the star and the exoplanet next to or in front of each other, we see the light of the star alone; and how the stellar light changes. The faint molecular fingerprint of the planet's atmosphere is encoded in the stellar light and can be retrieved, for example with its periodicity of change, as

well as cross-correlation with forward-models of expected molecular species (Madhusudhan and Seager, 2009; Snellen et al., 2010; Heng, 2016; Brogi and Line, 2019).

When the light of the star reaches Earth's atmosphere, it is exposed to the same physical processes as the light of the sun. The absorption features associated with the molecular composition of our atmosphere are now called 'telluric lines' (Perryman, 2014; Madhusudhan, 2019; Allart et al., 2022). For nighttime observations, scattering effects play a minor role (Ulmer-Moll et al., 2019). Relevant can be spectral effects from the moon, when it is visible above the horizon (Jones et al. 2014). At the ground, the light is collected with a mirror and fed to the instrument, for example into a spectrograph.

(High) Resolutions

The resolution capacities of ground-based astrophysical spectrographs are currently much higher than those of spectrographs on Earth Observation Satellites - and higher than those on astrophysical Space Telescopes. The main reasons for this are the dimensions of such instruments, weight and size being limited. The resolution capacity, in this case, refers both to spatial as well as spectral resolution. The spectral resolution is commonly indicated as:

$$R = \frac{\lambda}{\Delta\lambda}, \text{ or } R = \frac{c}{\Delta v}, \tag{2.8}$$

where λ gives the total covered wavelength range, and $\Delta\lambda$ the difference between two resolvable wavelengths, or Δv the difference between two resolvable velocities v, with c as the speed of light.

A higher resolution allows for the wavelength separation of spectral features, that are otherwise smeared together. In lower spectral resolution, the absorption depth of a spectral feature often gets underestimated. This occurs, because adjacent wavelength with and without absorption are blended together (Birkby, 2018). This was simulated in the Figure 2.6, which shows the sensitivity to the true absorption depth of a spectral feature, at different spectral resolution capacities of instruments. The Figure was produced with simulated TAPAS transmission spectra, see Section 3.2.1 (Bertaux et al., 2014) The spectral resolution of the ground-based astrophysical spectrograph illustrated below is R=130,000 (PEPSI analogue, see Section 3.2.2). This allows a more precise wavelength distinction of 0.0006 Ångström (or 0.00006 nm) than with a spectrograph of a spectral resolution of R=20,000. The resolving power of the example space-based spectrograph (illustrated here at R=1,000) is with a true R=520 even lower than illustrated. The minimum discriminable difference between two wavelengths is 1.25 nm (OLCI analogue, see Section 3.2.1).

Especially for weight-/size-limited space-based missions, the higher spectral or spatial resolving power often needs to be weighted against the scientific interests. Therefore, the spectral resolution capacity of ground-based instruments is currently unmatched and will likely remain so
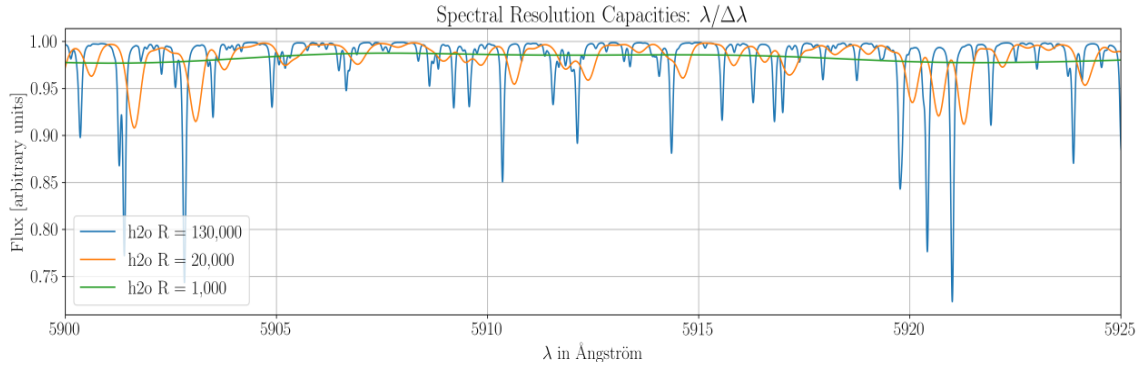
Figure 2.6: Shows several (telluric) H_2O absorption lines in example wavelength range, as they would be detected at different spectral resolutions. Own illustration, based on TAPAS simulations (3.2.1.

for the near future.

2.3.3 Transmission spectroscopy for Exoplanets

With growing exoplanet catalogues, mere detection is not the prime focus of exoplanet research anymore, although statistically significant research is certainly improved with larger sample sizes. The current main scientific interest, however, lies in the more careful and more precise study of the exoplanets that are already known (Charbonneau et al., 2002; Gaudi et al., 2021).

Some parameters of an exoplanet can be analysed practically without the need for its spectral fingerprint: the extent of the dimming of the light of the star, the 'transit depth' results from the radius of the planet relative to the radius of the star. If the stellar radius is known, the planet's can be robustly inferred, too (Pepe et al., 2002; Van Hoolst et al., 2019). The radial velocity amplitude of the star arises from the mass of the planet, and for a transiting planet, that reflex movement of the star is entirely along our LOS. When this it not the case, the mass of the planet can only be constrained with a lower limit (Pepe et al., 2002; Van Hoolst et al., 2019; Madhusudhan, 2019). Mass and radius of a planet can be used to determine or constrain the density and interior structure of the planet (Van Hoolst et al., 2019).

With 'Transmission spectroscopy' Seager and Sasselov (2000) an observer can look closer at the observations, where the planet's (atmospheric) absorption spectrum is hidden in the spectrum of the star. It is the difference between the spectrum of the star with a transiting planet 'in-transit', and the star alone ('out-of-transit'). The isolated exoplanet's transmission spectrum for an exoplanet with no atmosphere, the transmission spectrum would be empty; with an atmosphere present, the transmission spectrum is determined by the thickness and composition of the planetary atmosphere (Charbonneau et al., 2002; Torres et al., 2008; Snellen et al., 2010; Madhusudhan, 2019). The remaining absorption features in the transmission spectrum can be compared to forward models of the absorption behavior of molecules in a laboratory environment, such as HITRAN (Rothman et al., 2009, 2013; Gordon et al., 2022). We can build a statistic

understanding of the physical or chemical processes that shape planet's atmospheres (Birkby et al., 2013a; Crossfield and Kreidberg, 2017; Birkby, 2018; Van Hoolst et al., 2019), in terms of their evolution (Gebauer et al., 2017; Keles et al., 2022), or perhaps even the presence of life (Birkby et al., 2013b; Krissansen-Totton et al., 2018).

Rossiter McLaughlin effect

During the transit, when the planet obscures a fraction of the stellar surface, the star will appear slightly darker, decreasing the light flux virtually uniformly across all wavelengths. However, there is another effect happening in the observations of a star with an exoplanet 'in-transit'; the 'Rossiter McLaughlin effect' (Rossiter, 1924; McLaughlin, 1924).

The star in itself rotates - our Sun's differential rotation (fast at the solar equator, slower at the solar poles) was described above already (Zhivanovich et al., 2021; Snodgrass and Ulrich, 1990). One half of the star rotates toward us, the other half away from us. The approaching half of the light of the star is Doppler shifted towards the blue, the receding half Doppler shifted towards the red. One shift compensates for the other, from the observer's point of view, as we do not see the star spatially resolved anyway, but reduced to a single point source of light, thus none of these Doppler shifts are visible to the observer.

When the star's surface is obscured by a transiting planet, the star's approaching and receding hemispheres suddenly appear asymmetrical. Is the planet covering a fraction of the approaching - blue shifted - side, the overall light of the star will appear red shifted to an observer, and vice versa (Rossiter, 1924; McLaughlin, 1924).

This effect is strongest, when both the star's own rotation and the planet's orbit are aligned - a so called 'stellar spin-orbit alignment'. It is a valid assumption that they are, resulting from the formation process of star and planets and was shown in Figure 2.1. But this is not necessarily the case for all planets that we observe (Winn, 2006; Torres et al., 2008).

The 'Rossiter McLaughlin effect' (RM effect) can be a measure of potential misalignment between the axes of stellar spin $v \sin i_\star$ and planetary orbit, as misalignment angle (or 'spin-orbit angle') λ Rossiter (1924) and McLaughlin (1924). A planet with a small misalignment angle λ is perfectly aligned and obscures the blue and red shifted sides of its host star for an equal amount of time and transits past the star's equator, as can be seen in Figure 2.7. The distortion that it causes is large. The transit trajectory of planet with a large λ basically leads from the star's pole to pole. The blue and red shifted components of the stellar light are equally visible during all observations and the RM effect small (Cameron et al., 2010). The amplitude and the asymmetry of the apparent Doppler-distortion during a planetary transit can therefore be used to determine the inclination angle of the planet. This is commonly used in the analysis of transmission spectra (Morello et al., 2017; Triaud, 2018; Oshagh et al., 2018; Borsa et al., 2021).
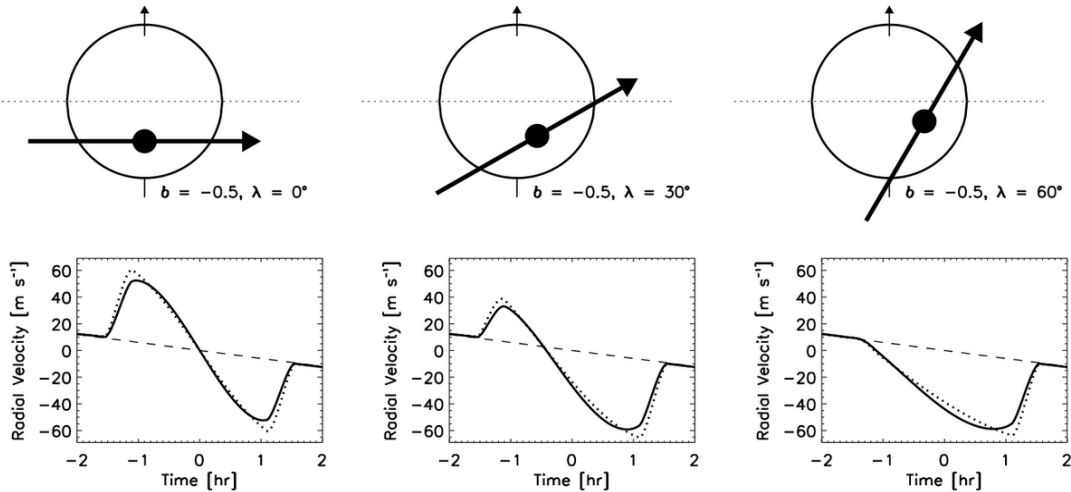
Figure 2.7: Compares the observable RM effect for different misalignment angles (Winn, 2006).

2.4 HD 189733 - one example system

The star observed for this study (HD 189733) is not visible to the naked eye. With a magnitude of 7.67 ±0.03 Exoplanet Archive, it is detectable only by telescope in a distance of approximately 64.5 light years (19.76 parsec), and is actually a pair of two stars. The companion star HD 189733B in the binary system is much smaller. The main star of the system has an effective temperature of approximately 5,050 K (Addison et al., 2019). It is classified as a K1V type star. A K1 star is with only 0.84 solar masses (Paredes et al., 2021) less massive than our Sun, which is a G2(V) type star with an effective temperature of 5,778 K (Carroll and Ostlie, 2014). Both the Sun and the star HD 189733 are 'main-sequence' (V) stars, where hydrogen burning takes place in the core. K-type dwarfs are interesting targets in the search for exoplanets (Lingam and Loeb, 2017).

The star HD 189733 is orbited by one known exoplanet HD 189733b, discovered in 2005 (Bouchy et al., 2005). The exoplanet orbits its host star in very close proximity, at about 0.031 AU (4.65 million km) (Rosenthal et al., 2021). This exoplanet is so close to its star, that one full orbit only takes 2.21857 Earth days Kokori et al. (2022). Therefore, temperatures at the planet's surface can be expected to be hot, and indeed, Addison et al. (2019) estimate an Equilibrium Temperature of around 1209 Kelvin. The exoplanet itself is by 1.13 times more massive than Jupiter (Stassun et al., 2017). With that mass and that equilibrium temperature, HD 189733b can be classified as a 'Hot Jupiter' (Ward-Thompson and Whitworth, 2011; Perryman, 2014; Zhu and Dong, 2021). Further stellar and planetary parameters are given in the Table 2.1 below.

The exoplanet HD 189733b is particularly well suited for theoretical and methodological studies (Zhu and Dong, 2021), especially for this thesis: Apart from the circumstance that our Solar System does not host this type of planet makes Hot Jupiters generally fascinating targets for observations (Birkby et al., 2013a), a Gas Giant's atmospheric envelope is very predominant and much easier to probe than that of a small rocky planet (Crossfield and Kreidberg, 2017) and it is one of the closest studied exoplanets (Madhusudhan, 2019). Many of its atmospheric species

Parameter height	HD 189733 Star	References
Mass $M_\star$ $(M_\odot)$	0.82785	Rosenthal et al. (2021)
Radius $R_\star$ $(R_\odot)$	0.78272	Rosenthal et al. (2021)
Distance (parsec)	19.7638 parsec	Exoplanet Archive
Stellar rotation velocity $v \sin i$(km/s)	3.5 ± 1.0	(Bonomo et al., 2017)

HD 189733b Planet		
Mass M_p (M_Jup)	1.166	Addison et al. (2019)
Radius R_p (R_Jup)	1.119	Addison et al. (2019)
Radial Velocity Amplitude K_p(m/s)	204.7 ± 2.5	Paredes et al. (2021)
Transit duration T (hours)	1.84 ± 0.04	(Addison et al., 2019)

Table 2.1: Overview of stellar and planetary parameters

have already confidently been detected: H_2O (Birkby et al., 2013a), Na + K (Keles et al., 2019, 2020), CO (De Kok et al., 2013) and many more (Exoplanet.eu Catalog). Brogi et al. (2016) measured winds and the planet's rotation period.

2.5 Atmospheric Corrections

Generally, an 'atmospheric correction' is required when a target cannot be observed directly, purely as it is, because its spectral fingerprint includes contaminating spectral features from a different source. These spectral features need to be disentangled, so that the true condition of the target can be inferred. A universal definition of an 'atmospheric correction' is not straightforward, because what is regarded as the contaminating species for one observer, might be the species of interest for another. Any 'correction' is thus dependent on research question.

The need for a correction of the images also depends on how the observation was made, specifically, in which range of the electromagnetic spectrum. Not all observations through or into Earth's atmosphere are equally difficult: in the gamma wavelength range, our atmosphere is completely opaque; gamma radiation is completely absorbed by the atmospheric constituents; his is also the case for radiation in the spectral ranges of X-ray, UV, infrared, microwave and radio, with a few exceptions (ESO). In the visual wavelength range, between 380 to 700 nm, most radiation can pass through. The gases of our atmosphere cause little or no absorption in this wavelength range. Because of its 'transmissivity' this range is called the 'atmospheric window' (Bessell, 2005). Earth's atmosphere leaves more than one window. Between the windows, our atmosphere is mostly opaque. Observing instruments are tuned to these specific window frequencies, or photometric bands. Earth Observation satellites observe in the B V R bands (in the visual range) and the Z Y J (H K) bands (in the infrared) (Nguyen et al., 2015; Neale et al., 2021). In

astrophysical observations, especially in exoplanet spectroscopy, the interesting bands are mostly the J H K bands in the infrared (Kerber et al., 2014; Birkby, 2018), but also the V and R bands (530 - 630 nm). These are also relevant for this study. The few absorption and scattering effects in this wavelength regime result mainly from Rayleigh scattering effects (Nguyen et al., 2015) and three atmospheric constituents: O_2, O_3 and H_2O (Noll et al., 2012).

2.5.1 Atmospheric constituents

The shape, depth and position of the telluric lines is a function of the volume mixing ratio of the absorbing molecules along the LOS. This, in turn, can typically be assumed a function of pressure and density (Ulmer-Moll et al., 2019). For well mixed gases, such as O_2, this is true. The relative concentration in the atmosphere is constant, therefore its very localised absorption bands in the visual atmospheric window vary in depth as a direct function of airmass (Bertaux et al., 2014; Kerber et al., 2014; Allart et al., 2022). O_3 can also be regarded as constant over the comparably short period of observation, and similarly its volume mixing ratio as a function of altitude and airmass. The absorption caused by O_3 in the atmospheric window is defined as a 'continuum absorption', which doesn't cause deep absorption lines at single wavelengths, but rather attenuates the overall radiation in a long stretch between 500 - 700 nm of the electromagnetic spectrum (Noll et al., 2012). The so called 'Chappuis absorption' occurs in the ozone layer (stratosphere). Observations with a short path-length through the atmosphere (with a small zenith angle) aren't affected as much as those with longer paths through the ozone layer (Brion et al., 1998). O_3 can therefore be disregarded in this study. H_2O, specifically water vapor is different. The volume mixing ratio is determined by temperature and pressure, as well as by weather conditions and atmospheric dynamics (Allart et al., 2022). A high concentration of water vapor along the line of sight causes considerable absorption, and Therefore, water vapor is the most challenging spectral component.

Water vapor

99% of the atmospheric water vapor is present in the troposphere (Ssenyunzi et al., 2020). Concentrations decrease with temperature, and therefore also with altitude. Ultimately, the concentrations are determined by the saturation-specific humidity of the air, which is influenced on a macro-scale by atmospheric dynamics, such as evapotranspiration, condensation and precipitation, and advection and turbulence (Trenberth, 1999; Randall et al., 2007). On a micro-scale, atmospheric water vapor responds to atmospheric dynamics, therefore changing with climate and season, with the diurnal cycle and with the topology of the surface. The spatial-temporal variability is therefore high (Diedrich et al., 2016; Ssenyunzi et al., 2020; Neelin et al., 2022).

The distribution of atmospheric water vapor shapes both local weather and climate, (i) by releasing latent heat and energy, when water vapor condensates to clouds (Randall et al., 2007; Ssenyunzi et al., 2020); and (ii) by absorbing the incoming solar radiation at infrared wavelengths (Randall et al., 2007). Water vapor is considered a highly potent greenhouse gas (Wang et al.,

2020; Intergovernmental Panel On Climate Change (Ipcc), 2023)(IPCC Assessment Report 6 2023). The prevalent assumption is that with rising global temperatures - due to rising levels of atmospheric CO_2 - the saturation-specific humidity of the air increases (Clausius-Clapeyron relation) (Dessler and Wong, 2009; Intergovernmental Panel On Climate Change (Ipcc), 2023). More water can evaporate, which in turn causes additional warming. The uptake of solar infrared (thermal) radiation is increased, and higher parts of the atmosphere are more opaque to the outgoing thermal radiation (Intergovernmental Panel On Climate Change (Ipcc), 2023). Additionally, water vapor can remain in the atmosphere for longer time spans (Hodnebrog et al., 2019; Wang et al., 2020) and transported over larger distances between source (evaporation) and sink (precipitation). This affects the entire hydrological cycle. With an increased availability of atmospheric water vapor, the likelihood of extreme precipitation events is growing (Hazeleger et al., 2015; Diedrich et al., 2016; Hodnebrog et al., 2019; Neelin et al., 2022). The human induced climate change due to higher levels of atmospheric CO_2 thus leads to a powerful 'water vapor feedback', which introduces large uncertainties (Dessler and Wong, 2009; Hazeleger et al., 2015; Windle et al., 2022). This includes a complex and still poorly understood net effect of clouds on the radiation budget (Intergovernmental Panel On Climate Change (Ipcc), 2023).

There is an urgent need for monitoring the distributions of atmospheric water vapor for the climate sciences (Schneider et al., 2010; Neelin et al., 2022; Windle et al., 2022). The inherent spatial-temporal variability complicates large scale spatial resolutions and mappings (Diedrich et al., 2016; Ssenyunzi et al., 2020).

In Earth Observation, and Space Observation, water vapor is the main contaminating species in the 'atmospheric window' and in the infrared, introducing a strong need to remove the absorption effects of water vapor from the observations (Nguyen et al., 2015; Neelin et al., 2022), which also requires a robust knowledge of its quantities along the observed LOS. In a spectrum, the absorption fingerprint of water vapor is complex: (i) the molecule is made up of three atoms (triatomic structure), and it can be present in all three aggregate states (Platt and Stutz, 2008; Bertaux et al., 2014); (ii) absorption occurs not only by collisions of photons with the component atoms (electronic transitions); it can also occur due to rotational and vibrational transitions of the molecules (Platt and Stutz, 2008), especially true for water in the gas phase. The spectral fingerprint is thus phase- and density dependent (Bertie and Lan, 1996; Pope and Fry, 1997; Bertaux et al., 2014; Kerber et al., 2014; Turchi et al., 2018). Atmospheric water vapor may be measured as precipitable water vapor (PWV), or total (vertical) column of water vapor (TCWV) in units of $kg\,m^2$ (Ssenyunzi et al., 2020).

The number of methods to correct for these absorption effects is vast and consistently growing. The continuous development of new correction methods seems to sway between two interests: accuracy and speed (of the corrections). All methods, however, can be divided in two major method types: (i) **Empirical methods** and (ii) **Model-based methods**.

2.5.2   Empirical Methods

Typically, Empirical Methods deal with the expected statistical behavior of different features that are present in the observed data, without prior data on the atmospheric conditions. An example for this is the 'Dark Object Subtraction' (DOS): this method is applied in Earth Observation in the Corrected Landsat Surface Reflectance product, available for download on the USGS Earth Explorer. This method considers the reflectance collected over a dark surface pixel as baseline reflectance due to atmospheric conditions and scattering. The baseline reflectance is used for calibration and is therefore removed from the other pixels in the same image (Liang et al. 2020 - CITE AGAIN). This method resembles the astrophysical correction approach using a 'standard star' for calibration. The star's spectrum is well-known, and ideally located close to target on the sky, being exposed to the same atmospheric absorption. It has to be observed in turns with the target over night, as described in (Husser and Ulbrich, 2013). The search for a 'common denominator', from which the amount of contamination can be inferred, can be done in various ways. These types of methods typically produces fast results, however sometimes with large remaining uncertainties (Ulmer-Moll et al., 2019). Approaches that reduce the uncertainties by iteratively removing only one systemic absorption share with the highest certainty each, such as SYSREM (Tamuz et al., 2005; Mazeh et al., 2006) can take a very long time to produce results (Allart et al., 2022).

2.5.3   Model-based methods

A model-based method generates a prediction of the contamination, based on the available information on the actual state of the systems, e.g. the atmosphere at the time of the observation. The transmission of the atmosphere corresponding to a certain atmospheric parameter can be simulated in a 'Radiative transfer model' (RTM) per wavelength per molecular contribution under various atmospheric parameter conditions as a 'line-by-line radiative transfer model' (LBLRTM)(Clough and Iacono, 1995). The result is a lookup table of a spectral response function at the sensor (Liang et al. 2020 - CITE AGAIN PROPERLY). In a correction approach, the observed spectrum might be fitted to any one of the spectral response functions in such lookup table, and the 'best fit' used for the correction of all other spectra/observations. Each spectral response functions corresponds to a specific atmospheric parameter condition; it is therefore computationally expensive to fit the observed data to all, and less expensive to fit to a sample of spectral response functions based on previous assumptions about the atmospheric conditions. Thus, knowledge of the atmospheric conditions improves the quality and accuracy of the fit (Smette et al., 2015; Kausch et al., 2015). The overall certainty of such a correction is typically higher than with an Empirical Correction approach. However, the model-based correction algorithms are often complex and offer limited applicability, or are time-consuming (Allart et al., 2022). The LBLRTM has been used in many succeeding modelling attempts. Several applications or pipelines, both in satellite Earth Observation and ground-based Space Observation build on the lookup tables of these models.

Generally, correction methods are tools. There is no single choice suited for all scientific pur-

poses. Advantages and disadvantages have to weighted against each other to find the appropriate correction type and method for the research question.

Chapter 3

Methodology

3.1 Study Region

The study area lies at 109.8719° East and 32.7016° North, the location of the telescope that provides the astrophysical observations, the Large Binocular Telescope in southeastern Arizona, USA. The telescope is installed on Emerald Peak on Mount Graham (also referred to as Pinaleno Mountains), at an altitude of 3220.8 meters (and a mirror altitude of 3268 meters). The observations were taken in the night of September 11 2021, from 02:17 am until 06:37 am. Relevant for this study are the atmospheric density and composition specifically along the line-of-sight (LOS) of the astrophysical observation. The Sky-position of the target is given as 20:01:39.99 (Apparent) Right Ascension (RA) and +22:46:18.83 (Apparent) Declination (DEC), observed at different Zenith Angles, between 11.251° and 35.849°.

The location of Mount Graham just between the Sierra Madre Occidental to the South (Mexico) and the Rocky Mountains to the North provide very dry conditions between November and April. The annual climate conditions are described as 'interior subtropical' with monsoon activity between July and August (Carrasco et al., 2017)(AROT Sub-millimeter Telescope).

3.2 Data sampling

3.2.1 Required data for the atmospheric research of Objective 1

The following data sets were used to determine the quantities of atmospheric water vapor for the time of the observation above the LBT.

Direct measurement

Some atmospheric parameters are measured directly at the Large Binocular Telescope. These include temperature, pressure and humidity in the telescope chamber. The variable of interest, however, is the total column integrated water vapor (TCWV). At many telescopes, this parameter is directly measured, for example at the Very Large Telescopes (VLT) on Cerro Paranal in Chile. Since 2011, the atmospheric water vapor over Paranal is monitored with a Radiometer (Kerber et al. 2012). The Low Humidity Atmospheric PROfiling radiometer (LHATPRO) by Radiometer

24

Physics GmbH measures the thermal radiation from the sky at microwave frequencies. It can derive the atmospheric water vapor content from the differential absorption in two frequency ranges. The LHATPRO probes the temperature of the atmosphere at $51.0 - 58.0$ GHz with the O_2 band; and with a second band at 183.31 GHz, where the atmospheric attenuation due to water vapor is very high, the LHATPRO creates a humidity profile (Kerber et al. 2012, Radiometer Physics GmbH). The LHATPRO is suited specifically for low-humidity environment (high altitudes, cold temperatures) with median humidity levels of 2.4 mm. The water vapor line near 183 GHz is easily saturated (100% opacity) at slightly more elevated amounts of PWV. Therefore, the more common instrument is the HATPRO, also by Radiometer Physics GmbH, where the water vapor band is located at 20-30 GHz.

The Radiometer typically scans the sky at different angles and thus different elevations to gradually retrieve a (humidity and temperature) profile up to an altitude of 12 km. The LHATPRO at the VLT, specifically, is able to scan the entire sky in just a few minutes. It is therefore suited to derive the PWV content in the line of sight (Kerber et al. 2012). In the employment phase, and continued in the first year of operation, the accuracy was inspected and successfully demonstrated with simultaneous radiosondes measurements with an precision for the radiometer PWV of 0.1 mm (Kerber et al., 2015).

A similar measurement can be employed on board of satellites, simultaneously with the scientific observation and in the LOS. The Envisat XML satellite carried the MEdium Resolution Imaging Spectrometer (MERIS) instrument until 2012. The two bands - H_2O and O_2 - at microwave frequencies measured the differential absorption and create temperature-humidity profiles alongside the observations of other instruments on board of the satellite (Rast et al., 1999). Special Sensor Microwave Imager/Sounder (SSMI/S) on board the United States Air Force Defense Meteorological Satellite Program measures water vapor absorption at 22.24 GHz (and differential absorption from 19.35–85 GHz) above the ocean, where the PWV content along the LOS is large (Kunkee et al., 2008). The Sentinel-3 satellites, which are discussed in Section 3.2.1, also carry microwave radiometers (Preusker et al., 2021). The measurement concept is well established, and well suited for providing the variable of interest. However, not all telescopes are that well equipped, or financially able to upgrade their instrumentation in the same manner. And the LBT does not have such instruments installed.

The Telescope is not isolated on Mount Graham. In a distance of merely 120 m, the Arizona Radio Sub-millimeter Observatory Telescope is located. Observers wishing to obtain data on the 'seeing conditions' are referred to this observatory, which in fact hosts a TAU radiometer. Albeit, the purpose of the instrument is to measure the sub-millimeter observing conditions, and therefore the atmospheric opacity at an H_2O absorption band at 225 GHz. At this frequency, the main contributor to H_2O absorption is not by water vapor, but just as well by water ices or super-cooled liquid water droplets. Both can be found in clouds. Therefore, the TCWV cannot be immediately inferred from atmospheric opacity at 225 GHz (Kunkee et al., 2008; Kneifel et al., 2014; Carrasco et al., 2017). Nonetheless, the available data was used to establish the typical - overall - atmospheric conditions and seeing conditions and can be interpreted as PWV, but not as TCWV. The data was provided as a yearly 224 GHz opacity values and opacity stats, and

was obtained from AROT Sub-millimeter Telescope.

The other atmospheric parameters - temperature, pressure, humidity - were also attempted to obtain independently from NOAA (National Oceanic and Atmospheric Administration). The nearest meteorological station maintained by NOAA is 'Noon Creek', which is also located on Mount Graham, approximately only 5 km distanced (at 32.6678° North, 109.7881° West and at an altitude of 1501.1 m (NOAA). However, the meteorological data request produced only an empty data set. The respective time frame was apparently not covered.

Water vapor absorption can also be derived from signal delays between Global Navigation Satellite System (GNSS) receivers. The delay of signals between the space-based GNSS instruments and the ground-based receivers GNSS receivers holds information about the atmospheric conditions along the LOS between two receivers (Preusker et al., 2021). This correlation of signal delay and tropospheric conditions was established by (Bevis et al., 1992). The 'Wet Delay' between two space-based GNSS receivers this is called 'GNSS radio occultation', which provides insight into the upper-tropospheric and lower-middle-stratospheric conditions (Niell et al., 2001; Cardinali and Healy, 2013). The 'Wet Delay' between a ground-based and a space-based GNSS receiver (altitude up to 800 km) can be interpreted as a vertical PWV column (Bevis et al., 1992), integrated from the PWV along the LOS between the receivers with simple geometry (Platt and Stutz, 2008). This so called 'Zenith Wet Delay' (ZWD) makes up only one fraction of the 'Zenith Total Delay' (ZTD), which is caused both by dry gases of air - this is referred to as the 'Zenith Hydrostatic Delay' component (ZHD) - and by water vapor, which is the wet component. The ZHD is directly proportional to the surface temperature and pressure (Bevis et al., 1992; Niell et al., 2001; Klos et al., 2018) and is the main contributor to the ZTD (Ssenyunzi et al., 2020).

The data derived from GNSS Radio occultation measurements makes up only a small percentage (3%) of the database that is used for ECMWF Forecasts (3.2.1), but delivers highly valuable data (Cardinali and Healy, 2013; Ssenyunzi et al., 2020; Wood-Vasey et al., 2022). The amount of ground-based atmospheric water vapor measurements derived from the GNSS 'Zenith Wet Delay' makes a major impact in ECMWF Forecasts (Wood-Vasey et al., 2022) and can in fact serve as a cost-efficient means of uninterrupted measurement with a high and dense temporal coverage and spatial resolution, albeit providing only point sources of data (Ware et al., 2000; Ssenyunzi et al., 2020).

Via the University Corporation for Atmospheric Research (UCAR) and their real-time national GPS network *U.S. SuomiNet*, large amounts of raw data 'Zenith Wet Delay' are made freely available as Hourly products (UCAR/COSMIC) (Ware et al., 2000). The uncertainties are estimated from other studies in the orders of $1 - 2\,\mathrm{km\,m^2}$ (Preusker et al., 2021). The closest GPS receiver to the location of the study area is situated in Safford, Arizona, at a distance of approximately 20 km (and an altitude difference of approximately 2000 m). Data was downloaded for 72 hours within the three dates 10, 11 and 12 September 2021. However, the data showed a huge gap of several weeks, exactly around the time of the observation. Before 20 July 2021 and

after 21 September 2021, data was continuously available from this station. The lack of coverage lead me to use a different approach.

Indirect Alternatives

With direct and independent measurements not available, the following section describes the data that was used to establish the atmospheric conditions indirectly for the time and location of the observation. These following multiple data sets can provide either a good temporal coverage over the time of the observation, with the downside of a low or unfortunate spatial resolution; or a very good spatial resolution of TCWV data directly for the location of the LBT, with the downside of a very low or unfortunate temporal resolution. The combination of the available data sets can increase the certainty for the attempted atmospheric water vapor assessment.

European Centre for Medium-Range Weather Forecast (ECMWF)

The European Centre for Medium-Range Weather Forecast (ECMWF) is both a research institute as well as weather service; it is the largest weather service for global numerical weather forecast and climatology. The wide range of services and data sets are provided through the EU platform Copernicus Open Access Hub.
(i) The ECMWF 'Integrated Forecasting System' (IFS) combines a global numerical Earth system and weather model with a large database of recent weather observations to create a short (18 hour) Forecast product. This product is continuously created. This product may be used in the time-critical processing of data, for example in the atmospheric correction of time-critical satellite imagery, downloadable via the 'Copernicus Open Access Hub'. If the use-case is non time-critical, however, the processing, including the atmospheric correction, is typically based on a different ECMWF product:
(ii) The 'ECMWF Analysis' is based on the same global numerical Earth system and weather model. At the point where the ECMWF Analysis is created, the predicted weather forecast can be assimilated with the actual measurements. This is done twice daily (for 06 and 18 UTC). This data can be downloaded from the Copernicus Open Access Hub for any point of time - the delivered data will be interpolated from the two analysis windows (ECMWF, 2020a). The total column vertically-integrated water vapor (TCWV) values are expressed in units of $kg\,m^2$. This amount represents the mean column density within a gridded area. The ECMWF analysis is produced for a latitude-by-longitude resolution (ECMWF, 2020b). The user can request the analysis data at any grid size. This will simply be interpolated from the original resolution.

The weather observations, that contribute to the ECMWF analysis make use of a number of data source: (i) various clear-sky satellite radiances (in infrared and microwave frequencies) provide values for temperature, humidity, precipitation and ozone (ECMWF, 2021) - the Sentinel 3 satellites (3.2.1) are not part of the used ECMWF satellite database; (ii) all-sky microwave radiances (from GNSS receivers, dropsondes, radiosondes to weather balloons) provide water vapor data (ECMWF, 2021) - with the derivation of water vapor from radio occultation of GNSS satellites even up to the ionosphere (800 km) (Vespe et al., 2005; Cardinali and Healy,

2013); and (iii) ground-based radar precipitation composites are assembled from buoys, ships and even air craft data (ECMWF, 2021). ECMWF additionally rely on the database of the World Meteorological Organization, which collects regional weather data, for example from NOAA and similar institutions. Thus, this data will ultimately be a part of the ERA5 reanalysis. The data availability of weather observations is directly proportional to the quality of the forecasts (ECMWF, 2020c). The amount of data availability has gradually grown since the 1970s (Hersbach et al., 2019). Ingleby et al. (2021) demonstrated successfully, that the reduced data availability during to Covid-19 lockdowns, resulting from reduced air craft traffic negatively impacted the forecast accuracy.

The data used in this study is the 'ECMWF Analysis product', which was downloaded from the Copernicus Open Access Hub, alongside the OLCI data, and therefore resampled to the spatial resolution of the OLCI data of 300 x 300 m for one daily value at 17 h (3.2.1).

ERA5: ECMWF's 5th Re-Analysis

ERA5 is a comprehensive global atmospheric re-analysis, produced by ECMWF and developed by the Copernicus Climate Change Service (C3S) (Hersbach et al., 2020; Bell et al., 2021). ERA5 is based on the same global weather model as the ECMWF Forecast and Analysis products. It combines the global weather model - similar to the 'ECMWF Analysis' - with the latest observations. In the re-analysis, however, all pixel values are aligned with their historic data from 1940 till current, and are in agreement with all surrounding pixels. The ERA5 data is therefore much less sensitive to measuring errors than the 'ECMWF Analysis'. All ERA5 products are based on the same global weather model (of the 5th generation), replacing the last ECMWF-Re-Analysis (ERA-Interim). The Re-Analysis is computationally very expensive; its production takes up to five days. Similar to the 'ECMWF Analysis', it is provided for two assimilation windows of 12 hours each - either from 09-21 UTC or 21-09 UTC. The data in the middle of the assimilation windows shall therefore be considered to have the lowest uncertainty (Hersbach et al., 2020).
In another consequence of the high computational expense, the data is assimilated onto a longitudinal/latitudinal grid. At the location of the LBT ($32°$) a grid cell of this resolution covers an area of 96.5 km^2. Again, the user can request the data down-sampled to any resolution. A resolution of $< 0.25°$ is not recommended to avoid the risk of oversampling (Ssenyunzi et al., 2020; Bell et al., 2021).

This study makes use of the 'ERA5 hourly data on single levels from 1940 to present', which is downloadable via the Climate Data Store (CDS). The downloaded variable was TCWV, expressed in units kg m^2, downloaded for a total of 72 hours between Sept 10, 00 am C to Sept 13, 00 am. The hourly values are interpolated from time intervals of the two assimilation windows, at the recommended 'maximum' resolution of 0.25 x 0.25° in longitude and latitude (for an area of 31km m^2.

OLCI

The Ocean and Land Colour Instrument (OLCI) is one of four instruments on board of the Sentinel-3 European Earth Observation satellite mission. Observing ocean and land surfaces and supporting ocean forecasting systems is only one half of the instrument's mission. Its second direct research objective is the accurate retrieval and description of the atmosphere, to enable environmental and climate monitoring. In view of its importance as a greenhouse gas in climate change research, the retrieval of the TCWV is a primary focus (Preusker et al., 2021). The instrument measures the radiance of Earth's surface with 21 sensor-bands in the visible and near-infrared spectral range (between 390 and 1040 nm). Two of those are designated water vapor absorption bands (19 and 20). Products of different processing levels can be downloaded from the Copernicus Open Access Hub, where Level-0 is the raw data, Level-1 the geo-referenced Top of Atmosphere (TOA) radiance and Level-2 the processed data. This is already 'corrected' for gaseous absorption and provides data on all measurable geophysical surface properties, respectively on the removed and corrected atmospheric properties. One of these Level-2 products can be read as TCWV estimate per pixel (Sentinel 3 OLCI).

The satellite is on a low near-polar and sun-synchronous orbit: *low* refers to the orbit reference altitude of 814.5 km - which places it in in the Exosphere; *near-polar* indicates the orbit inclination: the orbit is tilted at almost 90° towards the equator. The apparently inclined path over the surface is a result of Earth's daily rotation; *sun-synchronous* defines an orbit where the equator is crossed at 10:00 h Mean Local Solar Time to guarantee that the solar radiation illuminates the surface always at the same angle. The location of the study area is scanned once per day per satellite, at 17 h (A) and 17h30 (B) in the afternoon (Sentinel 3 OLCI) (Kalakoski et al., 2022).

The 21 sensor-bands provide a spectral resolution of $\Delta\lambda = 1.25$ nm (R = 520). In an orbit reference altitude of 814.5 km and a field of view of 68.6° the satellites can cover a 1440 km swath; with a sampling period of 44 ms this produces a spatial ground resolution of 300 x 300 m per pixel in Full Resolution mode - the Reduced Resolution was not used in this study (Sentinel 3 OLCI).

Although there is already a dedicated Level-2 product available, Preusker et al. (2021) propose a corrected and expanded processing scheme to isolate the TCWV from the observations. The standard Level-2 TCWV processing scheme employed at 'Copernicus' has already been found to systematically overestimate TCWV measurements over land by up to 11%, compared to selected ground-based reference data (Preusker et al., 2021). Therefore, this study uses the Level-1 product, which was processed in the suggested manner - described below - by Dr. Preusker as an alternative 'Level-2' product and provided to me as data set.

The standard L2 OLCI TCWV product indicates a maximum likelihood estimation of the water vapor column over a cloud-free pixel. This is derived from the 'differential optical absorption spectroscopy' (DOAS) of the water absorption band (Oa19), compared to the reference bands (Oa17, Oa18), where water is non-absorbing and the measured reflectance a function of the

surface albedo (Sentinel 3 OLCI). The column densities from the atmospheric transmission in the spectrum are produced with a radiative transfer (RT) simulation in the form of a lookup table. The 'maximum likelihood TCWV' arises from a comparison of the RT-simulated column densities and the measured OLCI TCWV quantities (Diedrich et al., 2013)(Sentinel 3 OLCI). The differential absorption technique in the way that it's used in the standard Level-2 TCWV product - with two reference non-absorption bands instead of one - has already been able to reduce uncertainties (Diedrich et al., 2013).

The alternative Level-2 product used in this study was produced in a '1D Var approach' (Preusker et al., 2021). This is a slight alteration of the standard Level-2 procedure. This approach also makes use of a RT-simulation lookup table, produced for a range of multiple atmospheric conditions; they apply additional correction coefficients from a previous study (Diedrich et al., 2015), and normalised TOA radiances (to compensate for variances of the solar flux). The first guess of the atmospheric state parameters is based upon the non-time-critical ECMWF Analysis. Again, the 'maximum likelihood estimate' is estimated from a comparison of the OLCI TCWV measurements and the RT-simulation lookup table; in their approach, the variances between TCWV measurements and first assumed atmospheric state parameters are iteratively reduced, both by their column densities and their radiances. The proposed '1D Var approach' yielded indeed better results in their validation study, reducing the overestimation of TCWV to 2-3% (Preusker et al., 2021).

The available data on Copernicus Open Access Hub comprised the Level-1 satellite images from Sentinel 3A and 3B satellites for the dates September 10, 11 and 12 2021. Downloaded were those images, where the pixel at the location of the LBT was cloud-free, which resulted in four available satellite images. They were downloaded in Full Resolution - with a pixel size of 300x300 m. These were converted to a Level-2 TCWV product by Dr. Preusker and provided to me.

TAPAS

TAPAS (Transmissions of the AtmosPhere for AStromomical data, or Transmissions Atmosphériques Personnalisées pour l'AStronomie) is a web-based service, directed at the astrophysical community. It provides simulated transmission spectra of Earth's atmosphere that can be subtracted from ground-based astrophysical observations (Bertaux et al., 2014). Users can request such simulated atmospheric transmission spectra. This transmission spectrum is simulated for the sky angle of the observation and specifically for the time of the observation through AERIS, a data and service center for atmospheric data in France. In that request, the user specifies the observational parameters - time, location (longitude, latitude, altitude) and zenith angle (RA-DEC). TAPAS obtains the respective atmospheric profile from the non-time critical ECMWF analysis product, interpolated to the time of the observation from within the ECMWF 12 hour analysis windows (06 UTC and 18 UTC). The atmospheric profile - integrated over the angle of the LOS through the atmosphere - and the respective transmission spectrum are simulated for the different requested molecules based on the Line-By-Line Radiative Transfer

Model (LBLTRM) code (Clough and Iacono, 1995) and the high-resolution transmission molecular absorption database (HITRAN) (Rothman et al., 2009, 2013; Gordon et al., 2022). The simulated transmission model is convoluted with the instrumental resolution (which the user indicates in the data request), so that the simulated transmission and the observations share the same wavelength grid (Bertaux et al., 2014).

This study makes use of the simulated extinctions for H_2O, O_2, O_3 and Rayleigh scattering in a spectral resolution of (2.8), in the same spectral range as the PEPSI observations: 530 to 630 nm. Since the first and last PEPSI observation are merely 4 hours apart, they fall into the same 12 hour ECMWF analysis window. The simulated TAPAS transmissions were requested only for the times of the first, middle and last observation, for 02:17 am, 04:25 am and 06:37 am , since requesting more than three simulations would not have added scientific value to the analysis (ECMWF, 2020a).

3.2.2   Data for the Telluric Correction and Objective 2

The data used for the second objective - conducting and assessing the performance of a telluric correction with the proposed new Empirical Correction Method - comprises the observational data of the stellar system HD 189733. The system was observed during the night of September 11, 2021, between 02:17 am and 06:37 am . Within the observing period, a total of 59 spectra were collected with an exposure time of '00:03:20.000' for each image. 27 observations captured one full transit of the exoplanet HD 189733b; the other 32 observations were taken before and after the transit occurred. The time of the observation was aligned with the transit occurrence: the last observed transit and the current state of knowledge of the system's orbital parameters allow a precise calculation of the transit timings. The data was provided by Prof. Poppenhäger at the Leibniz Institute for Astrophysics (AIP), after the standard reduction process; this includes a wavelength calibration and the removal of the inherent system velocity of the observer relative to the star (of 11841.212 m/s) (Strassmeier et al., 2017). The spectra were aligned to a common wavelength grid, which has been demonstrated to reduce instrumental effects (Brogi et al., 2013). The system was observed by the Large Binocular Telescope (LBT), which is an optical telescope with two identical 8.4 m primary mirrors (Figure 3.1). The LBT is operated in binocular mode, which results in a combined collecting area corresponding to a single 11.8 m (LBTO). The spectroscopic measurements of the system were performed by the Potsdam Echelle Polarimetric and Spectroscopic Instrument (PEPSI), which is a high-resolution spectrograph installed directly at the LBT (Strassmeier et al., 2015, 2017). PEPSI has six cross-dispersers (CD), two of which can be used during the same exposure. The spectra used in this study were collected on CD4, which diffracts in the spectral range from 5441 - 6278 Ångström, with a resolving power of R=130,000. The collected spectra had a high continuum signal-to-noise ratio of 382 per pixel. The PEPSI spectrograph is installed in a closed chamber below the mirrors, where temperature, pressure and humidity are kept constant to ensure stable collecting and read out conditions; the light is fibre-fed to the spectrograph. This instrument setup is shown in the Figure 3.1.
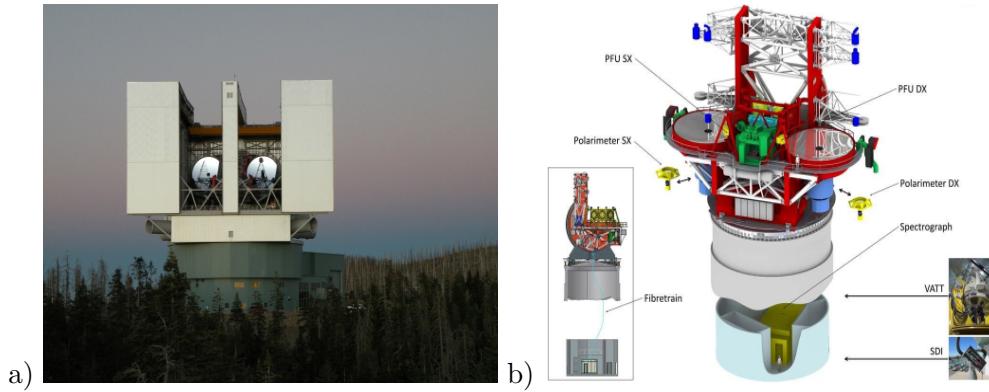
Figure 3.1: (Left) The Large Binocular Telescope LBT (Image credits: EIE group); (Right) and the integrated PEPSI instrument (Strassmeier et al., 2015).

3.2.3 Additional data for the astrophysical assessment of Objective 3

The following paragraph describes the data that was used for Objective 3, thus to assess and even to quantify how much of the faint exoplanet signal, that is hidden among all other much more dominant spectral features, remained intact with the Empirical telluric correction method. And respectively, whether (and if so, how much) the Telluric correction accidentally removed absorption lines of exoplanet origin.

Benchmark: Synthetic spectrum with artificial exoplanet absorption features

The PEPSI spectra that are already used for Objective 2, contain an artificial signal that was integrated into the observed data. This serves as a benchmark for the performance of the Correction Method. Any possible attenuation of the signal can be quantified precisely. This artificial signal mimics the transmission fingerprint of an exoplanet atmosphere. Although the PEPSI spectra already include the spectral fingerprint of an exoplanet atmosphere, the knowledge of the strength of these spectral features is not known as precisely as the spectral features that were incorporated. Therefore, 'false positives' can be minimized (Mazeh et al., 2006; Birkby, 2018; Keles et al., 2022). The artificial transmission spectrum includes both (i) scientifically realistic absorption features (at wavelengths where molecules would cause absorption) and (ii) absorption features that were placed at strategically significant locations, where discriminating effects are to be examined. Simulated was one exoplanet transmission, that was integrated into the observed data at three different orbital velocities - for an exoplanet on a fast orbit ('F'), medium-fast ('MF') and slow ('S') and resulted in three synthetic data sets that were processed and analysed in the same manner. The artificial transmission was incorporated into the PEPSI data by Prof. Poppenhäger, with an approach that was described in detail in Seager (2014).

3.3   Data processing steps

3.3.1   Determining the total column atmospheric water vapor

The measurements of atmospheric water vapor were obtained from various sources. These provide the data in different spatial and temporal resolutions, ranging from a dense temporal coverage and a large spatially unresolved area, to point sources of (spatial/temporal) data. To combine the data for an increased understanding of the properties of atmospheric water vapor for the time and location of the observation, the TCWV values need to be adjusted in the following manners.

Visual examination in SNAP

The first visual examination of the OLCI data was done in the SeNtinel Application Platform (SNAP), which is an open access environment for processing and analysis of Sentinel (and other) satellite sensor data, provided by ESA. The visual examination of the pixel grid distribution around the location of the LBT helped select the most suitable pixel; with a pixel size of 300 x 300 m, the LBT can be located anywhere from the center of the pixel to the pixel edge. With the location of the LBT on Emerald Peak on Mount Graham, where elevation can also change considerably within a pixel of 300 x 300 m, a selection purely based on coordinates might place the LBT in a non-representative pixel. This can was avoided by visual examination and a deliberate choice of the most representative 'LBT-pixel', based mostly on elevation.

Adjusting for altitude

The altitude of the OLCI pixels represents the average altitude of all surfaces within the pixel. The TCWV values of the Level 2 product are delivered after the atmospheric correction for the entire pixel, and for the average altitude of that pixel. For pixels on large flat surfaces with little altitude variance within, this is very accurate. However, on mountain tops, such as Emerald Peak on Mount Graham, the altitude varies significantly within an area of 300 x 300 m. The TCWV re-analysis quantity holds true only for the average altitude and thus only gives an average TCWV quantity. The TCWV quantity for the true height of the LBT location within that pixel WV_{LBT} can be derived from that, as a function of water vapor per altitude as follows (Platt and Stutz, 2008):

$$WV_{\mathrm{LBT}} = WV_{\mathrm{mean}} + \frac{\Delta WV}{\Delta h}\left(h_{\mathrm{mean}} - h_{\mathrm{LBT}}\right), \tag{3.1}$$

where WV_{mean} is the average TCWV measured by OLCI for the LBT-pixel and its surrounding 8 reference pixels; h_{mean} is the average height indicated by OLCI for the LBT-pixel and its surrounding 8 reference pixels; and h_{LBT} is 3268 m; Δ_{LBT} and Δ_{h} give the sum of the difference of each surrounding reference pixel value to the LBT-pixel value.

Transformation of Vertical Column Density to Slant Column Density

All measured or analysed TCWV values ultimately describe the physical properties of a Vertical Column Density (VCD) of the atmosphere. Observed was the target always at an angle through the atmosphere, thereby increasing the path-length and airmass in the LOS. The true physical properties of a Slant Column Density (SCD) of the true observation geometry can be calculated, following the 'Differential Optical Absorption Spectroscopy' (DOAS) approach. This is typically applied vice versa: to translate the physical properties for the measured SCD of an observation to a VCD. The relation of the geometries can be used for a translation from and to either direction (Platt and Stutz, 2008):

$$\sigma_\theta = AMF\,\theta\,\sigma_0, \tag{3.2}$$

where σ_θ calculates the SCD, from the VCD σ_0, which has an angle of $0°$ toward the solar zenith angle, from the observed zenith angle θ and from the airmass factor AMF, which is assumed as $\frac{1}{cos}$ since no significant multiple scattering effects have to be considered for this type of observation (Platt and Stutz, 2008).

3.3.2   Telluric correction processing steps

The following chapter describes how the proposed Empirical Telluric Correction approach is using the inherent properties of the observational data and how the approach itself is implemented.

Stellar rest frame

The method requires that 'movement' and Doppler shifts of spectral signals only (or mainly) arise from one moving system, as if the observer had been tied to the star and its motion. Therefore, the observations were calibrated and shifted, so that the spectral absorption features caused by the star always displayed at the same wavelength position. This is called a 'stellar rest frame'. As the radial velocities of the star and Earth are not that different, the telluric absorption features remain virtually stationary as well (Brogi et al., 2018).

Assumptions for the Empirical Telluric Correction Method

This Empirical Telluric Correction method is based upon (i) the inherent radial velocity differences of multiple objects in motion, that contribute to the same spectrum of an observation, and (ii) the different behaviors in a time series of observations. Whereas the spectral features of Earth and the star undergo only small velocity changes in a time series over the course of a few hours, the transiting exoplanet is observed with both large radial velocities, and major radial velocity changes (Birkby et al., 2013a; Ivanova et al., 2023).
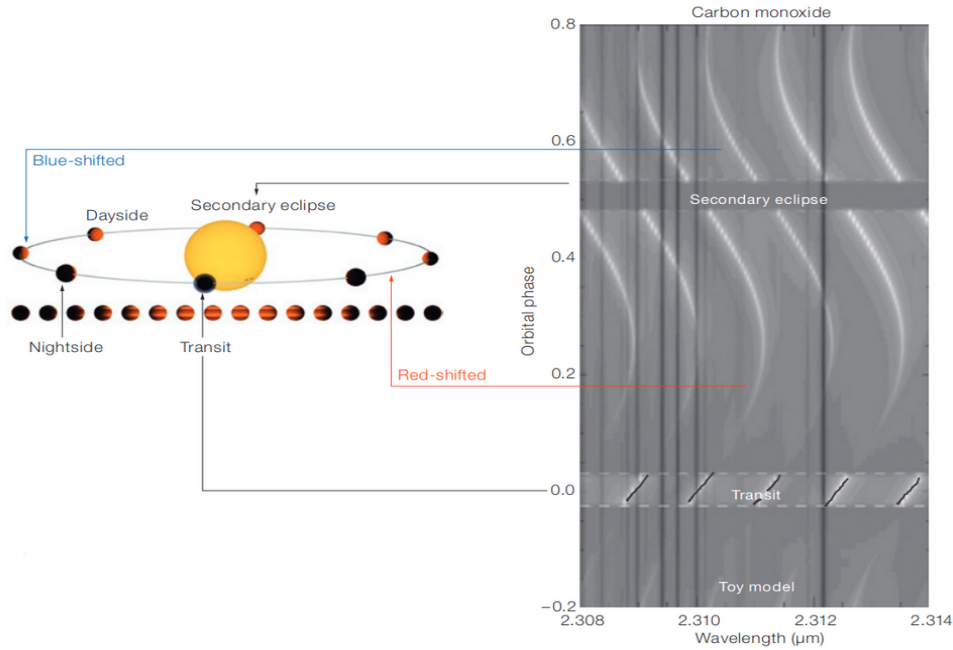
Figure 3.3.2. Time series ob observations of a star with an exoplanet. It shows bright emission features reflected from its dayside and dark absorption features from its atmosphere during transit. The time series covers one entire orbital period (Earth analogue: one year). Each column on the x-axis represents one observation - one spectrum. The image was adapted from Birkby et al. (2013a).

Illustrated in Figure 3.3.2 above is the toy-model of an entire orbital Phase of an exoplanet in a time-series of observations of its star. The dark vertical stripes are the absorption features of a star (or Earth), calibrated to always appear at the same wavelength position in a time-series of observations. The wavy features belong to an exoplanet, moving through the time-series at a very specific amplitude. Here, it adds bright emission features whenever its dayside is visible, illuminated by the light of its star, just like a full (or crescent) moon. During transit, dark absorption features from its atmosphere are visible. The spectral features of an exoplanet moving towards the observer appear blue-shifted, and away from the observer red-shifted, as seen in the Figure 3.3.2 above. At the orbital phases 0.75 and 0.25, the planet has its largest radial velocity. In a spectroscopic time series, the features of the exoplanet will appear displaced/Doppler shifted furthest away from their actual wavelength position. During the transit, around Phase 0.0, most of the planet's movement is lateral, with little to no components of the movement along our LOS. At 'mid-transit', the exoplanet's spectral features won't appear shifted at all. Just before and just after the transit mid-point, however, the rate of velocity change is strongest - from a positive to a negative radial velocity. Therefore, as seen in Figure 3.3.2, the planet's spectral features appear closest to their true wavelength position at transit, but also tilted at the steepest angle towards the stationary spectral lines of the star (or Earth). The PEPSI observations of HD 189733(b) cover the Orbital Phase from -0.1 to 0.1. The above Figure was shown for orientation, and to illustrate what Doppler shifts of the exoplanet signals can be expected in a time-series that has been calibrated into a 'stellar rest frame'. Exactly this tilt is what the Empirical Telluric Correction Method will exploit (Keles et al., 2022).

The Telluric Correction Method is basically used for normalising for expected trends in a time series of observations. Relevant is (i) a distinct trend of the exoplanet's spectral features, which appear (during transit) at a different wavelength in each observation; and (ii) the trends that the stellar or telluric absorption features experience over the course of the night. As they have been calibrated to a stellar rest frame, they will be displayed at the same wavelength in the time series. However, both sets of lines undergo specific changes over the course of the night: changes of flux. The light collected at a pixel that was calibrated to a stellar absorption line will be attenuated during the 'in-transit' observations, because a fraction of the stellar surface is blocked and the overall luminosity decreases. Pixels calibrated to a telluric absorption line will also vary over the course of several hours. During this time, the telescope will follow the star's apparent position on the sky, which changes with Earth's diurnal rotation velocity. With a changing observing angle, the length of the LOS and the airmass varies. Therefore, the absorption caused by telluric molecules (and the flux collected for that pixel at the CCD) decreases or increases relative to the airmass. Pixels calibrated to both stellar or telluric lines undergo these small but distinct temporal changes (Keles et al., 2022).

Correcting with a Univariate Smoothing Spline Interpolation

This study investigates the effectiveness and limits of an approach that was used successfully in a previous study by Keles et al. (2022), where they applied the method to correct for telluric contamination, based on an approach used in the standard reduction process for PEPSI observations. This is done by Dr. Ilyar Ilyin at the AIP, and further described in Strassmeier et al. (2017).

(1)
At first, we fit a 'Univariate Smoothing Spline Interpolation' to the flux curve of the each pixel over the course of the night. A Spline is a piecewise polynomial function with multiple segments. Each segment is defined by a polynomial function of a chosen degree, by default assumed to be cubic. The shape of the Spline Curve is determined by where and how the different adjacent polynomial segments meet, which happens at 'knots'. These 'knots' need to fulfill several conditions: a classical Spline has continuity, which means that the 'knot' values of two adjacent segments are the same; typically also the first derivatives are identical. conditionality of the 'knots' is what makes Spline Interpolations superior to a simple Polynomial Regression. As the Figures 3.2 below demonstrate, the latter fits either only loosely to the data by interpolating a low-order Polynomial (left); or it fits closely with a high-order polynomial degree, which often leads to excessive oscillations (overhanging wiggles) (middle). This is called 'Runges Phenomenon'. A Spline Interpolation avoids this, because (i) the 'knot' conditions ensure continuity between two segments, and (ii) each segment is described by its own low-order polynomial function, somewhat independent of the other segment's functions (right) (Akima, 1970; Murtagh and Heck, 1987; Cheng et al., 2007; Phillips, 2011).
A Smoothing Spline is characterized as a Spline that does not need to go through all data points. It can therefore be used as a variance reduction technique, for example to fit a polynomial regression to the basic trend of the data (Vacca et al., 2003; Phillips, 2011; Keles et al., 2022).
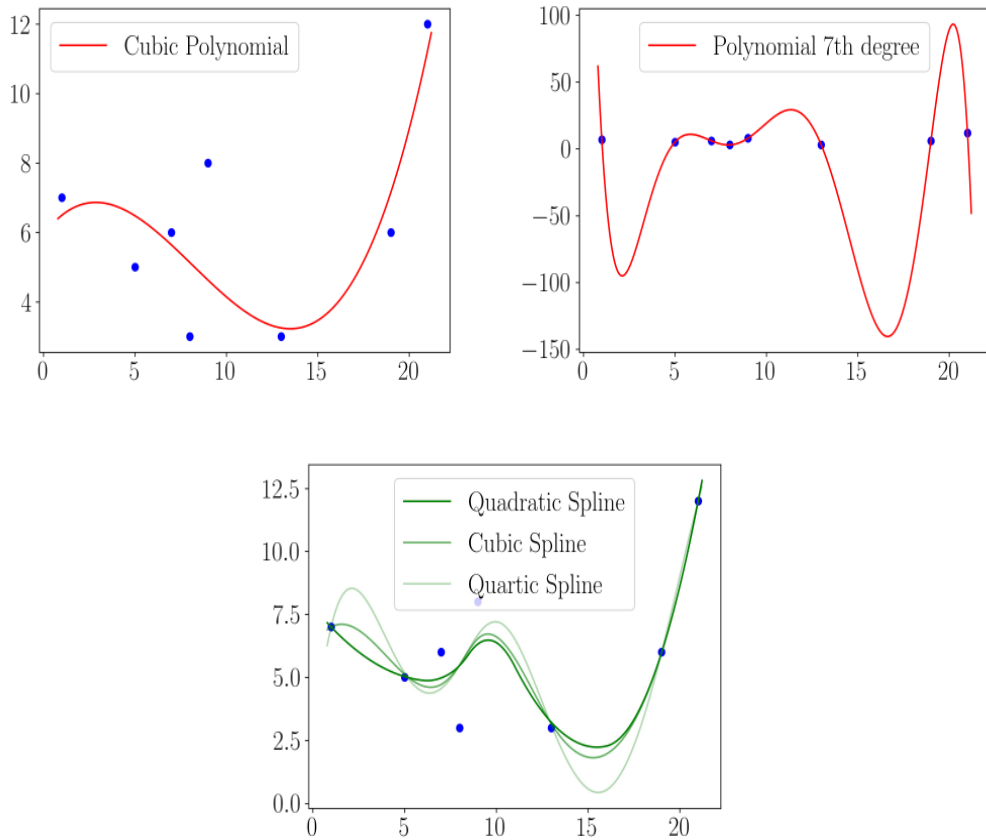
Figure 3.2: Polynomials (red) versus Splines (green). Own illustration.

The smoothing condition (the polynomial degree of the Smoothed Spline) also specifies the number of knots. 'Univariate' refers to the parameter dimensions relevant to the Spline, which is solely the flux of a given pixel, opposed to a 'multivariate' analysis that's typically used to describe the relationships between parameter dimensions (Murtagh and Heck, 1987).

(2)

In a second step, the interpolated curve of the Univariate Smoothing Spline is used to normalise for the detected trends of the pixel flux curves. Each pixel (in each observation) is divided by the Spline function of its pixel curve. The assumption is that telluric and stellar trends are largely removed, and what remains is each pixel's deviation from its over-night-trend. Such a deviation would be either noise, or, for example, an exoplanet's spectral feature appearing on a pixel - contrary to the typical trend of that pixel flux curve, and therefore 'overlooked' by the Univariate Smoothing Spline Interpolation (Keles et al., 2022).

Although the common default polynomial degree for Splines is cubic, there is no previous study that firmly compared the efficiencies of cubic Splines versus other polynomial degrees. Whereas (Strassmeier et al., 2017) applied the Spline with the default cubic degree, Keles et al. (2022) used a second-order quadratic Spline. In my understanding of a Spline, even a lower-order polynomial degree (for example a second-order quadratic polynomial) should be capable of

providing a close and smooth fit of the various - quadratic - segments to the data; and similarly, even a slightly higher-order Spline with a quartic polynomial degree should be robust enough to avoid excessive oscillations because of the knot conditionality. Therefore, this study applies three Splines with different polynomial degrees - quadratic, cubic and quartic - to the pixel curves and pixels, and compares the yielded results.

3.3.3   Preparation for Analysis

To analyse the exoplanet's spectral features before and after the Spline Correction, we need to be able to look at the exoplanet alone. Up until now, the exoplanet's signal appears during transit on a different spectral pixel in each observation, in a fixed stellar rest frame. The spectra can just as well be calibrated differently, for example in the exoplanet's rest frame. To shift all observations (before and after the Spline Correction) so that the exoplanet features are aligned, each spectrum needs to be Doppler shifted by the same Doppler shift that the artificial exoplanet experienced at this Orbital Phase.

Doppler shifting and aligning the spectra into an Exoplanet Rest Frame

Doppler shifting a spectrum by Radial Velocity is not a uniform shift towards the blue or red direction. As explained in Section 2.2.2, the amount of Doppler shift is wavelength dependent. For example, a radial velocity of $-23.681 \, \mathrm{km \, s^{-1}}$ will cause a larger Doppler shift in the bluer part of the spectrum: an absorption line originally located at 6200 Ångström will be Doppler shifted by 0.49 Ångström (towards the blue); an absorption line originally located at 5800 Ångström will appear Doppler shifted only by 0.46 Ångström.

Retrieving the Exoplanet Transmission from the Spline Corrected time series

The exoplanet transmission can be isolated from the remaining noise after the Spline Correction - and from the remaining stellar or telluric residuals, that appear now tilted towards the exoplanet's lines at a different wavelength in each observation. The exoplanet transmission spectrum can be retrieved from the 'in-transit' observations. Necessary for the purpose of this study was merely the average retrievable exoplanet signal. Less important was how the exoplanet transmission changed at different Phases of its transit, albeit this would typically be of interest for a further analysis of the physical properties of the exoplanet's atmosphere. The residual flux per pixel per spectrum after the Spline Correction should reflect only (i) the exoplanet's absorption behavior at this wavelength and(ii) noise - even if resulting from any uncorrected stellar/telluric residuals, now affecting a different pixel in each observation. Therefore, the 'average in-transit residuals' in an exoplanet's rest frame is essentially considered as the exoplanet transmission spectrum (Pepe et al., 2002).

3.4 Analysis Methods

3.4.1 Analysis Methods for Objective 1

Interesting to analyse are the questions whether (i) all (adjusted) estimates for atmospheric water vapor column quantities are in the same order of magnitude and in an expected range, consistent with the climatological understanding of the study area; and/or (ii) whether the estimates of the different data sources vary significantly.

Vice Versa! Modelling atmospheric H_2O and O_2 trends from astrophysical observations

If the spectral positions and even the line depths of spectral lines caused by telluric absorption are known, and can be isolated, we can actually also model the behavior of the tellurics that we *see* in the astrophysical observations taken at the LBT. We reliably know the positions and depth of telluric lines thanks to the simulated telluric transmission spectra that were obtained from TAPAS for the night of the observation. This simulated transmission spectrum was modelled from the atmospheric estimates from the ECMWF analysis product and interpolated for the LOS of the telescope. And even though the quality of the data that TAPAS uses for its simulation, as well as the quality of the simulated transmission itself will be discussed in detail in the Section 5, TAPAS provides essentially a dependable atlas of lines to guide the eye for this next analysis step.

TAPAS indicates the molecular source of the absorption features. The user can therefore easily differentiate absorption lines caused by H_2O from those caused by O_2. We can expect that the change of absorption depth in O_2 lines will be proportional to the change of airmass in the LOS. The change of absorption depth of H_2O lines *might* follow the trend of the O_2 lines - if the amount and distribution of water vapor in the atmosphere remained stable over the entire observation time. But just as well, the behavior of an H_2O line might show a very different trend because of additional atmospheric dynamics.

Therefore, we model the progress of one single H_2O absorption line, as well as one O_2 absorption line. The relevant part of this result is not the absolute strength of the absorption line caused by either O_2/H_2O in a single observation, but the temporal progress of the line strengths over the course of the night, and the similarities or differences in the trends between H_2O and O_2 therein. The approach used to estimate the strengths the absorption lines is described in 3.4.2.

3.4.2 Analysis Methods for Objective 2

The analysis of Objective 2 is carried out in the regular stellar rest frame. The questions of interest are (i) whether there is a considerable amount of telluric lines left after the Correction by Splining, (ii) whether there is a notable difference in the removal success of telluric H_2O lines compared to telluric O_2 lines, and (iii) whether other influences can be observed, i.e. for

coinciding telluric and stellar absorption lines.

Comparing the Delta line depths

To answer these questions, we look at single spectra from different observations and how they have changed after the Telluric Correction by Splining. A single spectrum before the Spline Correction (the original Pepsi spectrum - S_{pepsi_i}) includes absorption lines form three set of features; for the same single spectrum after the Spline-correction S_{spl_i} most features are expected to be removed, apart from the exoplanet signal and uncorrelated noise. A Delta-Spectrum S_{Δ_i}, which shows the flux at each wavelength after S_{spl_i} was subtracted from S_{pepsi_i}, should essentially be identical to S_{pepsi_i}, because the exoplanet absorption features are again distributed over several wavelengths.

The line strengths of telluric (H_2O or O_2) absorption lines in S_{pepsi_i} and S_{Δ_i} should ideally be identical. The potential mismatches need to be studied carefully.

This again requires a robust knowledge of the positions and depths of telluric absorption lines. The simulated telluric transmission spectrum, that was obtained from TAPAS for three different observations (the First Observation at 02:17 am, the Middle Observation at 04:25 am and the Last Observation at 06:37 am), should ideally give us exactly this robust knowledge. At least the positions and depths of the O_2 molecules should be modelled with adequate precision, as TAPAS can calculate the airmass from the given observing angle (and therefore also the ratio of O_2 in such airmass, dependent on the temperature and pressure conditions in the LOS).

To ensure such a robust knowledge of the positions and perhaps even depths of the telluric absorption lines, this study makes alternating use of another simulated telluric transmission spectrum, provided by (Noll et al., 2012). This spectrum is incorporated into the correction pipeline of Molecfit (LINK SECTION) (Smette et al., 2015; Kausch et al., 2015). This spectrum was not simulated for the specific atmospheric conditions at the time or location of the observations of this study, instead it was produced for the annual mean atmospheric state above the Very Large Telescopes on Cerro Paranal, Chile (Noll et al., 2012). The general atmospheric conditions for Paranal and Mount Graham are somewhat comparable, at least for the observing season on Mount Graham, with considerably different atmospheric conditions during the monsoon summer months (Kerber et al., 2014; Carrasco et al., 2017; Turchi et al., 2018). Therefore, is is used only occasionally and in comparison with the TAPAS line atlas, which was included in the analysis of the thesis only at a later stage.

Equivalent Widths as Quantitative Comparison Means

A straightforward quantitative comparison of the strength of different spectral lines can be achieved by comparing the 'Equivalent Widths' of spectral lines. To estimate the 'Equivalent Width' of a spectral line, we calculate its 'area under the curve'. The flux at onset and offset of the curve is fixed for all investigated curves equally at 1.0. Representing this in a rectangle of the same geometric area, again with the predefined height of 1.0, leaves the width of the rectangle as
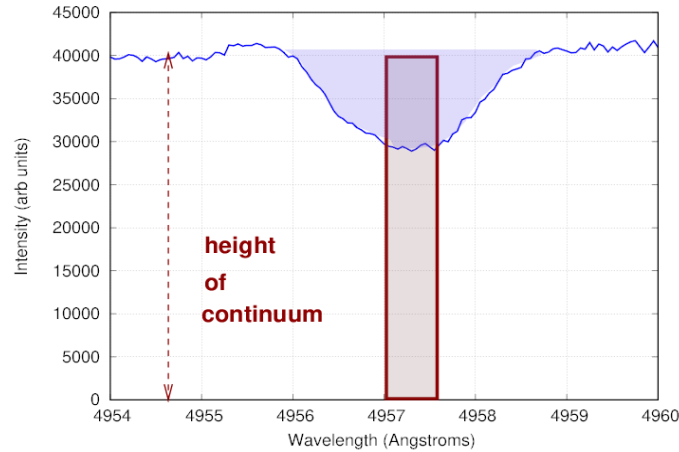
Figure 3.3: Concept of Equivalent Width. Image credits: Michael Richmond

discriminating parameter, reducing all other distinguishable parameters of the spectral lines to merely one dimension. This width is interpreted as equivalent to the strength of the spectral line (Stahler and Palla, 2004; Carroll and Ostlie, 2014). The basic concept can be seen in Figure 3.3 below (Image source: Michael Richmond) and can be described as follows:

$$W_\lambda = \int \frac{F_c - F_\sigma}{F_c} \, d\lambda \tag{3.3}$$

$$= \int \left(1 - \frac{F_\sigma}{F_c})\right) \, d\lambda, \tag{3.4}$$

$$\tag{3.5}$$

where F_c is the flux of the continuum, which is fixed at 1.0, and F_σ is the flux of the curve. This parameter is a common choice for spectral analysis in Astronomy (Stahler and Palla, 2004; Carroll and Ostlie, 2014), although it certainly offers a useful dimension reduction for other disciplines, as well as this thesis.

3.4.3 Analysis Methods for Objective 3

The analysis of Objective 3 is carried out in the already shifted exoplanet rest frame. The questions of interest for this Objective are (i) how well the exoplanet features have been preserved generally with the Telluric Correction Method by Univariate Smoothing Spline Interpolation, (ii) whether coinciding telluric, stellar and exoplanetary absorption lines impacted the success of the corrections, (iii) whether the origin of telluric line - H_2O or O_2 - had a notable effect on the condition of the exoplanet line, (iv) which Splining degrees were most effective, and (iv) whether different orbit velocity yielded different results.

Comparison to Artificial Exoplanet Spectrum

Analysed is how much of the artificial exoplanet transmission can be retrieved after the Spline Correction, comparing the purely artificial signal with the 'Average in-transit residuals'. The artificial signal serves as a benchmark for question (i); its strength is known, any variation from it after the Spline Correction can be quantified. The artificial spectral fingerprint included spectral absorption lines that were strategically placed at interesting wavelength locations, so that telluric (H_2O or O_2) features would be coinciding with exoplanet features, to answer questions (ii and iii). For Question (iv), the potential discrepancies among the three synthetic data sets will be analysed: the artificial transmission, that was incorporated at a Fast ('F'), Medium-Fast ('MF') and Slow ('S') radial velocity into the PEPSI observations. The radial velocity shifts simulated for the 'F' set is equivalent to the radial velocities that the exoplanet HD 189733b experiences. Sets 'MF' and 'S' have slower orbital velocities and thus undergo slightly weaker radial velocity changes during transit. This results at a smaller Doppler shift 'displacement' of the spectral features. In a time series of observations (in the stellar rest frame), these features appear at a narrower angle of the tilt towards the stellar/telluric features. The question (iv) whether this poses a limit to the performance of the Spline Correction is to be analysed.

Equivalent Width: Quantitative comparison of the exoplanet line strengths

As explained in the previous chapter 3.4.2, the 'Equivalent Width' (Carroll and Ostlie, 2014; Stahler and Palla, 2004) of a rectangle to the height of 1.0, equivalent to the area under this curve in the spectrum, is a useful tool of dimension reduction and quantitative comparison of the one remaining dimension - the equivalent width. In this step, the benchmark 'Equivalent Width' is measured for four example spectral lines of the artificial exoplanet spectrum, that are located on interesting parts of the spectrum: (i) an exoplanet feature coinciding with a stellar absorption feature, (ii) an exoplanet feature coinciding with a telluric absorption feature. These contexts are particularly interesting to identify potential constraints of the Telluric Correction Method. The same spectral ranges are re-investigated for their 'Equivalent Width' after the Spline Correction, measuring the strengths of the 'Average in-transit residual' signal to quantify exactly by how much the line strength has been reduced. As the Telluric Correction with a Univariate Smoothing Spline Interpolation was executed in three different degrees of Splining, the 'Equivalent Width' is calculated for the same spectral ranges after all three degrees of Splining. And since the Telluric Correction was implemented for three synthetic data sets, each including an artificial exoplanet transmission spectrum of different orbit velocity, the 'Equivalent Widths' of the compared spectral ranges are calculated for all three data sets. This comparison parameter would be interesting to investigate, as it can reveal other potential constraints of the Empirical Telluric Correction Method.

All processing and analysis steps described above were executed in Python with the following modules: *numpy, matplotlib, matplotlib.pyplot, astropy.io ascii, fits, astropy.table Table, Column, PyAstronomy pyasl, scipy.interpolate interpld, UnivariateSpline, astropy.modeling models, fitting,*

astropy.units, netCDF4 Dataset, datetime datetime, timedelta, cftime num2date, date2num, xarray, glob, shutil, copy deepcopy.

Chapter 4

Results

The following Section describes the Results of this study, and any data analysis that was performed to answer the research questions.

4.1   Results from the Atmospheric data collection

4.1.1   TAU Radiometer Results

The TAU radiometer values provided by the nearby Arizona Radio Sub-millimeter Observatory Telescope measured the atmospheric opacity at 225 GHz, corresponding to the opacity of both water vapor and (super-cooled) liquid water droplets or ices, present in clouds. The TAU data in Figure 4.1 a) gives an overview of the annual atmospheric opacity for 2021; the black regions indicate opacity values > 50% at 225 GHz, the deeper the white stripe, the lower the opacity at 225 GHz. 11 September 2021 marks the 254th Day of the year (DOY), indicated by the red line. The variations between seasons are large and saturated at > 50% in the summer months (June-September, DOY 150-250). The number of days with clearer conditions of < 30% opacity increase with the beginning of September 2021 (DOY 250). The highest number of days with opacity values of < 20% can be seen between January and February 2021 (DOY 50). c) is a cumulative graph showing that opacity values of < 20% were recorded for approximately 30% of measurements in 2020-2021. b) shows the enlarged TAU measurements for September 2021, where the values are given in 1/2 hour bins. In the night of DOY 253 and the early morning of 254, the atmospheric opacity is at 37-32%, the red line indicates the beginning of the observation at that LBT (AROT Sub-millimeter Telescope).

4.1.2   Indirect measurements

The following Figure 4.2 illustrates a Synthesis from all other available atmospheric data for the time of the observation. ERA5 provided continuous re-analysis data (blue line). Indicated with blue dots is the integration of the ERA5 TCWV values from a Vertical Column Density (VCD) to a Slant Column Density (SCD) - for the period of the observation (Sept 11, 02 - 06 am), this was calculated for a changing Zenith Angle; for the periods prior to or after the observation, this was
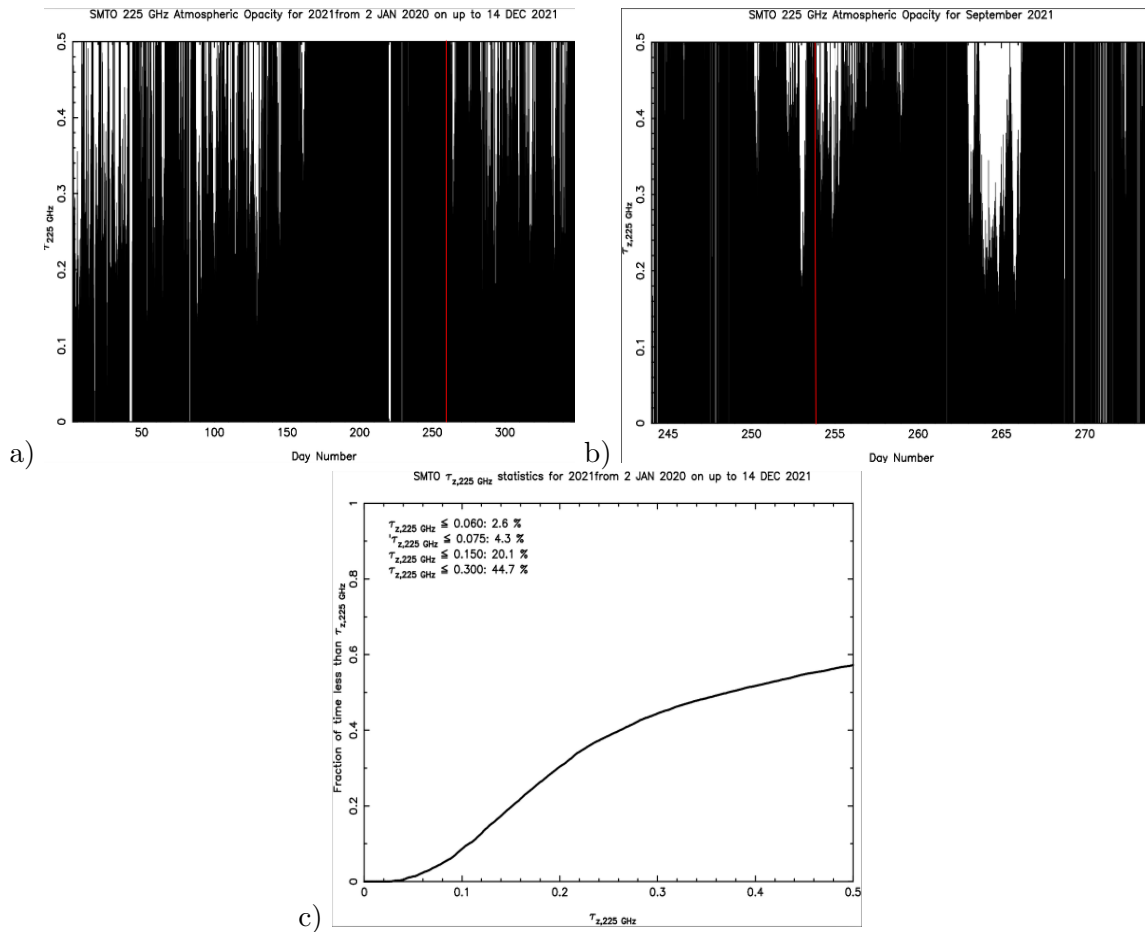
Figure 4.1: Shows the TAU radiometer measurements of atmospheric opacity at 225 GHz: (a) daily measurements for the year 2021; (b) daily measurements for September 2021; (c) the cumulative annual statistic for 2020-2021 (AROT Sub-millimeter Telescope).
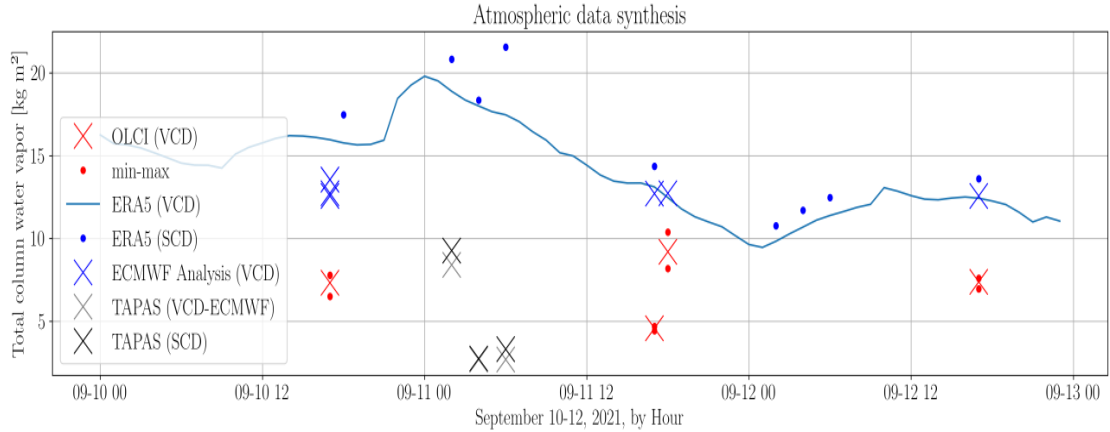
Figure 4.2: Result: Synthesis of available data on atmospheric water vapor above the LBT.

calculated for the mean Zenith Angle across all observations. The estimates provided by the ERA5 re-analysis and the ECMWF Analysis (alongside the OLCI Level-1 data) are in good agreement for Sept 11 and 12 (TCWV $\pm 0.5 \mathrm{kg\,m^2}$); for Sept 10, the discrepancy was larger with an ERA5 estimate of TCWV $+3.5 \mathrm{kg\,m^2}$. The discrepancy between the ECMWF estimates for the day times (17h, OLCI) and night times (02 - 06 am, TAPAS), respectively the discrepancy between the ECMWF interpolation provided to OLCI (corresponding to the OLCI pixel grid and average pixel altitude) versus the ECMWF interpolation provided to TAPAS and the exact location and altitude of the LBT was on average in the range of $\pm 7.75 \mathrm{kg\,m^2}$. The difference between the TAPAS values for a VCD and for a SCD was by $\pm 1.05 \mathrm{kg\,m^2}$, and larger for the last observations by 06 am, where the Zenith Angle was largest ($35.849°$), and smallest in the observations around 04 am, which were observed with the smallest Zenith Angle of $11.2497°$. The Vertical Column Densities given by OLCI were integrated from the mean pixel altitude to the true LBT altitude and were in the range of $7.21 \pm 2.324 \mathrm{km\,m^2}$, and generally in better agreement with the TAPAS TCWV values.

The following three Figures 4.3 show the simulated transmission spectra by TAPAS, which are based on the ECMWF Analysis values interpolated to the location, altitude and time from the original ECMWF Analysis window/grid. TAPAS then converted these values from the VCD over the observation geometry into a SCD for the requested molecular extinctions O_2 and H_2O and provided the simulations below. The TAPAS transmission denotes the molecular origin of the absorption lines, here shown for the same wavelength range as the PEPSI observations (530 - 630 nm). It illustrates that O_2 is the main contributor to telluric absorption at 625 - 630 nm (ca 35% atmospheric opacity) and contributes little to the transmission spectrum at 580 nm (ca 0.05% atmospheric opacity). H_2O contributes with absorption lines at several ranges, strongest at 590 - 600 nm (ca 25% atmospheric opacity), and shallower ($< 10\%$) at 540 - 550 nm, 570 - 580 nm, overlapping with the O_2 absorption lines at 625 - 630 nm. The simulated transmission for the First Observation at 02.17 am corresponds to a ECMWF Analysis TCWV value of $8.41608 \mathrm{kg\,m^2}$. Observed was at a Zenith Angle of $24.91648°$ with an airmass of 1.102300 in the line of sight. The transmission for the Middle Observation at 04.25 am corresponds to a TCWV of $2.69469 \mathrm{kg\,m^2}$, simulated for a Zenith Angle of $11.24974°$ and an airmass of 1.019533
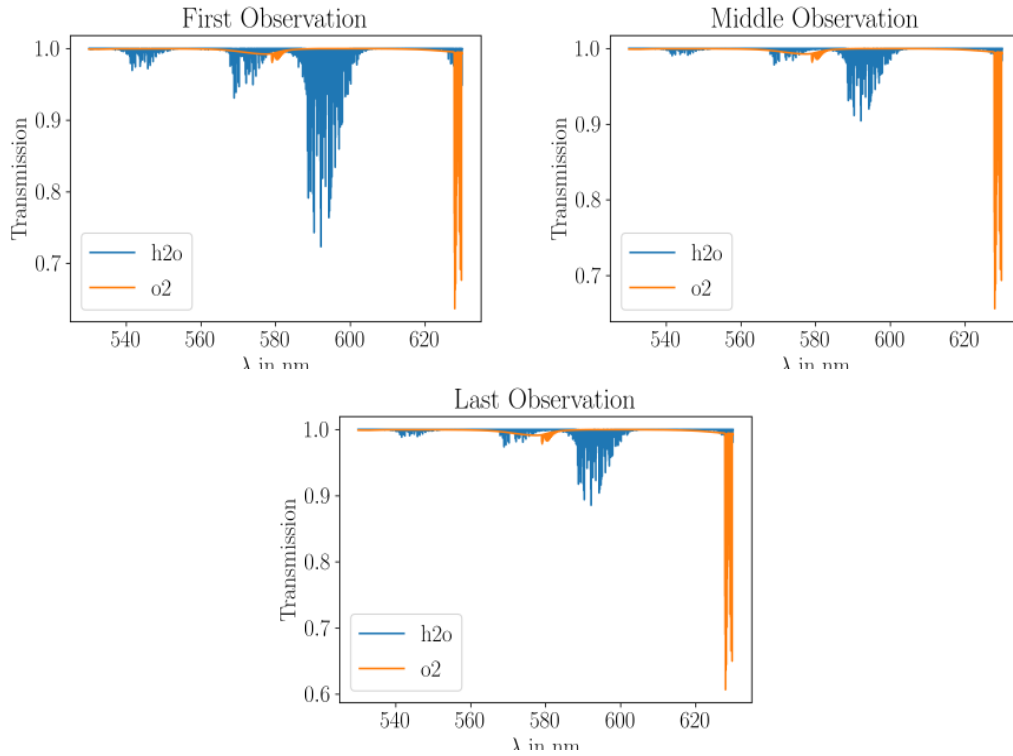
Figure 4.3: Result: Simulated TAPAS Transmission Spectra

in the LOS. The simulated absorption lines due to H_2O extinction are much shallower compared to the First simulated absorption lines. The transmission for the Last Observation at 06.37 am corresponds to a TCWV estimate of $2.69469\,\mathrm{kg\,m^2}$, simulated for a Zenith Angle of $35.84899°$ and an airmass of 1.232854. The H_2O absorption depth slightly increased again. The differences among the O_2 absorption lines between the three simulated transmission spectra are much fainter by comparison and not clearly visible here.

Context

The results of the visual examination of the day time observations of Mount Graham by the OLCI instrument can be seen in the Table below. The OLCI measurements of TCWV (bottom, black/white) were visualised the SNAP tool. Above are additional satellite images downloaded from EOSDIS Worldview, in this case originating from the Terra MODIS satellite. As these images in the visible wavelength range, they provide orientation for an easier interpretation of the OLCI images. What appears in the OLCI images as black areas are PWV saturated pixels. The darker greyscales indicate lower TCWV values, the lighter greyscales higher TCWV values. The OLCI measurement for Sept 10 was taken before the astrophysical observation, the measurements for Sept 11 and 12 after. The OLCI images of both Sept 10 and 11 show many dark saturated pixels. The EOSDIS Worldview images for these two days show the sky above Mount Graham covered in clouds. The OLCI image of Sept 12 shows no sign of saturated pixels, and the corresponding EOSDIS Worldview image is also cloud free.

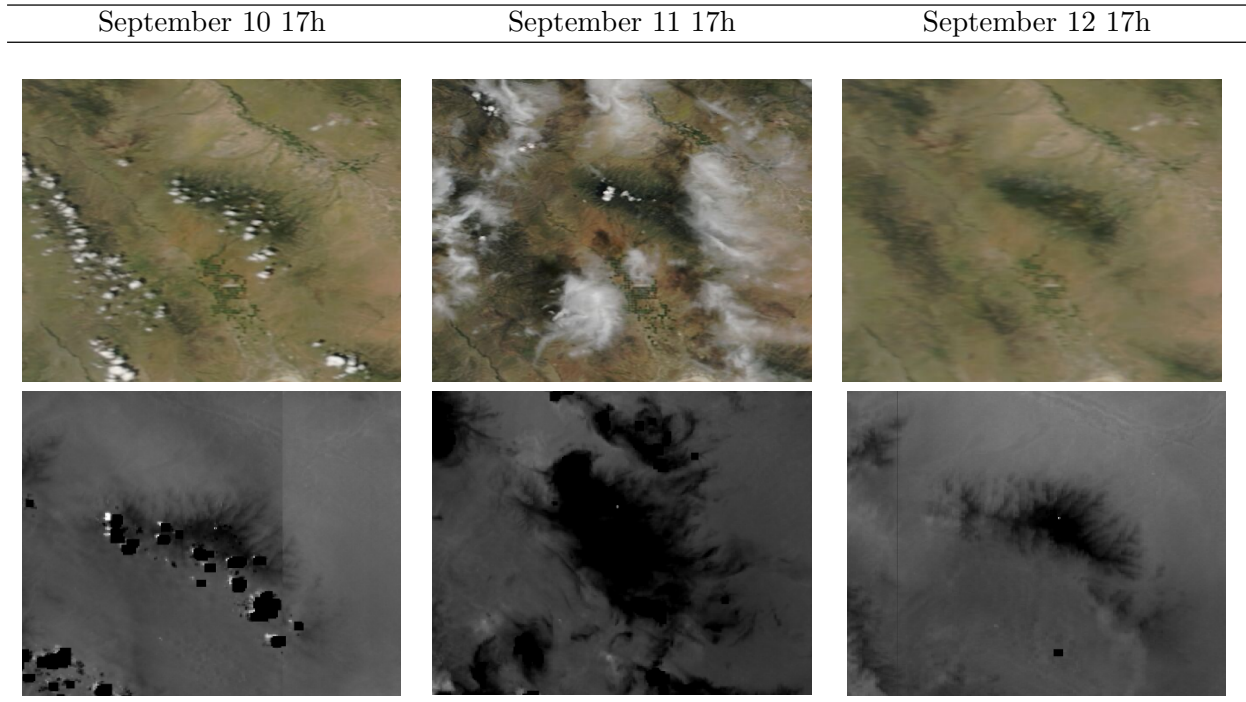| September 10 17h	September 11 17h	September 12 17h

Table 4.1: Cloud situation at daytime Mount Graham: (Top) Terra MODIS satellite imagery, obtained for 10 am from EOSDIS Worldview; (Bottom) Level-2 TCWV of Sentinel-3 OLCI, visualised in SNAP.

4.1.3 Modelled temporal progression of example lines from the PEPSI observations

In the Figure 4.4 below, the temporal progress of the depth of a single absorption line is modelled, specifically for a telluric O_2 line across all 59 observations. The depth of the line increases with a larger Equivalent Width - therefore, as illustrated in Figure 4.4 a), the line depth increases towards the end of the night. 4.4 b) shows the same line (from different observations) in the spectrum, as well as the simulated TAPAS lines.

In the next Figure 4.5 a), the temporal progress of the depth of a single H_2O line is modelled. The line depth decreases considerably between 02 am and 04 am (first half of the observations), and then increases again strongly over the second half. In the Figure 4.5 b) this behavior (slightly decreasing, strongly increasing depth) was illustrated by showing the same absorption line in the spectrum, with multiple observations overlapping: the first (02 am), middle (04 am) and last (06 am) observation. Shown in the same range are the simulated TAPAS absorption lines for the same observations. These, however, do show a slightly diverging trend: decreasing strongly towards 04 am, and then increasing only slightly towards 06 am.
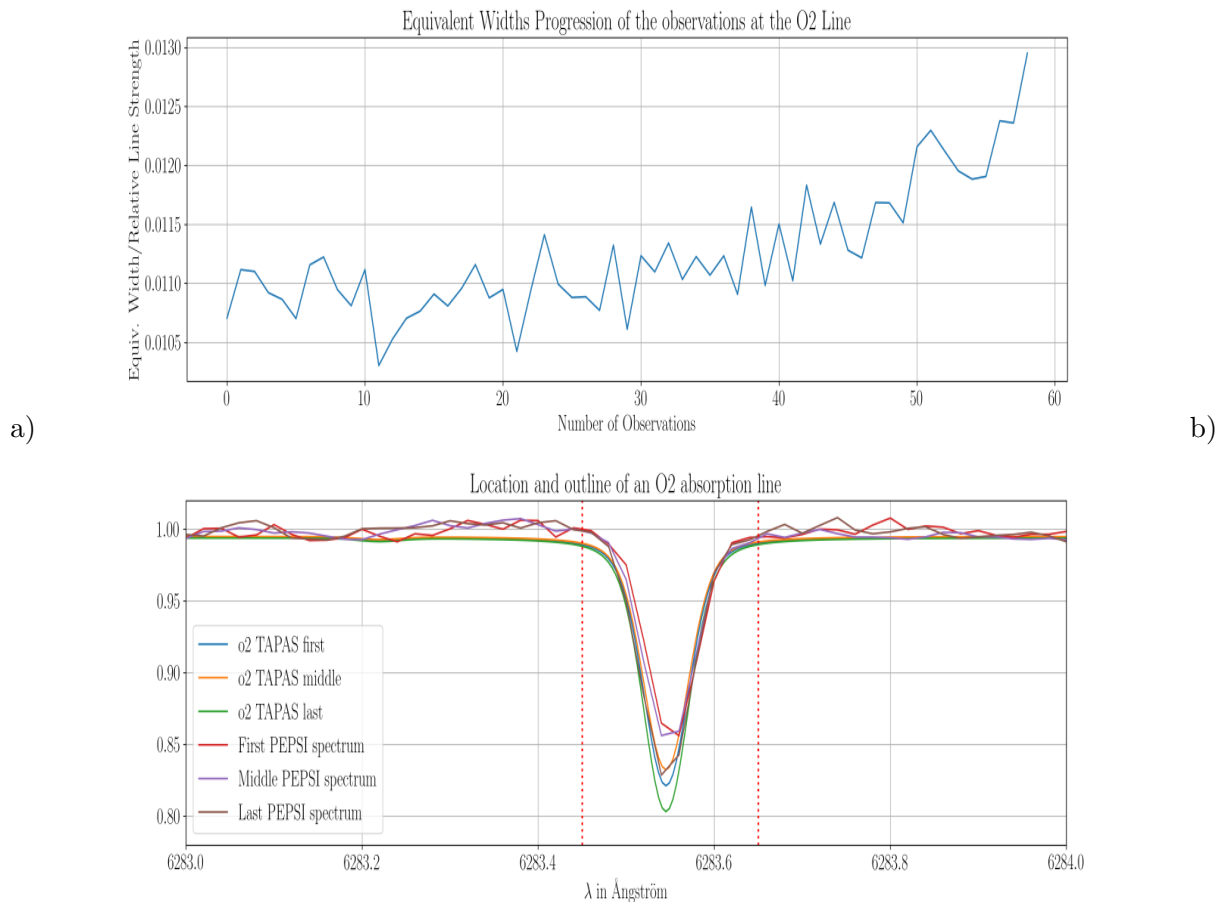
a)

Equivalent Widths Progression of the observations at the O2 Line

b)

Location and outline of an O2 absorption line

- o2 TAPAS first
- o2 TAPAS middle
- o2 TAPAS last
- First PEPSI spectrum
- Middle PEPSI spectrum
- Last PEPSI spectrum

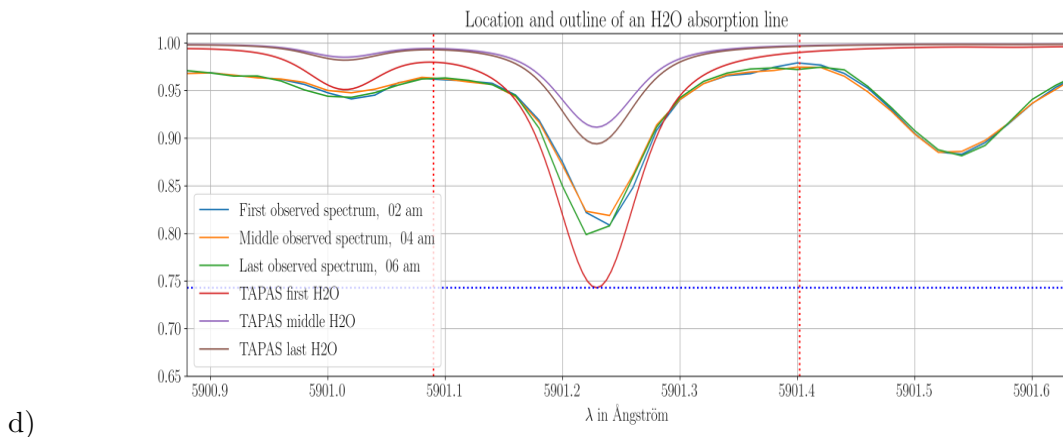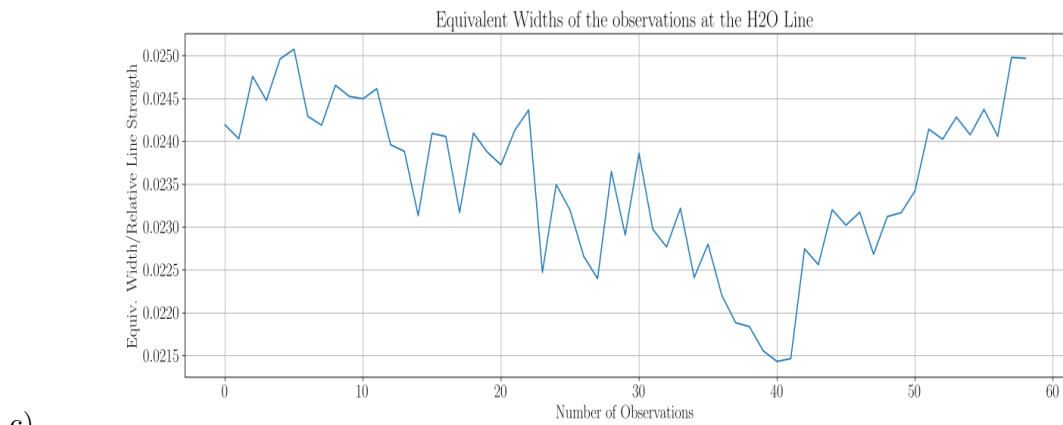Figure 4.4: Result: Temporal progress of an O_2 line

c)

d)

Figure 4.5: Result: Temporal progress of an H_2O line
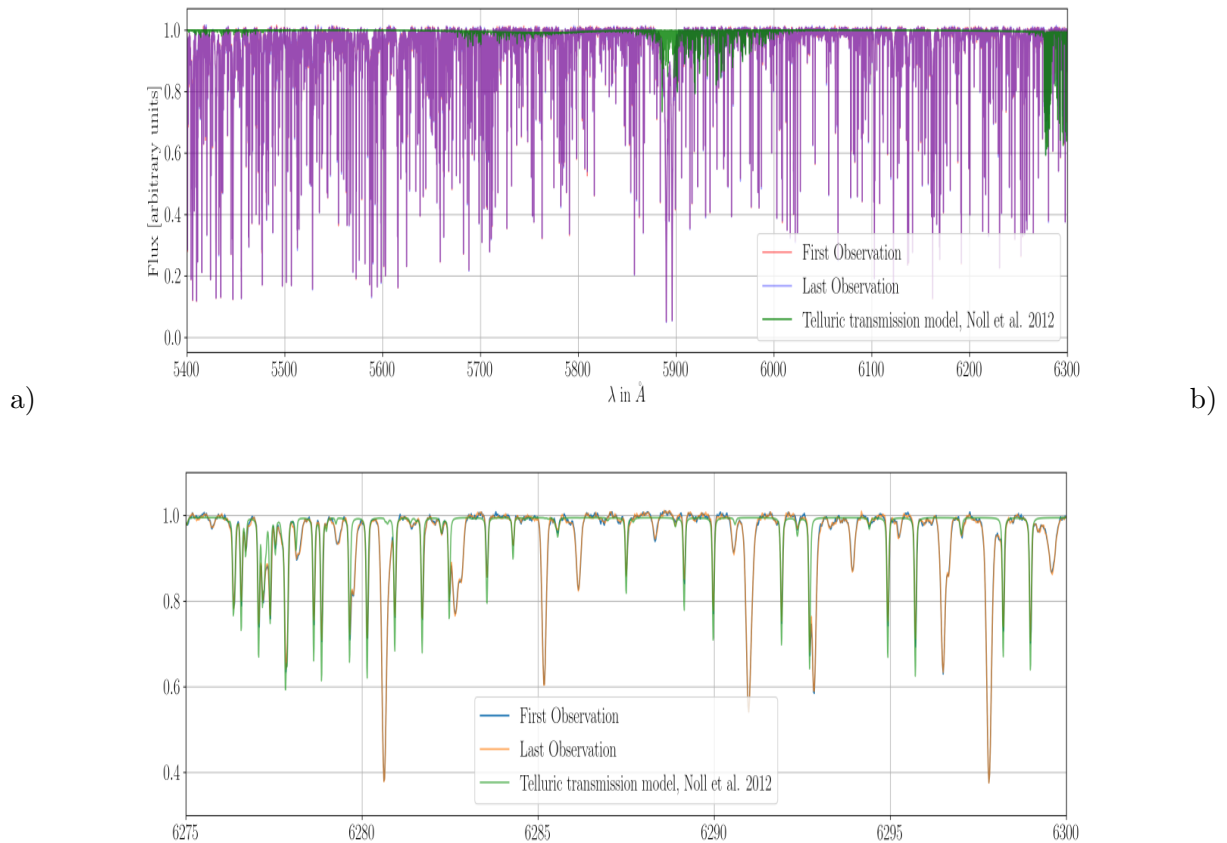
Figure 4.6: Result: First PEPSI 1D spectra

4.2 Results from the Telluric Correction

4.2.1 PEPSI processing results

Single observation

The top Figure 4.6 shows how a single PEPSI spectrum looks like. On the x axis is the full wavelength range covered during the observation, from 5300 to 6300 Ångström (or 530 - 630 nm) in high-resolution (R = 130,000); on the y axis is the relative flux in arbitrary units. This spectrum belongs to the First Observation at 02.17 am (red), overlapped with the Last Observation at 06.27 am (blue). Both spectra are virtually identical with only a few exceptions, e.g. at 5800 Ångström, where the red absorption lines of the First Observation are slightly deeper. Overlapped is also the simulated Telluric transmission model, taken from Noll et al. (2012) (green). It was included here to guide the eye again.

The Figure below looks more closely into a smaller wavelength range, towards the red end of the observed spectrum (6275 - 6300 Ångström). Again, only minor differences between the overlapping First and Last Observation are visible; the overlapping Telluric transmission model again shows which absorption lines in the observed spectrum can be attributed to Earth's atmosphere.
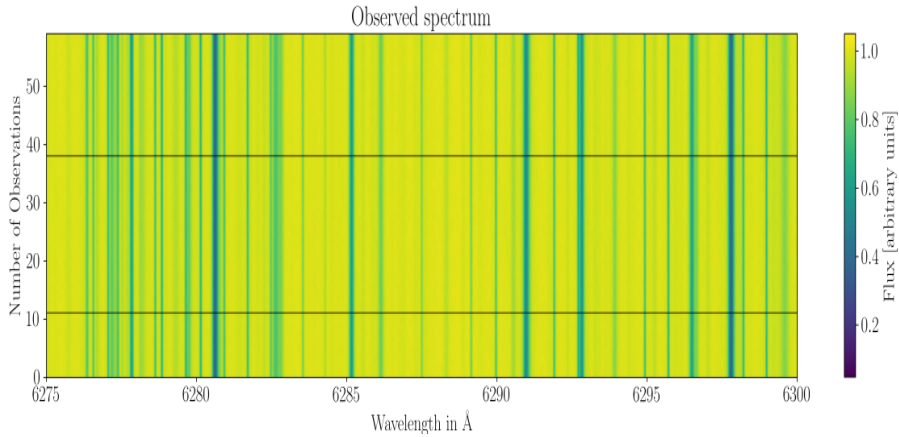
Figure 4.7: Result: PEPSI 2D spectrum

2D time series

Figure 4.7 shows the same small wavelength range as 4.6 b) above, but now as a time series of all obtained PEPSI spectra. It is a so called 2D spectrum, which is a common display in Astrophysical Observation. Each line on the y axis represents one observation; the flux information is now given by color, still in arbitrary units. A flux of 1.0 (yellow) indicates 100% of the maximum flux received at the CCD for that star across all observations. Any absorption is now visible as a darker shade. These absorption features appear as dark stripes stretching across all 59 locations, because the spectra are aligned in the stellar rest frame and calibrated so that they appear on the same wavelength.

The first 11 observations (under the indexed line) were taken before the transit occurred showing purely the light of the star. The top 21 observations (38 - 59, above the second indexed line) after the transit occurred, again showing purely the light of the star. The observations 12 - 38 (between both indexed lines) were the observations taken while the planet transited in front of its host star. In these observations, the absorption features of the star are distorted, and there is additional absorption caused by the atmosphere of the exoplanet. However, any of these changes of the stellar spectrum during the transit are too faint, too marginal relative to the overall flux received at the CCD, so that they cannot be distinguished in this display below.

2D mean-normalised spectra

Therefore, the observations were normalised. The 2D spectrum 4.8 now indicates the *normalised* flux as the variation of each pixel from the observed mean flux. In this display, three types of features are visible: **(i)** the previously visible absorption features now show trends and distinct changes of (relative) flux over the course of the 59 observations, e.g. a change from yellow (positive deviation from the mean flux) to dark blue (negative deviation from the mean). **(ii)** at 6280.5 Ångström, there is a spectral feature that does not show this trend; instead, the absorption line appears with two colors next to each other, sometimes yellow on the left and darker blue on the right (between the two indexed lines), and sometimes vice versa (e.g. in the first 11 observations under the lower indexed line). Also, **(iii)** new absorption features have
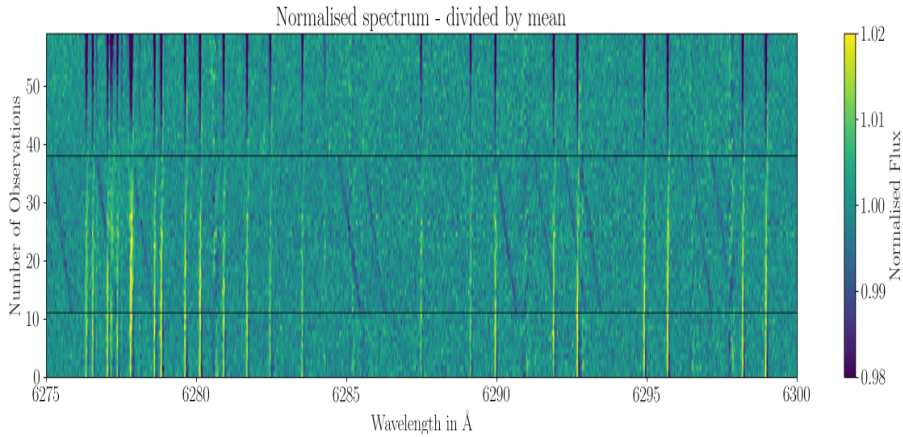
Figure 4.8: Result: 2D mean normalised spectrum

appeared on the observations taken during the transit. These appear tilted towards the other features.

(i) The tilted features belong to the exoplanet. As the 2D display is currently fixed in the stellar rest frame, they are Doppler shifted according to the radial velocity of their orbital phase.

(ii) The absorption lines that appear with the distinct trend from yellow to dark blue towards the end of the observation are telluric absorption features. They seem to experience a slight change of absorption depth over the course of the observations.

(iii) The absorption lines with yellow and dark blue edges, changing the sides, belong to the star. Most changes are visible especially during transit: the overall flux decreases slightly, and yellow/dark blue 'swap sides'. This s-shaped variation is a remnant of the 'Rossiter McLaughlin effect' (2.3.3), where the transiting planet covers parts of the blue shifted half, the stellar light appears more red shifted; as it covers parts of the red shifted half, the stellar light appears more blue shifted.

Time Series per Pixel: Pixel light curves

The Univariate Smoothing Spline Interpolation will later treat every pixel individually. Therefore, the Figures below illustrate the behavior of individual pixels in a time series. Figure 4.10 shows the light curve of a pixel on the (Stellar) Continuum, which is dominated by noise, with no distinct temporal trend visible.

The following Figures 4.11 illustrate the behavior of different pixels that are all located on a stellar absorption line. Depending on their location either on the flanks or in the center of the absorption line, they show a slightly different behavior over time. Especially the pixel located on the left flank of the absorption line (4.9) shows the 'Rossiter McLaughlin' effect again. Also the pixel on the right flank shows some behavior for the observations taken during transit (12 - 38); the central pixel doesn't.
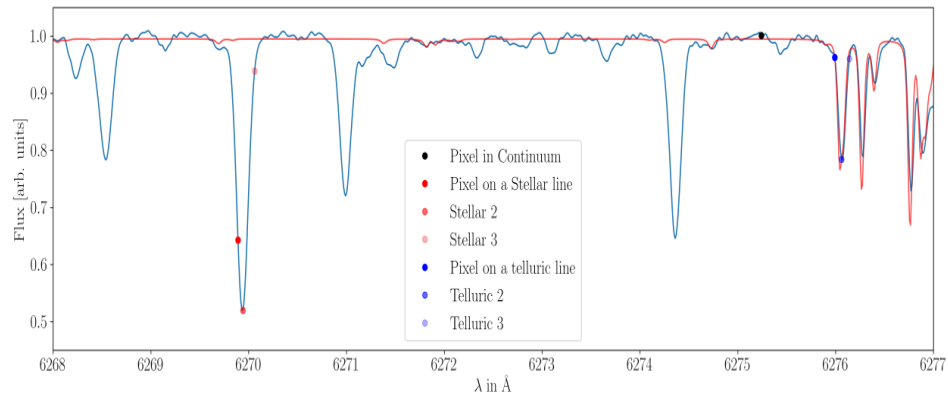
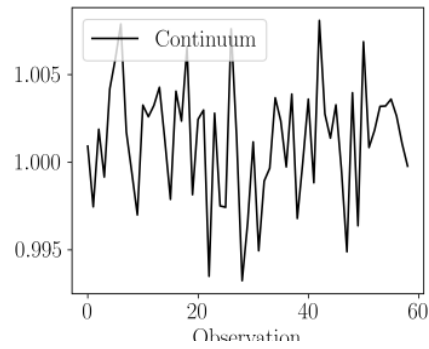Figure 4.9: Result: Location of the pixels described below.

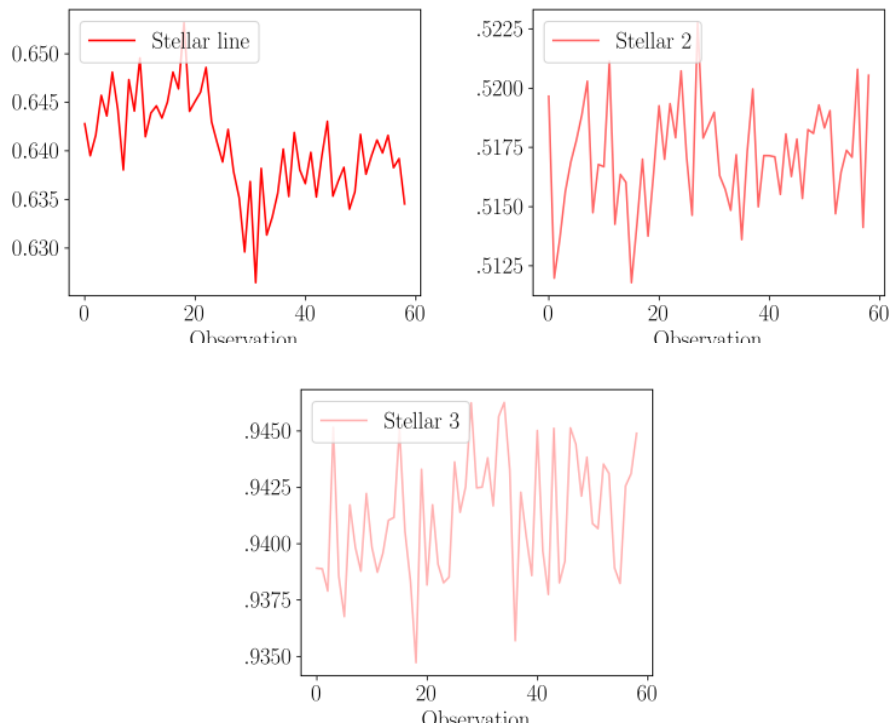Figure 4.10: Result: Continuum pixel light curve

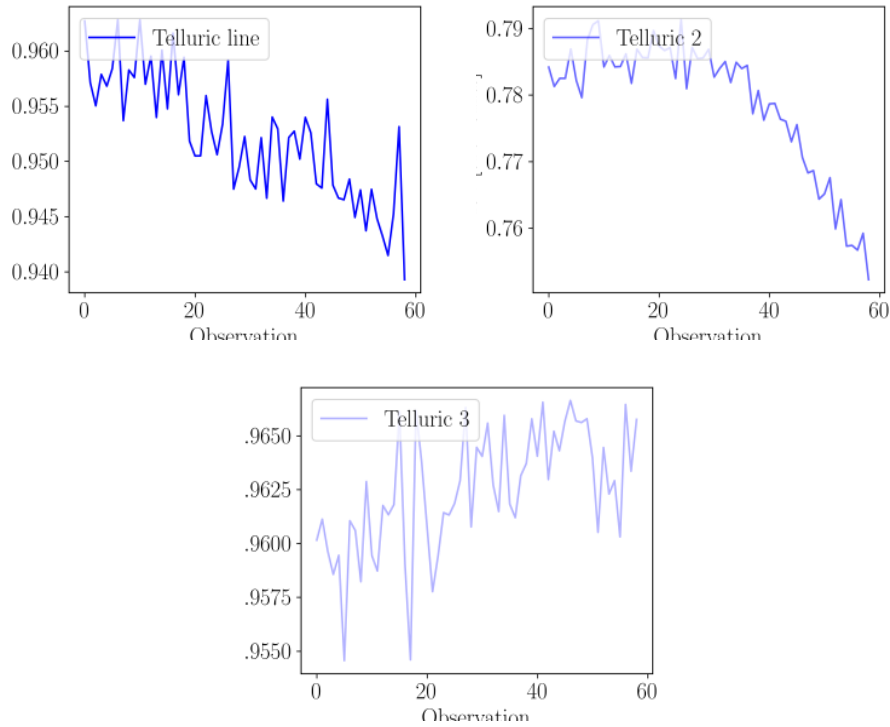Figure 4.11: Result: Stellar pixel light curves

54

Figure 4.12: Result: Telluric pixel light curve

Also, the behavior of pixels located on telluric absorption lines can show varying behaviors over time, depending on their exact location *on* the line, as can be seen in the Figures 4.12 below. While the exact behaviors and shapes of the temporal trends might differ among the Figures below, all three pixels show a distinct temporal trend.

4.2.2 Results from the Telluric Correction by Univariate Smoothing Spline Interpolation

Pixel light curves - Results from Spline Correction

The Figures 4.13 below show how the Univariate Smoothing Spline Interpolation worked on individual pixels. In the left Figure we see how the interpolated Spline Curve is fitted to the pixel values of one of the Stellar absorption lines from above. This pixel was located on the left flank of the absorption line. We see three Spline Curves corresponding to three different Spline degrees: quadratic, cubic and quartic. The Spline by quadratic degree only picked up on the general reduction of flux for that pixel over time, whereas the Splines by cubic and quartic degree fitted more closely to the sinus-shape of the light curve; the cubic spline is also the closest fit at both end points of the interpolated curves, while the Splines of quadratic and quartic degree interpolated further away from the first and last data point on the curve, rather continuing their detected trends.

The Figure on the right shows how the result looked like after each data point on the curve was normalised by division through the Spline Interpolation of its light curve. Again, shown are the results for three degrees of Spline, with the cubic and quartic Spline Corrections in lighter shades of red. The corrected light curves still show the same noise behavior as before - corrected was
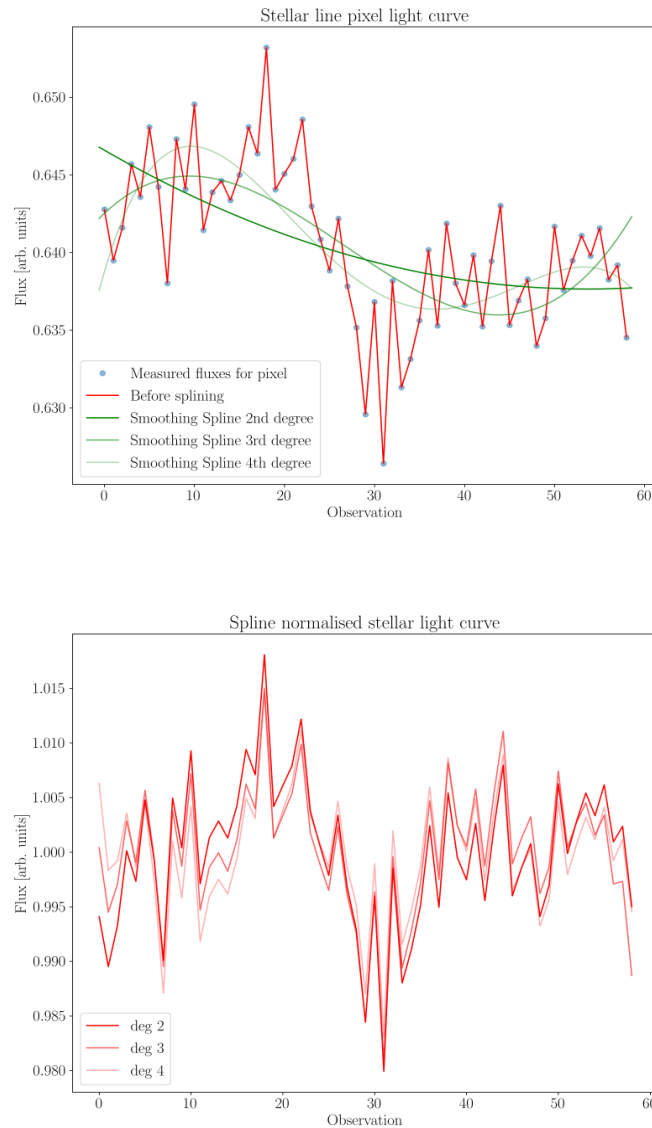
Figure 4.13: Result: Splines for stellar line

only for the general trend. While the light curve corrected by quadratic Spline still looks very similar to the curve before the Correction, the two other Spline degrees smoothed the overall signal slightly. Any behavior of the stellar pixel during transit, what I have flagged as 'Rossiter McLaughlin effect' before, remained undisturbed in all three Spline Corrections.

These results can also be shown for one of the pixels located on a Telluric absorption line in Figures 4.14 below. The left Figure shows how loosely or closely the three Spline degrees interpolated to the data points: the differences among the interpolate curves are less clear than for the Stellar line; most differences are visible towards the fits around the end points. In the right Figure we can see the results and how the Corrected pixel light curves look like after each pixel was divided through the Spline of its light curve. Here again, the Spline degrees used in the Normalisation are indicated by the shade of blue. Most differences in the results are also
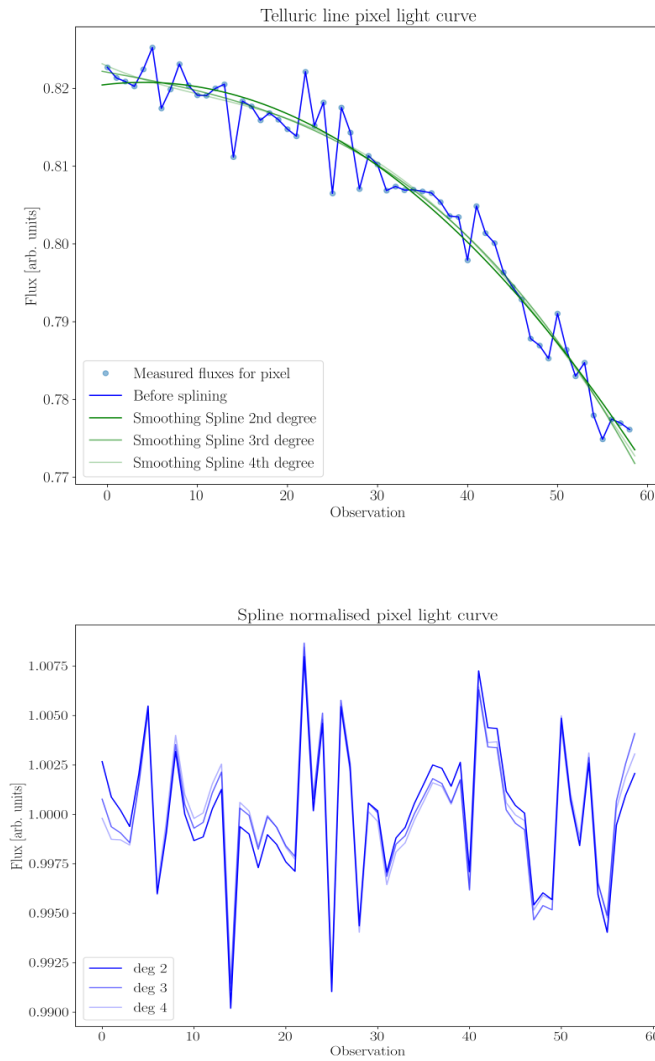
Figure 4.14: Result: Splines for telluric line

only visible towards the beginning/end of the curves.

2D spectra - Results from Spline Correction

The other pixels were treated in exactly the same manner: a Univariate Smoothing Spline Interpolation fitted to each pixel light curve, and each individual pixel divided by its Spline Curve. The result of this Correction is presented again in a 2D spectrum. The Figures 4.15 below show the Mean-normalised uncorrected 2D spectrum for orientation and comparison (top), and the same spectrum corrected by Quadratic Spline (bottom), in the wavelength range of 6260 - 6285 Ångström. Just like in our previous example, the absorption features in the right side of the Mean-normalised spectrum are mostly telluric absorption features with a clear temporal trend (decrease - dark blue; and increase - yellow) over the observation night. The three spectral features in the left side are stellar features, which show the Doppler distortion during the transit ('Rossiter McLaughlin effect'); and the tilted features at 6275 - 6280 Ångström are absorption features from the exoplanet's atmosphere. In the bottom Figure, the telluric features are not
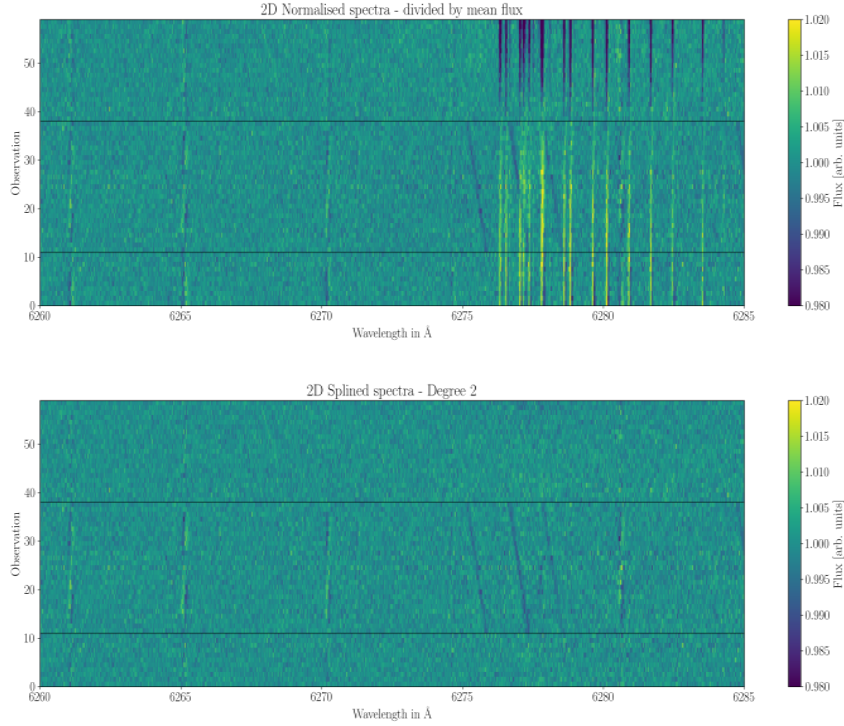
57

Figure 4.15: Result: Mean-normalised 2D spectrum (top) and quadratic Spline normalised 2D results

visible anymore, while the exoplanet's features remain. The stellar features have mostly been removed, except for their absorption behavior during the 'in-transit' observations.

As for the example pixel light curves above, the Spline Correction for all pixels was also done with three different degrees of Spline. The Figures 4.16 below show the Corrected 2D spectra after a cubic (top) and quartic (bottom) Univariate Smoothing Spline Interpolation were applied. The differences among the three Spline Corrections are again too faint to be picked up by eye, in the Splined results with cubic and quartic degree, the remaining stellar features are fainter than for the quadratic Spline result.

Obsolete results

Keles et al. (2022) suggests another preceding processing step, where all spectra are divided by the out-of-transit spectra first, and the Correction by Univariate Smoothing Spline Interpolation is performed afterwards. This did not change the quality of the results. Another attempt was to exclude all in-transit pixels from the Splining process, so that any behavior the pixels might show there would not affect the overall trend of the Spline. This however yielded weaker correction results, as the Spline did not have enough data for the in-transit pixels to go on, and had to divide these pixels through a poorer fit. Also, higher-order Splines beyond the quartic degree were applied, but these did not improve the results.

At an earlier stage of this thesis, the performance of the Telluric Correction by Univariate Smoothing Spline Interpolation was planned to be compared to the performance of a Telluric
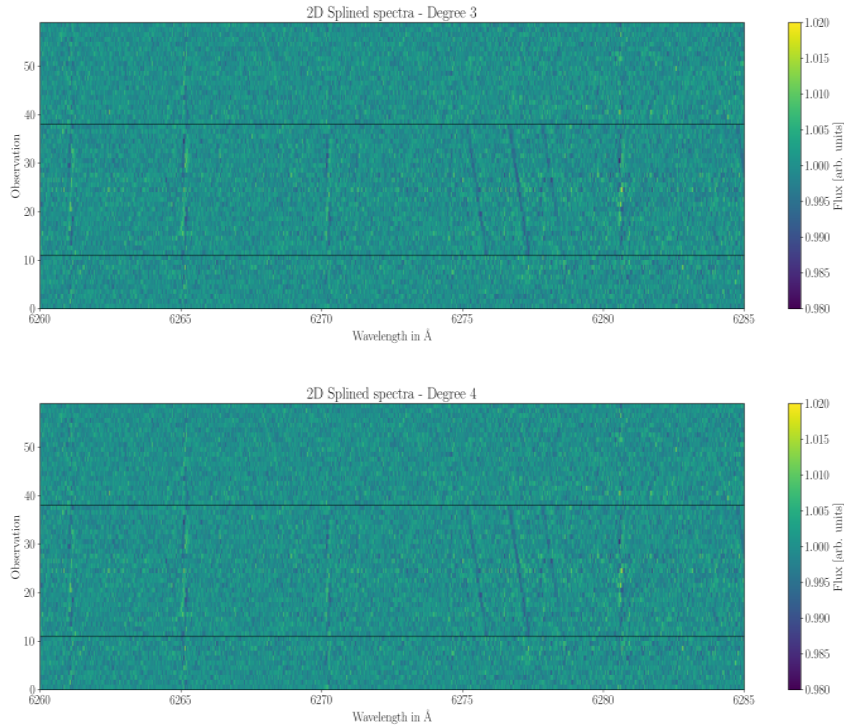
Figure 4.16: Result: 2D Spline normalised by cubic Spline (top) and quartic Spline (bottom)

Correction with 'Molecfit' (Smette et al., 2015; Kausch et al., 2015). 'Molecfit' is a model-based method, incorporated into the standard correction pipeline for ESO Telescopes (European Southern Observatory) and considered state-of-the-art. However, the corrected spectra were still flawed, for several reasons, as described below. This comparison case was therefore abandoned.

If applied correctly, the Molecfit output product is a telluric-free version of the original single spectrum. Molecfit requires several data inputs: (i) any single observed spectrum, (ii) a parameter file that includes the geographic location, altitude, the instrument resolution and the observing angle, and (iii) atmospheric data for the time of the observation. The atmospheric data is taken in this case from the GDAS archive (Global Data Assimilation System), basically the equivalent to the ECMWF analysis archive, provided by NOAA (Smette et al., 2015; Kausch et al., 2015). The first processing step is performed for a small wavelength range. This range is indicated by the user. It contains only a single absorption line of known telluric origin, and known molecular source; the indicated range should not include stellar absorption features, or features of unknown origin. For this indexed range, Molecfit simulates a single absorption line for the respective atmospheric constituent. The simulation is based on the atmospheric values obtained from GDAS and the corresponding airmass in the observing angle, and a LBLRTM. The line depths of the simulated absorption and the observed absorption (in the given wavelength range) are fitted to each other. The best fit of this process - ultimately the best fitting atmospheric parameter for this constituent - is then fed back to Molecfit, and used in the second processing step for the full transmission spectrum. This is calculated for all atmospheric constituents that were indicated in their single absorption lines by the user. This transmission is removed from the observed spectrum. The user receives this corrected output spectrum as well as the intermediate simulated

transmission spectrum, and the atmospheric parameters that this transmission spectrum was simulated for (Smette et al., 2015; Kausch et al., 2015). Specifically the simulated telluric transmission spectrum as standard product from this Correction would have been useful to my study. Fortunately, the TAPAS service offers a similar product.

However handy the output, the Molecfit tool expects the data input in a very specific way. This limits its applicability. From the technical side, it is tailored to produce telluric corrections for spectra obtained at ESO telescopes. The tool therefore expects the input spectra in the same data format and style. This limit can be, and was adjusted for. The second limit was encountered with the first processing step: the selection of a number of narrow wavelength ranges with only single telluric absorption lines, without containing other absorption features. Ideally, this absorption line is isolated, surrounded by continuum flux, so that the absorption depth of the indicated telluric line can be estimated by its relative flux against the continuum at this wavelength. Depending on the quality of the spectrum, the spectral resolution, or the type of star, this can be challenging: while hotter stars contain typically very few absorption lines, cooler stars, such as K and M type stars contain many in their spectrum. The host star HD 189733 from this study is such a K type dwarf, therefore the spectrum shows only few wavelength ranges with solely a continuum absorption, maybe even a telluric line. This limits the applicability of the Molecfit tool to certain stellar types, respectively reduces the quality of the fitted correction for others (Smette et al., 2015; Kausch et al., 2015; Langeveld et al., 2021; Sedaghati et al., 2021).

4.2.3 Delta Analysis - How much was removed?

The following Section reviews the success of the Correction to remove Telluric transmission features from the observations. The Figures below therefore show several Delta-Spectra S_{Δ_i}. These are calculated as the flux at each wavelength after the Spline-corrected S_{spl_i} was subtracted from the original observation S_{pepsi_i}. The ideal S_{Δ_i} would be virtually identical to S_{pepsi_i}, because S_{spl_i} should only include the exoplanet's features. For orientation, the Figure also shows the simulated TAPAS transmission spectrum, and the artificial exoplanet signal to identify spectral regions where indeed discrepancies between S_{pepsi_i} and S_{spl_i} should or should not be present.

The Figure 4.17 below shows the spectral range of 5920 - 5930 Ångström. In this example, we look at the First Observation's PEPSI spectrum and Delta spectrum (top) and the Last Observation's PEPSI and Delta spectrum (bottom). In the **First Observation**, the Delta lines (green) are deeper than the PEPSI lines (orange), when the absorption is caused by telluric (H_2O, blue). In the four - likely stellar - absorption lines without telluric (H_2O), the PEPSI line is slightly deeper than the Delta line. The most distinct non-telluric absorption line in this range is at 5924 Ångström. The simulated TAPAS lines are also much deeper than the actual PEPSI observation and hint towards a mismatch between simulation and observation. In this, and in the Last Observation, the Artificial Exoplanet line is flat, meaning that this range does not include an artificial exoplanet signal contributing to any discrepancies between S_{Δ_i} and S_{pepsi_i}. In the **Last Observation**, where the simulated TAPAS lines are much shallower than the actual PEPSI observation, also the Delta lines are slightly shallower than the PEPSI lines.

The line strengths of the S_{Δ_i} and S_{pepsi_i} spectra were compared quantitatively, as well. This
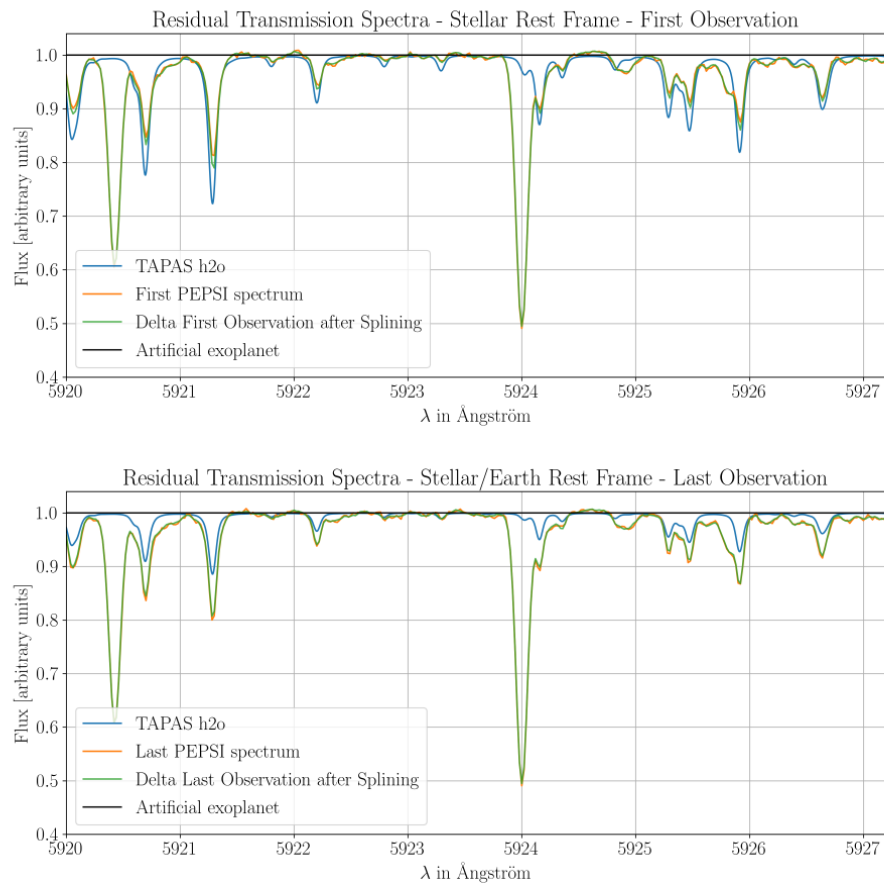
Figure 4.17: Result: Delta Analysis, for First Observation (top) and Last Observation (bottom)

comparison was done for two exemplary lines, dominated by telluric H_2O or O_2 absorption each. The Figures 4.18 below again include the simulated TAPAS transmission line for this range and one PEPSI observation, which is in both cases the Middle Observation at 04.25 am. The Equivalent Widths were calculated for the original line strength of the PEPSI spectrum, as well as for three Deltas, calculated after the three degrees of Spline Correction. The spectral ranges of both the H_2O line (5900 - 5902 Ångström)(top) and the O_2 line (6283 - 6284 Ångström)(bottom) were chosen before, when calculating the progression of their line strengths over time, presented in the Figures 4.5 and 4.4 above.

The results for the Delta-Equivalent Width comparisons, in both cases, show no difference among the Spline degrees. For the First Observation at 02.17 am, where the Equivalent Width of the O_2 line was by 0.01071, the Delta's line was by 0.00036 stronger; for the Middle Observation at 04.25 am, the original observation had a line strength of an Equivalent Width of 0.01123 (increasing in strength), with an almost identical Equivalent Width of the Delta line of 0.01107; in the last Observation at 06.37 am, the Equivalent Width of the O_2 line was calculated at 0.01295, and for the Delta line at 0.01295, which was slightly shallower. The Equivalent Widths of the H_2O line was measured for the First Observation with 0.02419, the Delta's strength with an Equivalent Width of 0.0256 by 0.0014 stronger and deeper; the difference between the Equivalent Widths for the Middle Observation were in the same order of magnitude, but inverted, with the Delta's line (0.2273) by 0.0012 shallower than the original PEPSI line (0.02386); in the Last Observation, the Equivalent Width for the PEPSI line was 0.02497 - stronger than in the First Observation, which was also closely met by the Delta H_2O line's Equivalent Width of 0.02416.

4.3 3. Obj-Results

4.3.1 Shifting to exoplanet rest frame

The analysis of Objective 3 is carried out in the exoplanet rest frame, which requires a shift. The results of the shift of rest frames is demonstrated in the following Figures 4.19. The top Figure shows the Spline-Corrected 2D spectrum in an exemplary wavelength range of 6275 - 6285 Ångström in the original stellar rest frame. The tilted features are the exoplanet features, the perpendicular feature in the center of the Figure, at 6281 Ångström, is a stellar feature. The middle Figure shows the same wavelength range, now in the exoplanet rest frame. Each row (each observation) has been shifted by a different radial velocity, corresponding to the negative of the radial velocity of the exoplanet at this part of its orbital phase. The exoplanet's spectral features thus appear aligned. The bottom Figure shows how this shift looked like in an individual spectrum and at this spectral position. At this spectral range, the radial velocity of $-29.8367\,\mathrm{km\,s^{-1}}$ causes a Doppler shift of -0.6 Ångström.

4.3.2 Analysis of the Results

With all spectra shifted to the exoplanet rest frame, we can now review the success of the Correction to preserve exoplanet transmission features in the observations. Therefore, below Figures 4.20 show a comparison of the strength of the exoplanet signal before the Spline Correction with
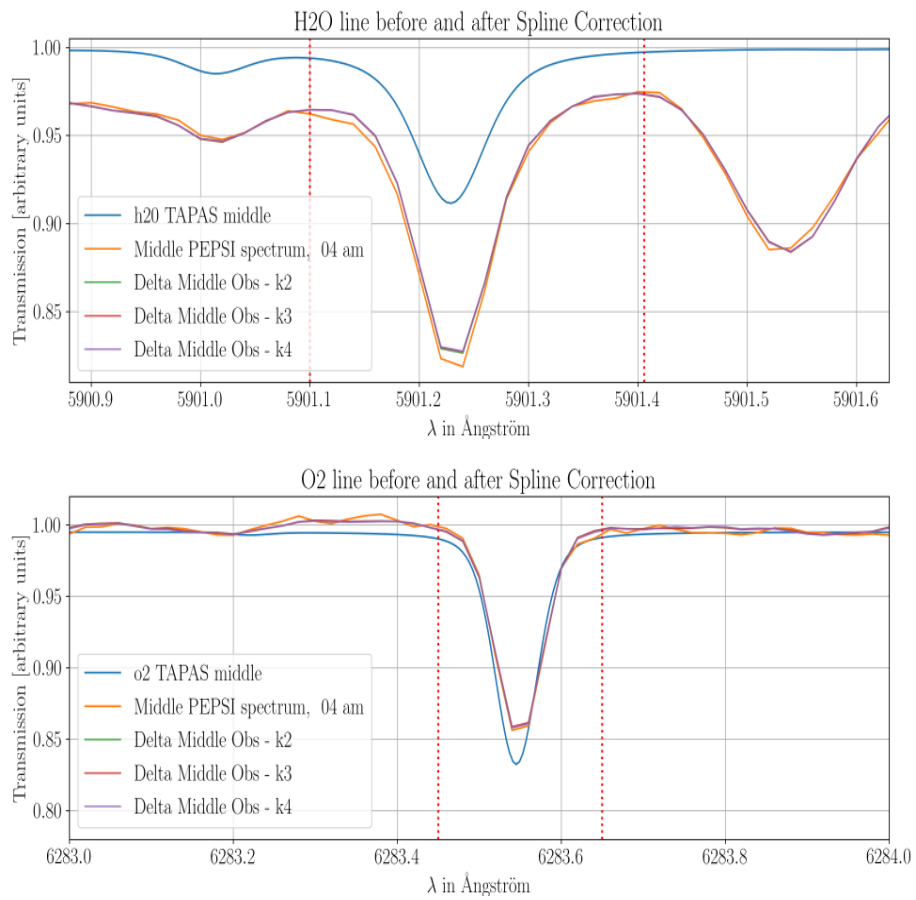
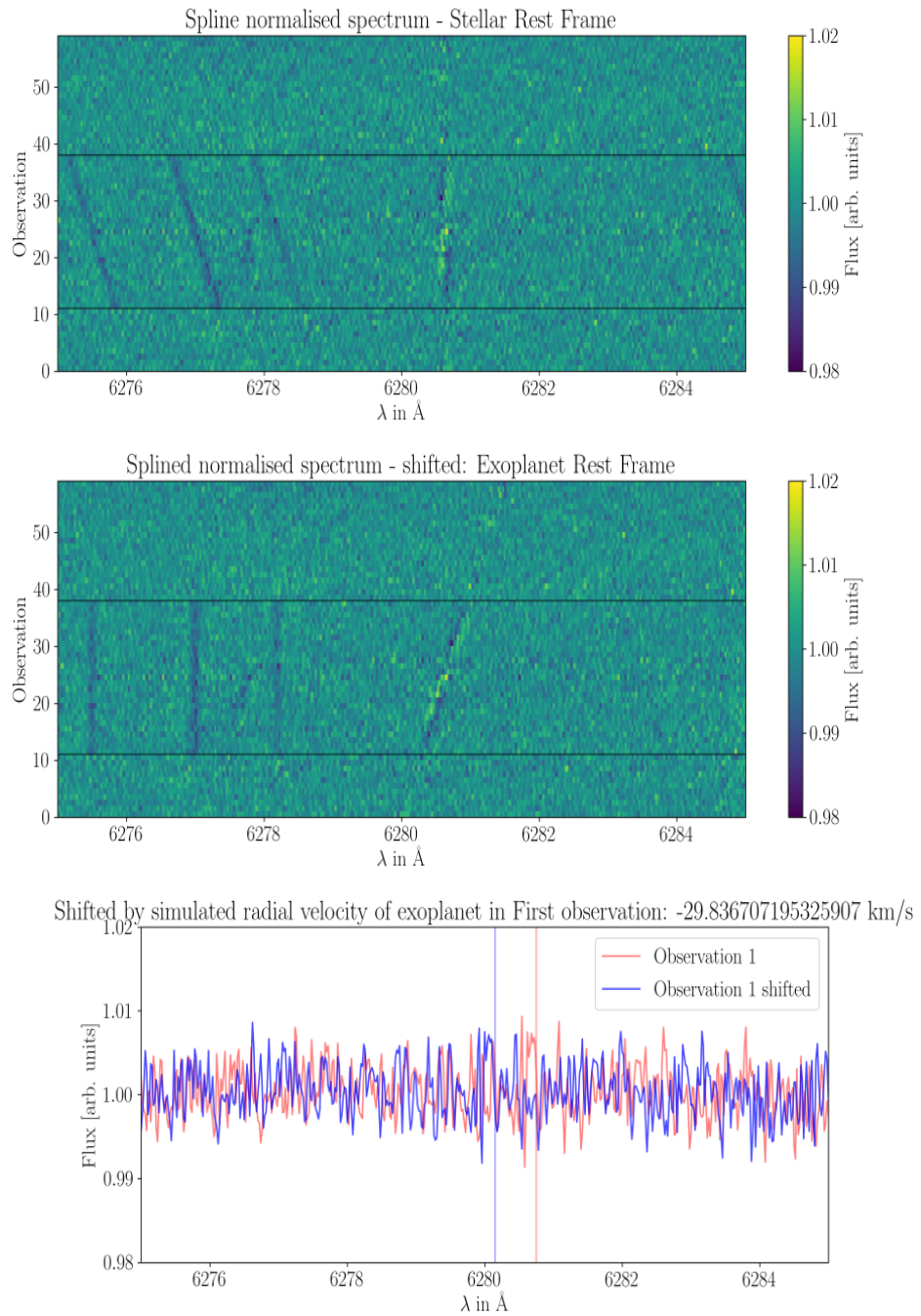Figure 4.18: Result: Equivalent Widths of the Deltas. H_2O line (Top), O_2 line (Bottom)

Figure 4.19: Result: Shifting rest frames

the Artificial Signal; the signal after the Correction is given by the 'Average in-transit residual'. This was calculated for the three different degrees of Spline Interpolation. For orientation, the Figure includes also the simulated transmission model (Noll et al., 2012) for orientation. The Figure 4.20 (top) in the exemplary wavelength range below (5395-5405 Ångström) shows one artificial exoplanet absorption feature at 5398 Ångström. The 'Average in-transit residuals' of all three Spline degrees reflect that feature, albeit not at the true depth of the simulated signal; the depth of the 'average in-transit residuals' is roughly 0.2 % shallower. The differences among the different Spline degrees are in the orders of ±0.0005 (arbitrary) units of relative flux. The exoplanet signal is not coinciding with a telluric absorption line, but there are multiple telluric features immediately adjacent.

Apart from these differences, Figure 4.20 (top) reveals a noteworthy feature at 5397 Ångström: a sinus-shaped curve with no apparent origin. Figure 4.20 (bottom) was therefore shown for additional orientation. We can see a Mean-normalised 2D spectrum in the stellar rest frame in the same wavelength range as the top Figure. The curve at 5379 Ångström (top) is aligned with a strong stellar absorption line, showing a distinct 'Rossiter McLaughlin effect' (bottom). As the 'Average in-transit residuals' are calculated from the Exoplanet rest frame, any stellar features will have been tilted - any signal that is not resulting from noise will be attributed to the 'in-transit' average of a different pixel. The same shape, albeit less prominent, can be seen at 5404 Ångström (top Figure), where also a strong stellar absorption line with a clear 'Rossiter McLaughlin effect' is visible in the bottom 2D spectrum.

Below Figure 4.21 shows one example range at 5802 - 5803 Ångström, where one very shallow artificial exoplanet absorption line was hidden in the observations (5803.4 Ångström). This Figure illustrates an example, where not only the true depth of the exoplanet was not fully met, but where the 'Average in-transit residuals' - regardless of Spline degree - don't replicate the absorption line at all. At least, this faint features seems to be buried under the remaining noise, which is equally as strong as the maybe accidental, maybe intentional curve at this location.

Quantitative Comparison by Equivalent Widths

Again, the line strengths were quantitatively compared by their respective Equivalent Width. This was done for two exemplary lines, that present different contexts. The results are presented in the Table 4.3.2 below. This Table comprises a matrix with the Equivalent Widths of the residuals (that would scientifically, ideally, be interpreted as the exoplanet transmission spectrum) and (i) how the different contexts influenced the performance of the Spline Correction, but also (ii) which Spline degree performed best. The matrix also shows the third comparison-case of interest: whether or not a slower orbital velocity would affect the performance of the Spline Correction. The Figures below all show the 'Average in-transit residuals' for the synthetic spectrum that included the artificial exoplanet with the 'Fast' orbital velocity. This is the velocity analogue to the observed exoplanet HD 189733b.

The contexts of the examples can be seen in the Figures 4.22 below: Figure 4.22 a) shows one artificial exoplanet line at 6278.5 Ångström, which is coinciding with a telluric O_2 absorption line, indicated with the simulated TAPAS transmission. Figure 4.22 b) shows an exoplanet absorption
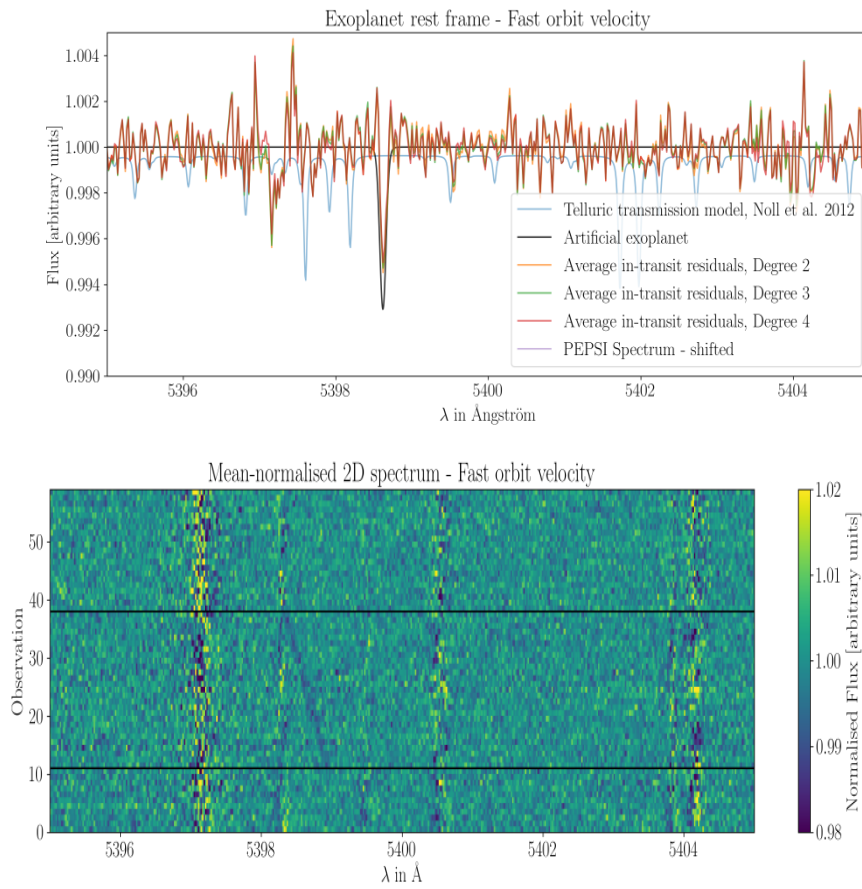
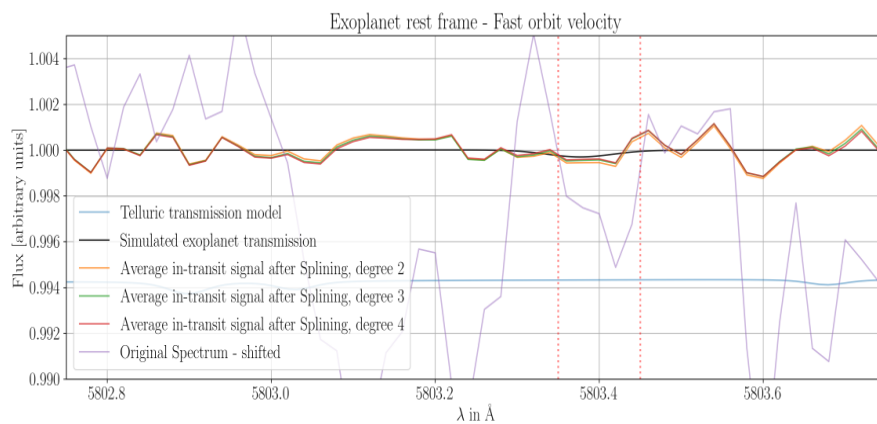Figure 4.20: Result: Average in transit residuals Analysis (Top), and Mean-normalised 2D spectrum (bottom).

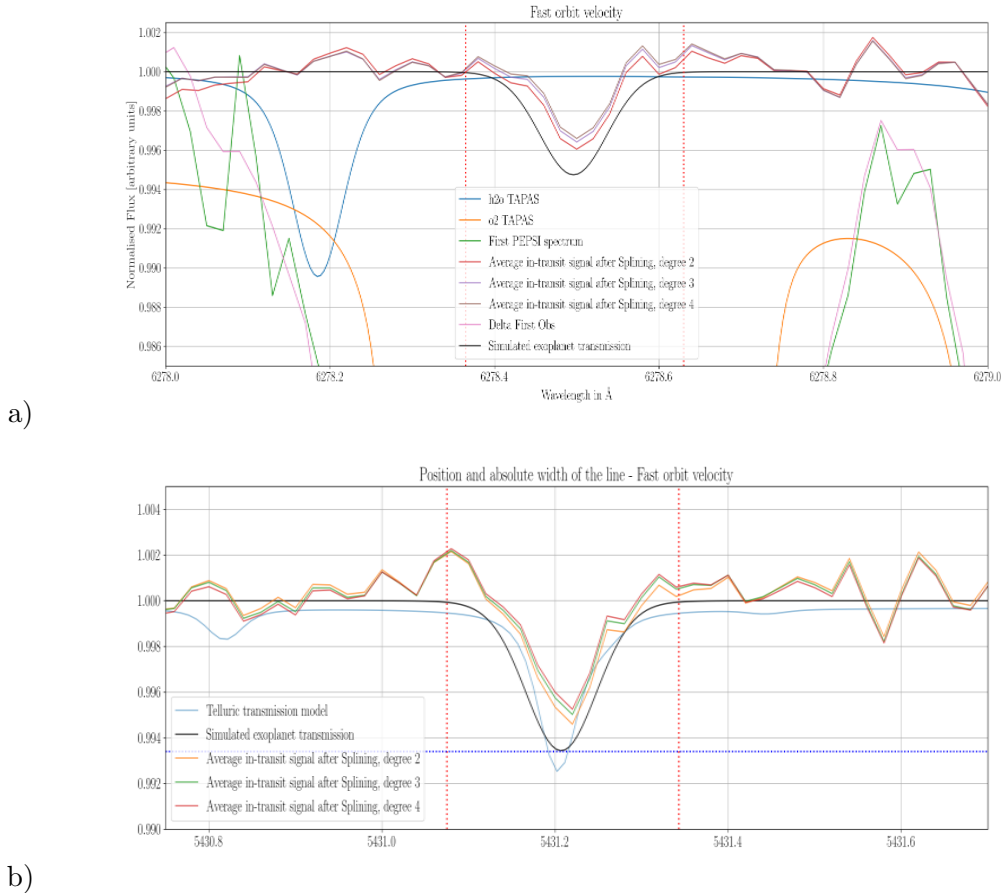Figure 4.21: Result: Faint example line

a)

b)

Figure 4.22: Result: Equivalent Widths of the Average in-transit residuals.

line at 5431 Ångström, which is not coinciding with any telluric absorption feature (indicated again by TAPAS), but it is located on a strong stellar line. Figure 4.22 c) shows the exoplanet feature at 6290.5 Ångström, which is coinciding both with a telluric H_2O and O_2 line, and it is located just between two strong stellar features.

For the first context a), the results in Table 4.3.2 show that the quadratic Spline degree captured most of the exoplanet signal. Same holds true for the second context b). Decreasing the orbital velocity of the simulated exoplanet indeed affected the performance negatively. Generally, the differences among the performances of the Spline degrees were minor for the Fast orbit velocity planet, and larger for the Slow orbit velocity planet. Likewise, the differences among the performance for a planet with a different orbital velocity were smaller with the quadratic Spline degree than with the quartic. This behavior can be observed for all two contexts.

The following Figures 4.23 show context b) in a direct comparison with the results of the two slower orbiting simulated exoplanets, for which the absorption features appear in the time series of observations at a smaller angle of tilt towards the stellar or telluric features. The results per Equivalent Width can be found in the Table above. These Figures are shown to illustrate the varying shapes of the captured 'Average in-transit residual' curve, or: the inferred exoplanet's transmission spectrum. The captured depth decreases from the Fast radial velocity towards the

True Strength (EW)	Spline°	Fast HD 189733b equivalent (-29.836 km/s at ingress)	Middle (-23.681 km/s)	Slow (-18.795 km/s)
a) **0.000543**	k2	0.000093	0.000113	0.000111
	k3	0.000077	0.000079	0.000063
	k4	0.000072	0.000063	0.000044
b) **0.000681**	k2	0.000348	0.000348	0.000295
	k3	0.000269	0.000254	0.000189
	k4	0.000223	0.000198	0.000129

Table 4.2: Result: Line strengths after Spline Correction - compared by Equivalent Width (EW), by Spline degree and by Orbital Velocity

slower velocity, albeit not equally across Spline degrees. The other difference can be seen at the flanks of the retrieved curve, which appears more and more broadened for the slower orbital velocities, and sharp for the Fast velocity exoplanet (the HD 189733b analogue).
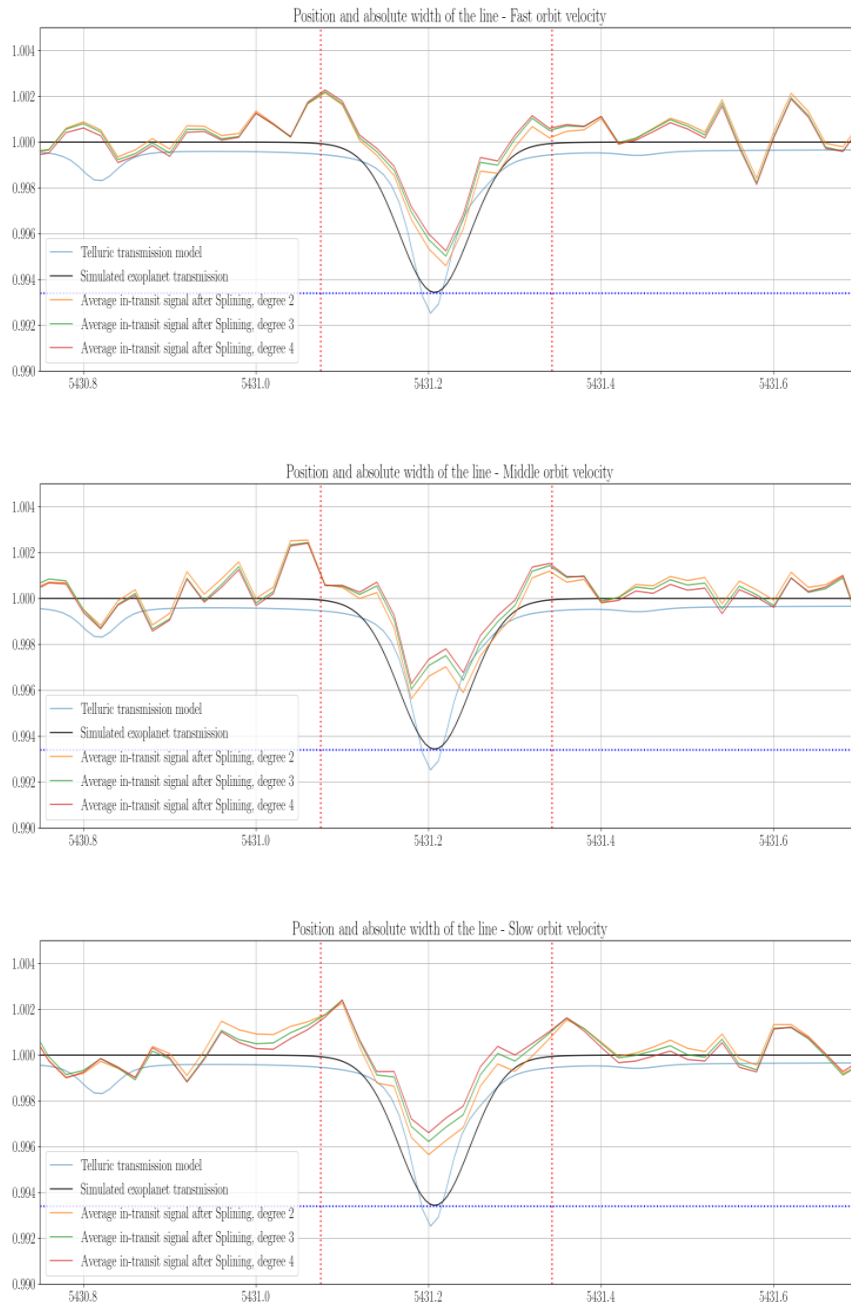
Figure 4.23: Result: Orbital velocity comparison

Chapter 5

Discussion

5.1 Main findings from the atmospheric research of Objective 1

The reported TAU Radiometer values 4.1 indicate that the night of the observation is only at the beginning of the 'Observing season', where the seeing conditions improve compared to the still high atmospheric opacity of 37-32% in the observing night. However, the TAU measurements cannot be interpreted reliably as TCWV alone, since the attenuation at the 225 GHz range can be attributed to atmospheric liquid/icy water droplets in clouds as well. Albeit, such an interpretation would be in good agreement with previous studies on the nighttime atmospheric PWV conditions at the LBT (Carrasco et al., 2017; Turchi et al., 2018). The presence of clouds in the satellite images (OLCI and the available imagery from EOSDIS Worldview, **??**) for one day prior to *and* the day after the observation (Sept 10 and 11 during daytime) suggests that the amount of atmospheric water vapor was also high during the nighttime hours. This is corroborated by the ERA5 data, which provided continuous estimates for this time frame. The TCWV values for the nighttime hours of Sept 11 show a decreasing trend, but are generally higher than for the days Sept 10 and 12. The clear daytime sky, visible in the satellite imagery for Sept 12 is also corroborated by the ERA5 estimates, that clearly show a steep decrease in TCWV over the course of the early hours on Sept 12. OLCI also measured much lower TCWV values on Sept 12, 17h, with a reduction from $8\,\mathrm{kg\,m^2}$ to $5\,\mathrm{kg\,m^2}$. The nighttime ECMWF Analysis data, that was provided to TAPAS, shows the same nighttime trend - TAPAS's simulated transmission spectra, based on this data, and integrated from the VCD into the SCD, shows a steep decrease in TCWV over night. The temporal progress of the actual telluric absorption lines in the PEPSI observations, however, does not show this steep trend. The TAPAS transmission spectra were therefore not robust enough, that they could simply be removed from the observations without closer examination. The atmospheric opacity due to water vapor has been found to be overestimated by TAPAS in previous studies as well (Ivanova et al., 2023). The reason for the overestimation can either be found in the way that TAPAS produces the transmission spectrum, or, more likely in the ECMWF data. The generally low availability atmospheric nighttime data, and the inconsistencies among the data sets that were used in this study, don't allow a confident assessment of the nighttime ECMWF values that were provided to TAPAS. A direct measurement would have been very beneficial, such as from the GPS instrument in Safford, Arizona, or from the even closer meteorological station Noon Creek on Mount Graham. This

data gap was unfortunate, but describes the very reason why an Empirical Telluric Correction approach might be advantageous. Additionally, the accuracy of the ECMWF and ERA5 products are both also negatively impacted by reduced availability, as the study by Ingleby et al. (2021) famously demonstrated. And the use of ECMWF - or ERA5 - data for the Telluric Correction of astrophysical data might be inherently impaired, as Turchi et al. (2018) suggest. Their study could demonstrate a lower suitability of ECMWF (forecast) data for 'extreme' locations, such as for other astrophysical observation sites in Chile. The study sites were characterized by generally very low PWV conditions, in high altitudes with large seasonal or diurnal variations. These conditions hindered an accurate prediction based on an interpolation from the large pixel sizes and analysis windows that ECMWF and ERA5 provide. The trend was already suggested before by Kerber et al. (2014) and Carrasco et al. (2017). The best basis for adequate telluric corrections - with model-based approaches, such as TAPAS (Bertaux et al., 2014) or Molecfit (Smette et al., 2015; Kausch et al., 2015) - in the long-term will be the direct measurement. The success of an increased use of HATPROs has already been affirmed by Kerber et al. (2015). As low-cost alternative, GNSS instruments have been investigated more closely over the past years and are strongly recommended by Wood-Vasey et al. (2022).

However, for the purpose of this study, the actual progress of the telluric absorption could be modelled nicely from the PEPSI observations, with the help of a robust telluric line atlas to guide the eye. The Figure 4.4 Showed the progress of the O_2 line (reflecting the change of airmass in the line-of-sight): The assumption was that O_2 is entirely reflecting the airmass in the LOS, increasing with Zenith Angle. Even though the Zenith angle decreases during the first half of the observations, and only then increases (strongly), there was no significant decrease in Equivalent Width visible. A reason for that might be that the increase of molecular density of O_2 in the LOS is dependent both on airmass *and* temperature, which likely increased towards the end of the observation! While the changes of airmass along the LOS during the first half of observations did not change the absorption depth significantly, the combination of increased airmass and higher temperatures led to the observed change. With a Zenith Angle of $> 30°$ for the last observations, also scattering effects could have played a larger role than assumed, or the attenuation due to O_3 in the Chappuis absorption band. This was also mostly neglected in this study. The Chappuis absorption band causes absorption in the stratospheric ozone layer, which affects only observations with longer lines-of-sight passing through this atmospheric layer. This requires further investigation.

Additionally, the combined use of the simulated telluric line atlases by Noll et al. (2012) and TAPAS Bertaux et al. (2014); ? was very useful for this study, as it increased the certainty in either the most likely line-depth, as well as a robust knowledge of the locations of absorption lines.

5.2 Main findings from the Telluric Correction and Analysis of Objective 2

For the exemplary O_2 and H_2O lines could be observed, that the Deltas were slightly too deep or too shallow at the beginning and at the end of the observation, while there were only little

to no discrepancies visible during the middle observations. Also the discrepancies between the Deltas of the different Spline degrees were few to none in these middle observations, whereas the Deltas of the First and Last Observations were slightly deviating. This corresponds very well to the Spline results for the Telluric Pixel light curve example chosen in Figures 4.14. In the top Figure, the Interpolated curves showed different behaviors mostly towards the first and last data points. In the bottom Figure, the Spline Corrected Results also showed alternating trends mostly towards the end points of the observation series, and were in very good agreement for the middle observations. Generally, the Spline degree made only little to no difference for the efficiency to remove the telluric features from the observations.

The Telluric Correction by Univariate Smoothing Spline Interpolation led to very accurate results for the removal of Telluric features. The efficiency of the method, in this perspective, did not rely on its application for the observation of an exoplanet, but rather on a tangible temporal trend within a time series of observations. With regard to the decreased atmospheric data availability for this night, this approach yielded a much more robust and accurate Telluric Removal than would have been possible with the model-based approach by TAPAS (Bertaux et al., 2014). Potentially even with regard to the generally lower atmospheric data availability for night times, in the absence of a direct atmospheric measurement in form of a HATPRO or GNSS instrument, an Empirical Correction approach might can remove the tellurics without introducing even more uncertainty. In any case, the comparison of the Deltas with the actual observation is advisable to have some measure of the goodness of the Correction. And this is highly facilitated by the use of TAPAS to guide the eye. This Empirical Correction Method is simple to use and provides fast results. This is an advantage compared to other popular Empirical Telluric Correction approaches, for example 'sysrem' (Tamuz et al., 2005; Mazeh et al., 2006), which identifies telluric - and other systemic - effects by Principle Component Analysis and removes these effects iteratively. This can be time costly and bears the chances of reducing non-existing apparent systemics (Allart et al., 2022).

Additionally, the success of this Telluric Correction could be translatable to Earth Observation use cases, where a time series of observations are analysed. This requires that anything with a tangible temporal trend is supposed to be removed from the observations, or is negligible, leaving only these features reliably undisturbed that appear almost as noise in the background of the 'contaminated' data.

Other synergy effects were already suggested prior to this thesis by Bertaux et al. (2014). The authors recommended a future collaboration in form of an automated report of inferred measurements of CH_4, CO_2, and N_2O to the NDACC system (Network for Detection of Atmospheric Composition Change). The NDACC system in fact makes use of both continuous measurements of variable greenhouse gases, but also of any reported single values for their long-term monitoring program, with the aim to increase the overall spatial and temporal coverage of atmospheric data. Bertaux et al. (2014) suggested that this would be highly useful as well for H_2O as water vapor, and that ground-based astrophysical observatories could contribute with automated monitoring from remote sites, although they don't mention how the (true) TCWV would be inferred exactly. Most observatories are indeed located at 'extreme' sites, characterized - ideally - by lower than average atmospheric PWV values. The nighttime coverage of atmospheric PWV is indeed lower

(ECMWF, 2021), and the monitoring from these locations could clearly fill a gap.

One outlook for future research would be to test the efficiency of this Correction Approach in a spectral regime, where the telluric absorption features (especially due to water vapor) are much more opaque or nearly saturated, which is the case in the J H K bands. These are located in the near infrared wavelength regime, in the narrower 'atmospheric windows', where the atmosphere is not fully opaque. These ranges, however, experience very strong telluric contamination (Birkby, 2018; Lu et al., 2021; Allart et al., 2022).

5.3 Main findings from the retrieval of the Artificial exoplanet's transmission spectrum and the Analysis of Objective 3

The incorporated artificial transmission signal was not fully retrieved. The 'Average in-transit residuals' did replicate most artificial absorption lines, but never in their full absorption depth. Some shallow lines were not confidently captured (4.21). However, the retrieval of the exoplanet transmission spectrum from the 'Average in-transit residuals' is not a straightforward replica of the artificial hidden exoplanet signal. The corrected spectra still include much noise, some of which resulting from non-removed stellar features, which appear on different pixels in every observation. In the average residual only from the 'in-transit' observations, these remnants are thus of less, or no consequence. A further analysis of the atmospheric composition of the observed exoplanet, based on this retrieved transmission spectrum, requires a cross-correlation with forward models of multiple molecules (Snellen et al., 2010; de Kok et al., 2014; Brogi and Line, 2019). This was not the purpose of this thesis. The planned scientific value of this project was to provide a quantitative estimate of the efficiency of this correction approach, from multiple perspectives. This has been established from the Earth Observation and Climate Science perspective. From the astrophysical perspective, the potential limits or constraints of this method were interesting - either by Spline degree, of application case (orbital velocity of the exoplanet). The differences in success between the Spline degrees were small for an exoplanet with a Fast orbital velocity, corresponding to that of HD 189733b, where the quadratic Spline degree yielded slightly better results, evaluated solely by the captured Equivalent Widths. The differences among Spline degrees were much stronger for the simulated exoplanet with a slow orbit velocity.

This trend supports the previous expectation that this Correction Method is more successful, when the sets of spectral features can be separated better - and less successful, when the angle of tilt due to smaller radial velocity differences is narrower. However, albeit that the trend could be reproduced, the findings of this study could not establish this trend as a 'hard limit', as the exoplanet transmission spectrum could also be retrieved for the least successful configuration of parameters. This requires further research. Some interesting and noteworthy features have be preserved effectively, as well. This includes for example the Rossiter McLaughlin Effect, that was visible as this s-shaped distortion on all stellar lines during the transit, before the Spline Correction was applied. While most parts of the stellar features before and after the transit were removed, the in-transit features remained. Even though this adds 'noise' to the 'average in-transit residuals', the Rossiter McLaughlin Effect is a feature that is actually useful to preserve. A previous study from several years ago already detected the Rossiter McLaughlin feature in
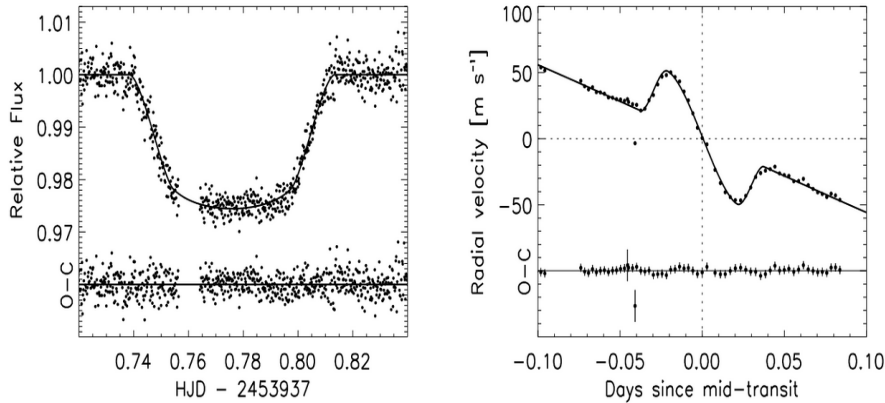
Figure 5.1: Isolated Rossiter McLaughlin Feature from another observation of HD 189733b from Winn (2006) in photometry (left) and spectroscopy (right).

observations of HD 189733b (Winn, 2006). The Figure 5.1 (left) shows the overall luminosity flux of the star (y axis) and a dip occurring during transit (the x axis denoting time) as a photometric observation (brightness measurement). The Figure 5.1 (right) shows the respective spectroscopic observation, resembling the type of observations used in this Thesis. While the x axis again denotes the time progression, the y axis denotes the 'radial velocity', which can virtually also be interpreted as pixel or wavelength; or, by how many pixels/wavelengths - by which radial velocity - the spectral features of the star were red- or blue-shifted, when the trajectory of the transiting exoplanet covered the approaching blue-shifted, or the receding red-shifted hemispheres of the star. The shape of the feature below resembles nicely the one in Figure 4.20 in the Results Section.

For future research, it would be interesting to see how well the Splining Method performs in wavelength ranges of e.g. the infrared, where telluric absorption due to water vapor is very dominant (e.g. which band numbers could be interesting). The regime of the J H K bands (Bessell, 2005) would be particularly well suited for reasons (i) the methodological performance of the Splining Method in a regime dominated by tellurics, and (ii) for the scientific revenue in a regime, where relevant absorption features of molecules are abundant (Langeveld et al., 2021; Lu et al., 2021).

5.4 Concluding remarks

In this thesis, I employed a simple Empirical Method to correct for Earth's atmospheric spectral features in an astrophysical observation series. Daytime and nighttime measurements by the TAU Radiometer, coupled with daytime measurements by OLCI, and daytime and nighttime values from the ECMWF Analysis and the ERA5 re-analysis were used to characterize the general atmospheric conditions for the time of the observation, albeit analysed separately, as the types of measurements and data provision differed. The absence of reliable direct nighttime measurements of PWV, and the heterogeneity in the collected indirect PWV values did not lead to a concise characterisation. This result was compared to the TCWV values used by TAPAS

for their simulation of the telluric transmission spectra. These were in line with the general temporal trend of my atmospheric data review. In the following comparison step, the simulated transmission spectra from TAPAS were found to partially disagree with the observed telluric (H_2O and O_2) fingerprint in the astrophysical observations. This was especially the case for the observed versus simulated temporal trends. This result is supported by previous studies which reported a disagreement between the simulated and observed transmission of atmospheric H_2O. These could be related to the anterior uncertainty in the TCWV value given to TAPAS by ECMWF. While this reduced the certainty of my analysis in some facets, it describes in fact the justification for the use of an Empirical Telluric Correction method that doesn't require previous knowledge of the atmospheric conditions. Additionally, it was shown that the simulated transmission spectra were robust enough to support the analysis of the results from the Telluric Correction, being used as a telluric line atlas to guide the eye.

The Telluric Correction by Univariate Smoothing Spline Interpolation was used to normalise for diverging temporal trends of spectral features in a time series of observations. The performance and the constraints of the Correction method were analysed with regard to (i) successfully removing the telluric features and (ii) preserving the exoplanet's transmission. These perspectives were analysed separately. For the former, the analysis revealed non-significant correction errors. Most errors occurred in the first and last observations. The results for individual pixel light curves already indicated that the Spline Interpolation fitted most closely to the central data points on the curve, and less closely to the end points. In the direct comparison of the results from the three Spline degrees, again, most deviations occurred at the end points of the pixel light curves. The applicability of this Correction method for observations in the J H K bands requires further investigation. In these bands the absorption lines caused by atmospheric H_2O are much deeper, and coincide more often with potentially interesting target features. Further investigation is also strongly suggested for the reciprocal effects: the comparison of astrophysical observations with TAPAS simulations might offer a new indirect source of atmospheric nighttime data by providing an additional confidence margin.

For the latter, the hypothesis was that the Correction Method is limited to observations, where the spectral features of the different contributors have (i) considerably different radial velocities and (ii) experience considerable radial velocity changes in a time series of observations. This general trend was supported by the findings of this study, where the depth of exemplary absorption lines in the retrieved exoplanet transmission spectrum (the average in-transit residuals), compared to the true depth of the original artificial exoplanet signal was better captured for the simulated exoplanet with a fast orbital velocity. The Telluric Spline Correction corrupted the simulated exoplanet transmissions for the slower orbital velocities more. The comparison of the results from the different Spline degrees were very small for the Fast orbiting HD 189733b analogue, and larger with a slower orbital velocity. The quadratic Spline degree yielded the best results. However, even though these results are in line with the previously hypothesised trends, the findings do not support this as a hard limit. This would require further analysis, for example by cross-correlation with a forward model of molecular transmissions, to assess which extent of distortion of the exoplanet's transmission spectrum is in fact below the - significant - detection limit. And again, further investigation is required for observations in the J H K bands, where

the absorption lines are much more profound, leaving less signal for cross-correlation after their removal.

In summary, two of the three Research Questions of this thesis could be answered confidently: the Empirical Telluric Correction Method by Univariate Smoothing Spline Interpolation is able to remove telluric spectral features efficiently from observations. The existence of correction errors for the beginning and end points of the time series have to be considered when applying the Correction Method, but can be neglected, when the analysis focuses on the mid-time-series-observations anyway. The method in itself might be applicable to Earth Observation use cases; and additionally, the comparison of simulated transmission spectra based on the available atmospheric data with astrophysical observations provides a feedback mechanism for the confidence estimation of the atmospheric data. This could increase the currently limited amount of atmospheric nighttime data for 'extreme' locations by a potentially vast amount of new 'direct measurements' from astrophysical observatories. The last Research Question could be answered partially and requires follow up research: the Empirical Correction Method did preserve the spectral features of interest in observations, and disentangled them from the contaminating features. The retrieval of an exoplanet transmission spectrum with this method is possible. But the final assessment of the correction errors cannot be done without the cross-correlation as next analysis step to identify how much of the exoplanet signal has to be preserved to be significantly detectable among the noise.

Acknowledgements

Bibliography

Brett Addison, Duncan J. Wright, Robert A. Wittenmyer, Jonathan Horner, Matthew W. Mengel, Daniel Johns, Connor Marti, Belinda Nicholson, Jack Okumura, Brendan Bowler, Ian Crossfield, Stephen R. Kane, John Kielkopf, Peter Plavchan, C. G. Tinney, Hui Zhang, Jake T. Clark, Mathieu Clerte, Jason D. Eastman, Jon Swift, Michael Bottom, Philip Muirhead, Nate McCrady, Erich Herzig, Kristina Hogstrom, Maurice Wilson, David Sliski, Samson A. Johnson, Jason T. Wright, Cullen Blake, Reed Riddle, Brian Lin, Matthew Cornachione, Timothy R. Bedding, Dennis Stello, Daniel Huber, Stephen Marsden, and Bradley D. Carter. Minerva-Australis I: Design, Commissioning, & First Photometric Results. *PASP*, 131(1005): 115003, November 2019. ISSN 0004-6280, 1538-3873. doi: 10.1088/1538-3873/ab03aa. URL http://arxiv.org/abs/1901.11231. arXiv:1901.11231 [astro-ph].

Hiroshi Akima. A New Method of Interpolation and Smooth Curve Fitting Based on Local Procedures. *J. ACM*, 17(4):589–602, October 1970. ISSN 0004-5411, 1557-735X. doi: 10.1145/321607.321609. URL https://dl.acm.org/doi/10.1145/321607.321609.

Richard P. Allan, Kate M. Willett, Viju O. John, and Tim Trent. Global Changes in Water Vapor 1979–2020. *JGR Atmospheres*, 127(12), June 2022. ISSN 2169-897X, 2169-8996. doi: 10.1029/2022JD036728. URL https://onlinelibrary.wiley.com/doi/10.1029/2022JD036728.

R. Allart, C. Lovis, J. Faria, X. Dumusque, D. Sosnowska, P. Figueira, A. M. Silva, A. Mehner, F. Pepe, S. Cristiani, R. Rebolo, N. C. Santos, V. Adibekyan, G. Cupani, P. Di Marcantonio, V. D'Odorico, J. I. González Hernández, C. J. A. P. Martins, D. Milaković, N. J. Nunes, A. Sozzetti, A. Suárez Mascareño, H. Tabernero, and M. R. Zapatero Osorio. Automatic model-based telluric correction for the ESPRESSO data reduction software: Model description and application to radial velocity computation. *A&A*, 666:A196, October 2022. ISSN 0004-6361, 1432-0746. doi: 10.1051/0004-6361/202243629. URL https://www.aanda.org/10.1051/0004-6361/202243629.

Jason W. Barnes. Effects of Orbital Eccentricity on Extrasolar Planet Transit Detectability and Light Curves. *PUBL ASTRON SOC PAC*, 119(859):986–993, September 2007. ISSN 0004-6280, 1538-3873. doi: 10.1086/522039. URL http://iopscience.iop.org/article/10.1086/522039.

Bill Bell, Hans Hersbach, Adrian Simmons, Paul Berrisford, Per Dahlgren, András Horányi, Joaquín Muñoz-Sabater, Julien Nicolas, Raluca Radu, Dinand Schepers, Cornel Soci, Sebastien Villaume, Jean-Raymond Bidlot, Leo Haimberger, Jack Woollen, Carlo Buontempo, and Jean-Noël Thépaut. The ERA5 global reanalysis: Preliminary extension to 1950. *Quart J Royal Meteoro Soc*, 147(741):4186–4227, October 2021. ISSN 0035-9009, 1477-870X. doi: 10.1002/qj.4174. URL https://onlinelibrary.wiley.com/doi/10.1002/qj.4174.

AndréL. Berger. Long-Term Variations of Daily Insolation and Quaternary Climatic Changes. *J. Atmos. Sci.*, 35(12):2362–2367, December 1978. ISSN 0022-4928, 1520-0469. doi: 10.1175/1520-0469(1978)035⟨2362:LTVODI⟩2.0.CO;2. URL http://journals.ametsoc.org/doi/10.1175/1520-0469(1978)035<2362:LTVODI>2.0.CO;2.

J. L. Bertaux, R. Lallement, S. Ferron, C. Boonne, and R. Bodichon. TAPAS, a web-based service of atmospheric transmission computation for astronomy. *A&A*, 564:A46, April 2014. ISSN 0004-6361, 1432-0746. doi: 10.1051/0004-6361/201322383. URL `http://www.aanda.org/10.1051/0004-6361/201322383`.

John E. Bertie and Zhida Lan. Infrared Intensities of Liquids XX: The Intensity of the OH Stretching Band of Liquid Water Revisited, and the Best Current Values of the Optical Constants of H $_2$ O(l) at 25°C between 15,000 and 1 cm ^{1}. *Appl Spectrosc*, 50(8):1047–1057, August 1996. ISSN 0003-7028, 1943-3530. doi: 10.1366/0003702963905385. URL `http://journals.sagepub.com/doi/10.1366/0003702963905385`.

Michael S. Bessell. Standard Photometric Systems. *Annu. Rev. Astron. Astrophys.*, 43(1):293–336, September 2005. ISSN 0066-4146, 1545-4282. doi: 10.1146/annurev.astro.41.082801.100251. URL `https://www.annualreviews.org/doi/10.1146/annurev.astro.41.082801.100251`.

Michael Bevis, Steven Businger, Thomas A. Herring, Christian Rocken, Richard A. Anthes, and Randolph H. Ware. GPS meteorology: Remote sensing of atmospheric water vapor using the global positioning system. *J. Geophys. Res.*, 97(D14):15787, 1992. ISSN 0148-0227. doi: 10.1029/92JD01517. URL `http://doi.wiley.com/10.1029/92JD01517`.

J. Birkby. Exoplanet Atmospheres at High Spectral Resolution, June 2018. URL `http://arxiv.org/abs/1806.04617`. arXiv:1806.04617 [astro-ph].

J. Birkby, R. de Kok, M. Brogi, H. Schwarz, S. Albrecht, E. de Mooij, and I. Snellen. Characterising Exoplanet Atmospheres with High-resolution Spectroscopy. *The Messenger*, 154:57–61, December 2013a. ISSN 0722-6691. URL `https://ui.adsabs.harvard.edu/abs/2013Msngr.154...57B`. ADS Bibcode: 2013Msngr.154...57B.

J. L. Birkby, R. J. de Kok, M. Brogi, E. J. W. de Mooij, H. Schwarz, S. Albrecht, and I. A. G. Snellen. Detection of water absorption in the day side atmosphere of HD 189733 b using ground-based high-resolution spectroscopy at 3.2 m. *Monthly Notices of the Royal Astronomical Society: Letters*, 436(1):L35–L39, November 2013b. ISSN 1745-3933, 1745-3925. doi: 10.1093/mnrasl/slt107. URL `http://academic.oup.com/mnrasl/article/436/1/L35/989813/Detection-of-water-absorption-in-the-day-side`.

A. S. Bonomo, S. Desidera, S. Benatti, F. Borsa, S. Crespi, M. Damasso, A. F. Lanza, A. Sozzetti, G. Lodato, F. Marzari, C. Boccato, R. U. Claudi, R. Cosentino, E. Covino, R. Gratton, A. Maggio, G. Micela, E. Molinari, I. Pagano, G. Piotto, E. Poretti, R. Smareglia, L. Affer, K. Biazzo, A. Bignamini, M. Esposito, P. Giacobbe, G. Hébrard, L. Malavolta, J. Maldonado, L. Mancini, A. Martinez Fiorenzano, S. Masiero, V. Nascimbeni, M. Pedani, M. Rainer, and G. Scandariato. The GAPS Programme with HARPS-N@TNG XIV. Investigating giant planet migration history via improved eccentricity and mass determination for 231 transiting planets. *A&A*, 602:A107, June 2017. ISSN 0004-6361, 1432-0746. doi: 10.1051/0004-6361/201629882. URL `http://arxiv.org/abs/1704.00373`. arXiv:1704.00373 [astro-ph].

F. Borsa, R. Allart, N. Casasayas-Barris, H. Tabernero, M. R. Zapatero Osorio, S. Cristiani, F. Pepe, R. Rebolo, N. C. Santos, V. Adibekyan, V. Bourrier, O. D. S. Demangeon, D. Ehrenreich, E. Pallé, S. Sousa, J. Lillo-Box, C. Lovis, G. Micela, M. Oshagh, E. Poretti, A. Sozzetti, C. Allende Prieto, Y. Alibert, M. Amate, W. Benz, F. Bouchy, A. Cabral, H. Dekker, V. D'Odorico, P. Di Marcantonio, P. Figueira, R. Genova Santos, J. I. González Hernández, G. Lo Curto, A. Manescau, C. J. A. P. Martins, D. Mégevand, A. Mehner, P. Molaro, N. J. Nunes, M. Riva, A. Suárez Mascareño, S. Udry, and F. Zerbi. Atmospheric Rossiter–McLaughlin effect and transmission spectroscopy of WASP-121b with ESPRESSO. *A&A*, 645:A24, January 2021. ISSN 0004-6361, 1432-0746. doi: 10.1051/0004-6361/202039344. URL `https://www.aanda.org/10.1051/0004-6361/202039344`.

William J. Borucki and Audrey L. Summers. The photometric method of detecting other planetary systems. *Icarus*, 58(1):121–134, April 1984. ISSN 00191035. doi: 10.1016/0019-1035(84)90102-7. URL https://linkinghub.elsevier.com/retrieve/pii/0019103584901027.

Francois Bouchy, Stephane Udry, Michel Mayor, Claire Moutou, Frederic Pont, Nicolas Iribarne, Ronaldo Da Silva, Sergio Ilovaisky, Didier Queloz, Nuno Santos, Damien Segransan, and Shay Zucker. ELODIE metallicity-biased search for transiting Hot Jupiters II. A very hot Jupiter transiting the bright K star HD189733. *A&A*, 444(1):L15–L19, December 2005. ISSN 0004-6361, 1432-0746. doi: 10.1051/0004-6361:200500201. URL http://arxiv.org/abs/astro-ph/0510119. arXiv:astro-ph/0510119.

J. Brion, A. Chakir, J. Charbonnier, D. Daumont, C. Parisse, and J. Malicet. Absorption Spectra Measurements for the Ozone Molecule in the 350–830 nm Region. *Journal of Atmospheric Chemistry*, 30(2):291–299, 1998. ISSN 01677764. doi: 10.1023/A:1006036924364. URL http://link.springer.com/10.1023/A:1006036924364.

M. Brogi, I. A. G. Snellen, R. J. De Kok, S. Albrecht, J. L. Birkby, and E. J. W. De Mooij. DETECTION OF MOLECULAR ABSORPTION IN THE DAYSIDE OF EXOPLANET 51 PEGASI b? *ApJ*, 767(1):27, March 2013. ISSN 0004-637X, 1538-4357. doi: 10.1088/0004-637X/767/1/27. URL https://iopscience.iop.org/article/10.1088/0004-637X/767/1/27.

M. Brogi, R. J. De Kok, S. Albrecht, I. A. G. Snellen, J. L. Birkby, and H. Schwarz. ROTATION AND WINDS OF EXOPLANET HD 189733 b MEASURED WITH HIGH-DISPERSION TRANSMISSION SPECTROSCOPY. *ApJ*, 817(2):106, January 2016. ISSN 1538-4357. doi: 10.3847/0004-637X/817/2/106. URL https://iopscience.iop.org/article/10.3847/0004-637X/817/2/106.

M. Brogi, P. Giacobbe, G. Guilluy, R. J. de Kok, A. Sozzetti, L. Mancini, and A. S. Bonomo. Exoplanet atmospheres with GIANO: I. Water in the transmission spectrum of HD 189 733 b. *A&A*, 615:A16, July 2018. ISSN 0004-6361, 1432-0746. doi: 10.1051/0004-6361/201732189. URL https://www.aanda.org/10.1051/0004-6361/201732189.

Matteo Brogi and Michael R. Line. Retrieving Temperatures and Abundances of Exoplanet Atmospheres with High-Resolution Cross-Correlation Spectroscopy. *AJ*, 157(3):114, February 2019. ISSN 1538-3881. doi: 10.3847/1538-3881/aaffd3. URL http://arxiv.org/abs/1811.01681. arXiv:1811.01681 [astro-ph].

Anthony G. A. Brown. Microarcsecond Astrometry: Science Highlights from Gaia. *Annu. Rev. Astron. Astrophys.*, 59(1):59–115, September 2021. ISSN 0066-4146, 1545-4282. doi: 10.1146/annurev-astro-112320-035628. URL http://arxiv.org/abs/2102.11712. arXiv:2102.11712 [astro-ph].

A. Collier Cameron, V. A. Bruce, G. R. M. Miller, A. H. M. J. Triaud, and D. Queloz. Line-profile tomography of exoplanet transits I: The Doppler shadow of HD 189733b. *Monthly Notices of the Royal Astronomical Society*, 403(1):151–158, March 2010. ISSN 00358711, 13652966. doi: 10.1111/j.1365-2966.2009.16131.x. URL http://arxiv.org/abs/0911.5361. arXiv:0911.5361 [astro-ph].

Carla Cardinali and Sean Healy. Impact of GPS radio occultation measurements in the ECMWF system using adjoint based diagnostics. 2013. doi: 10.21957/AIMMDXV2. URL https://www.ecmwf.int/node/8585. Publisher: ECMWF.

E. Carrasco, R. Avila, A. Erasmus, S. G. Djorgovski, A. R. Walker, and R. Blum. A Satellite Survey of Cloud Cover and Water Vapor in the Southwestern USA and Northern Mexico. *PASP*, 129(973):035005, March 2017. ISSN 0004-6280, 1538-3873. doi: 10.1088/1538-3873/129/

973/035005. URL `https://iopscience.iop.org/article/10.1088/1538-3873/129/973/035005`.

Bradley W. Carroll and Dale A. Ostlie. *An introduction to modern astrophysics*. Pearson, Harlow, 2. ed., pearson new internat. ed edition, 2014. ISBN 978-1-292-02293-2.

David Charbonneau, Timothy M. Brown, David W. Latham, and Michel Mayor. Detection of Planetary Transits Across a Sun-like Star. *The Astrophysical Journal*, 529(1):L45–L48, January 2000. ISSN 0004637X. doi: 10.1086/312457. URL `https://iopscience.iop.org/article/10.1086/312457`.

David Charbonneau, Timothy M. Brown, Robert W. Noyes, and Ronald L. Gilliland. Detection of an Extrasolar Planet Atmosphere. *ApJ*, 568(1):377–384, March 2002. ISSN 0004-637X, 1538-4357. doi: 10.1086/338770. URL `https://iopscience.iop.org/article/10.1086/338770`.

Ming-Yen Cheng, Liang Peng, and Jyh-Shyang Wu. Reducing variance in univariate smoothing. *Ann. Statist.*, 35(2), April 2007. ISSN 0090-5364. doi: 10.1214/009053606000001398. URL `https://projecteuclid.org/journals/annals-of-statistics/volume-35/issue-2/Reducing-variance-in-univariate-smoothing/10.1214/009053606000001398.full`.

L. M. Close, K. B. Follette, J. R. Males, A. Puglisi, M. Xompero, D. Apai, J. Najita, A. J. Weinberger, K. Morzinski, T. J. Rodigas, P. Hinz, V. Bailey, and R. Briguglio. DISCOVERY OF H EMISSION FROM THE CLOSE COMPANION INSIDE THE GAP OF TRANSITIONAL DISK HD 142527. *ApJ*, 781(2):L30, January 2014. ISSN 2041-8205, 2041-8213. doi: 10.1088/2041-8205/781/2/L30. URL `https://iopscience.iop.org/article/10.1088/2041-8205/781/2/L30`.

S. A. Clough and M. J. Iacono. Line-by-line calculation of atmospheric fluxes and cooling rates: 2. Application to carbon dioxide, ozone, methane, nitrous oxide and the halocarbons. *J. Geophys. Res.*, 100(D8):16519, 1995. ISSN 0148-0227. doi: 10.1029/95JD01386. URL `http://doi.wiley.com/10.1029/95JD01386`.

Ian J. M. Crossfield and Laura Kreidberg. Trends in Atmospheric Properties of Neptune-size Exoplanets. *AJ*, 154(6):261, November 2017. ISSN 1538-3881. doi: 10.3847/1538-3881/aa9279. URL `https://iopscience.iop.org/article/10.3847/1538-3881/aa9279`.

R. J. de Kok, J. Birkby, M. Brogi, H. Schwarz, S. Albrecht, E. J. W. de Mooij, and I. A. G. Snellen. Identifying new opportunities for exoplanet characterisation at high spectral resolution. *A&A*, 561:A150, January 2014. ISSN 0004-6361, 1432-0746. doi: 10.1051/0004-6361/201322947. URL `http://www.aanda.org/10.1051/0004-6361/201322947`.

R.J. De Kok, M. Brogi, I.A.G. Snellen, J. Birkby, S. Albrecht, and E.J.W. De Mooij. Detection of carbon monoxide in the high-resolution day-side spectrum of the exoplanet HD 189733b. *A&A*, 554:A82, June 2013. ISSN 0004-6361, 1432-0746. doi: 10.1051/0004-6361/201321381. URL `http://www.aanda.org/10.1051/0004-6361/201321381`.

A. E. Dessler and S. Wong. Estimates of the Water Vapor Climate Feedback during El Niño–Southern Oscillation. *Journal of Climate*, 22(23):6404–6412, December 2009. ISSN 1520-0442, 0894-8755. doi: 10.1175/2009JCLI3052.1. URL `http://journals.ametsoc.org/doi/10.1175/2009JCLI3052.1`.

H. Diedrich, R. Preusker, R. Lindstrot, and J. Fischer. Quantification of uncertainties of water vapour column retrievals using future instruments. *Atmos. Meas. Tech.*, 6(2):359–370, February 2013. ISSN 1867-8548. doi: 10.5194/amt-6-359-2013. URL `https://amt.copernicus.org/articles/6/359/2013/`.

H. Diedrich, R. Preusker, R. Lindstrot, and J. Fischer. Retrieval of daytime total columnar water vapour from MODIS measurements over land surfaces. *Atmos. Meas. Tech.*, 8(2): 823–836, February 2015. ISSN 1867-8548. doi: 10.5194/amt-8-823-2015. URL `https://amt.copernicus.org/articles/8/823/2015/`.

Hannes Diedrich, Falco Wittchen, René Preusker, and Jürgen Fischer. Representativeness of total column water vapour retrievals from instruments on polar orbiting satellites. *Atmos. Chem. Phys.*, 16(13):8331–8339, July 2016. ISSN 1680-7324. doi: 10.5194/acp-16-8331-2016. URL `https://acp.copernicus.org/articles/16/8331/2016/`.

ECMWF. IFS Documentation CY47R1 - Part II: Data Assimilation. 2020a. doi: 10.21957/0GTYBBWP9. URL `https://www.ecmwf.int/node/19746`. Publisher: ECMWF.

ECMWF. IFS Documentation CY47R1 - Part III: Dynamics and Numerical Procedures. 2020b. doi: 10.21957/U8SSD58. URL `https://www.ecmwf.int/node/19747`. Publisher: ECMWF.

ECMWF. IFS Documentation CY47R1 - Part V: Ensemble Prediction System. 2020c. doi: 10.21957/D7E3HRB. URL `https://www.ecmwf.int/node/19749`. Publisher: ECMWF.

ECMWF. IFS Documentation CY47R3 - Part I: Observations. 2021. doi: 10.21957/YCOW5YJR1. URL `https://www.ecmwf.int/node/20195`. Publisher: ECMWF.

Thomas Eversberg and Klaus Vollmann. *Spectroscopic instrumentation: fundamentals and guidelines for astronomers.* Springer, New York, 2014. ISBN 978-3-662-44534-1.

P. Figueira, F. Pepe, C. Lovis, and M. Mayor. Evaluating the stability of atmospheric lines with HARPS. *A&A*, 515:A106, June 2010. ISSN 0004-6361, 1432-0746. doi: 10.1051/0004-6361/201014005. URL `http://www.aanda.org/10.1051/0004-6361/201014005`.

B. Scott Gaudi, Jessie L. Christiansen, and Michael R. Meyer. *The Demographics of Exoplanets.* October 2021. doi: 10.1088/2514-3433/abfa8fch2. URL `http://arxiv.org/abs/2011.04703`. arXiv:2011.04703 [astro-ph].

S. Gebauer, J. L. Grenfell, J. W. Stock, R. Lehmann, M. Godolt, P. von Paris, and H. Rauer. Evolution of Earth-like extrasolar planetary atmospheres: Assessing the atmospheres and biospheres of early Earth analog planets with a coupled atmosphere biogeochemical model. *Astrobiology*, 17(1):27–54, January 2017. ISSN 1531-1074, 1557-8070. doi: 10.1089/ast.2015.1384. URL `http://arxiv.org/abs/1807.06844`. arXiv:1807.06844 [astro-ph].

I.E. Gordon, L.S. Rothman, R.J. Hargreaves, R. Hashemi, E.V. Karlovets, F.M. Skinner, E.K. Conway, C. Hill, R.V. Kochanov, Y. Tan, P. Wcisło, A.A. Finenko, K. Nelson, P.F. Bernath, M. Birk, V. Boudon, A. Campargue, K.V. Chance, A. Coustenis, B.J. Drouin, J.–M. Flaud, R.R. Gamache, J.T. Hodges, D. Jacquemart, E.J. Mlawer, A.V. Nikitin, V.I. Perevalov, M. Rotger, J. Tennyson, G.C. Toon, H. Tran, V.G. Tyuterev, E.M. Adkins, A. Baker, A. Barbe, E. Canè, A.G. Császár, A. Dudaryonok, O. Egorov, A.J. Fleisher, H. Fleurbaey, A. Foltynowicz, T. Furtenbacher, J.J. Harrison, J.–M. Hartmann, V.–M. Horneman, X. Huang, T. Karman, J. Karns, S. Kassi, I. Kleiner, V. Kofman, F. Kwabia–Tchana, N.N. Lavrentieva, T.J. Lee, D.A. Long, A.A. Lukashevskaya, O.M. Lyulin, V.Yu. Makhnev, W. Matt, S.T. Massie, M. Melosso, S.N. Mikhailenko, D. Mondelain, H.S.P. Müller, O.V. Naumenko, A. Perrin, O.L. Polyansky, E. Raddaoui, P.L. Raston, Z.D. Reed, M. Rey, C. Richard, R. Tóbiás, I. Sadiek, D.W. Schwenke, E. Starikova, K. Sung, F. Tamassia, S.A. Tashkun, J. Vander Auwera, I.A. Vasilenko, A.A. Vigasin, G.L. Villanueva, B. Vispoel, G. Wagner, A. Yachmenev, and S.N. Yurchenko. The HITRAN2020 molecular spectroscopic database. *Journal of Quantitative Spectroscopy and Radiative Transfer*, 277:107949, January 2022. ISSN 00224073. doi: 10.1016/j.jqsrt.2021.107949. URL `https://linkinghub.elsevier.com/retrieve/pii/S0022407321004416`.

W. Hazeleger, B.J.J.M. Van Den Hurk, E. Min, G.J. Van Oldenborgh, A.C. Petersen, D.A. Stainforth, E. Vasileiadou, and L.A. Smith. Tales of future weather. *Nature Clim Change*, 5 (2):107–113, February 2015. ISSN 1758-678X, 1758-6798. doi: 10.1038/nclimate2450. URL `https://www.nature.com/articles/nclimate2450`.

Kevin Heng. A CLOUDINESS INDEX FOR TRANSITING EXOPLANETS BASED ON THE SODIUM AND POTASSIUM LINES: TENTATIVE EVIDENCE FOR HOTTER ATMOSPHERES BEING LESS CLOUDY AT VISIBLE WAVELENGTHS. *ApJ*, 826 (1):L16, July 2016. ISSN 2041-8213. doi: 10.3847/2041-8205/826/1/L16. URL `https://iopscience.iop.org/article/10.3847/2041-8205/826/1/L16`.

Gregory W. Henry, Geoffrey W. Marcy, R. Paul Butler, and Steven S. Vogt. A Transiting "51 Peg–like" Planet. *The Astrophysical Journal*, 529(1):L41–L44, January 2000. ISSN 0004637X. doi: 10.1086/312458. URL `https://iopscience.iop.org/article/10.1086/312458`.

Hans Hersbach, W Bell, P. Berrisford, Andras Horányi, Muñoz-Sabater J., J. Nicolas, Raluca Radu, Dinand Schepers, Adrian Simmons, Cornel Soci, and Dick Dee. Global reanalysis: goodbye ERA-Interim, hello ERA5. 2019. doi: 10.21957/VF291HEHD7. URL `https://www.ecmwf.int/node/19027`. Publisher: ECMWF.

Hans Hersbach, Bill Bell, Paul Berrisford, Shoji Hirahara, András Horányi, Joaquín Muñoz-Sabater, Julien Nicolas, Carole Peubey, Raluca Radu, Dinand Schepers, Adrian Simmons, Cornel Soci, Saleh Abdalla, Xavier Abellan, Gianpaolo Balsamo, Peter Bechtold, Gionata Biavati, Jean Bidlot, Massimo Bonavita, Giovanna Chiara, Per Dahlgren, Dick Dee, Michail Diamantakis, Rossana Dragani, Johannes Flemming, Richard Forbes, Manuel Fuentes, Alan Geer, Leo Haimberger, Sean Healy, Robin J. Hogan, Elías Hólm, Marta Janisková, Sarah Keeley, Patrick Laloyaux, Philippe Lopez, Cristina Lupu, Gabor Radnoti, Patricia Rosnay, Iryna Rozum, Freja Vamborg, Sebastien Villaume, and Jean-Noël Thépaut. The ERA5 global reanalysis. *Q.J.R. Meteorol. Soc.*, 146(730):1999–2049, July 2020. ISSN 0035-9009, 1477-870X. doi: 10.1002/qj.3803. URL `https://onlinelibrary.wiley.com/doi/10.1002/qj.3803`.

Øivind Hodnebrog, Gunnar Myhre, Bjørn H. Samset, Kari Alterskjær, Timothy Andrews, Olivier Boucher, Gregory Faluvegi, Dagmar Fläschner, Piers M. Forster, Matthew Kasoar, Alf Kirkevåg, Jean-Francois Lamarque, Dirk Olivié, Thomas B. Richardson, Dilshad Shawki, Drew Shindell, Keith P. Shine, Philip Stier, Toshihiko Takemura, Apostolos Voulgarakis, and Duncan Watson-Parris. Water vapour adjustments and responses differ between climate drivers. *Atmos. Chem. Phys.*, 19(20):12887–12899, October 2019. ISSN 1680-7324. doi: 10.5194/acp-19-12887-2019. URL `https://acp.copernicus.org/articles/19/12887/2019/`.

Tim-Oliver Husser and Kathrin Ulbrich. Using a model for telluric absorption in full-spectrum fits, December 2013. URL `http://arxiv.org/abs/1312.2450`. arXiv:1312.2450 [astro-ph].

Ilya Ilyin, Michael Weber, Arto Järvinen, Manfred Woche, Silva Järvinen, Daniel Sablowski, Matthias Mallonn, Engin Keles, Thorsten Carroll, Marshall C. Johnson, R. Mark Wagner, Christian Veillet, Klaus G. Strassmeier, and Chad Bender. Want a PEPSI? Performance status of the recently commissioned high-resolution spectrograph and polarimeter for the 2x8.4m Large Binocular Telescope. In Hideki Takami, Christopher J. Evans, and Luc Simard, editors, *Ground-based and Airborne Instrumentation for Astronomy VII*, page 38, Austin, United States, July 2018. SPIE. ISBN 978-1-5106-1957-9 978-1-5106-1958-6. doi: 10.1117/12.2311627. URL `https://www.spiedigitallibrary.org/conference-proceedings-of-spie/10702/2311627/Want-a-PEPSI-Performance-status-of-the-recently-commissioned-high/10.1117/12.2311627.full`.

Bruce Ingleby, Brett Candy, John Eyre, Thomas Haiden, Christopher Hill, Lars Isaksen, Daryl Kleist, Fiona Smith, Peter Steinle, Stewart Taylor, Warren Tennant, and Christopher Tingwell.

The Impact of COVID-19 on Weather Forecasts: A Balanced View. *Geophys Res Lett*, 48(4), February 2021. ISSN 0094-8276, 1944-8007. doi: 10.1029/2020GL090699. URL `https://onlinelibrary.wiley.com/doi/10.1029/2020GL090699`.

Intergovernmental Panel On Climate Change (Ipcc). *Climate Change 2022 – Impacts, Adaptation and Vulnerability: Working Group II Contribution to the Sixth Assessment Report of the Intergovernmental Panel on Climate Change.* Cambridge University Press, 1 edition, June 2023. ISBN 978-1-00-932584-4. doi: 10.1017/9781009325844. URL `https://www.cambridge.org/core/product/identifier/9781009325844/type/book`.

A. Ivanova, R. Lallement, and J. L. Bertaux. Improved precision of radial velocity measurements after correction for telluric absorption, February 2023. URL `http://arxiv.org/abs/2302.03897`. arXiv:2302.03897 [astro-ph].

Niilo Kalakoski, Viktoria F. Sofieva, René Preusker, Claire Henocq, Matthieu Denisselle, Steffen Dransfeld, and Silvia Scifoni. Validation of Copernicus Sentinel-3/OLCI Level 2 Land Integrated Water Vapour product. *Atmos. Meas. Tech.*, 15(17):5129–5140, September 2022. ISSN 1867-8548. doi: 10.5194/amt-15-5129-2022. URL `https://amt.copernicus.org/articles/15/5129/2022/`.

W. Kausch, S. Noll, A. Smette, S. Kimeswenger, M. Barden, C. Szyszka, A. M. Jones, H. Sana, H. Horst, and F. Kerber. Molecfit: A general tool for telluric absorption correction: II. Quantitative evaluation on ESO-VLT/X-Shooterspectra. *A&A*, 576:A78, April 2015. ISSN 0004-6361, 1432-746. doi: 10.1051/0004-6361/201423909. URL `http://www.aanda.org/10.1051/0004-6361/201423909`.

E. Keles, D. Kitzmann, M. Mallonn, X. Alexoudi, L. Fossati, L. Pino, J. V. Seidel, T. A. Carroll, M. Steffen, I. Ilyin, K. Poppenhaeger, K. G. Strassmeier, C. von Essen, V. Nascimbeni, and J. D. Turner. Probing the atmosphere of HD189733b with the Na I and K I lines. *Monthly Notices of the Royal Astronomical Society*, 498(1):1023–1033, October 2020. ISSN 0035-8711, 1365-2966. doi: 10.1093/mnras/staa2435. URL `http://arxiv.org/abs/2008.04044`. arXiv:2008.04044 [astro-ph].

Engin Keles, Matthias Mallonn, Carolina von Essen, Thorsten A. Carroll, Xanthippi Alexoudi, Lorenzo Pino, Ilya Ilyin, Katja Poppenhaeger, Daniel Kitzmann, Valerio Nascimbeni, Jake Turner, and Klaus G. Strassmeier. The potassium absorption on HD189733b and HD209458b. *Monthly Notices of the Royal Astronomical Society: Letters*, 489(1):L37–L41, October 2019. ISSN 1745-3925, 1745-3933. doi: 10.1093/mnrasl/slz123. URL `http://arxiv.org/abs/1909.04884`. arXiv:1909.04884 [astro-ph].

Engin Keles, Matthias Mallonn, Daniel Kitzmann, Katja Poppenhaeger, H. Jens Hoeijmakers, Ilya Ilyin, Xanthippi Alexoudi, Thorsten A. Carroll, Julian Alvarado-Gomez, Laura Ketzer, Aldo S. Bonomo, Francesco Borsa, Scott Gaudi, Thomas Henning, Luca Malavolta, Karan Molaverdikhani, Valerio Nascimbeni, Jennifer Patience, Lorenzo Pino, Gaetano Scandariato, Everett Schlawin, Evgenya Shkolnik, Daniela Sicilia, Alessandro Sozzetti, Mary G. Foster, Christian Veillet, Ji Wang, Fei Yan, and Klaus G. Strassmeier. The PEPSI Exoplanet Transit Survey (PETS) I: Investigating the presence of a silicate atmosphere on the super-Earth 55 Cnc e. *Monthly Notices of the Royal Astronomical Society*, 513(1):1544–1556, April 2022. ISSN 0035-8711, 1365-2966. doi: 10.1093/mnras/stac810. URL `http://arxiv.org/abs/2203.16856`. arXiv:2203.16856 [astro-ph].

F. Kerber, R. R. Querel, R. Rondanelli, R. Hanuschik, M. Van Den Ancker, O. Cuevas, A. Smette, J. Smoker, T. Rose, and H. Czekala. An episode of extremely low precipitable water vapour over Paranal observatory. *Monthly Notices of the Royal Astronomical Society*, 439(1):247–255, March 2014. ISSN 1365-2966, 0035-8711. doi: 10.

1093/mnras/stt2404. URL `http://academic.oup.com/mnras/article/439/1/247/971721/`
`An-episode-of-extremely-low-precipitable-water`.

Florian Kerber, Richard R Querel, and Bianca Neureiter. The water vapour radiometer of Paranal:
homogeneity of precipitable water vapour from two years of operations. *J. Phys.: Conf. Ser.*,
595:012017, April 2015. ISSN 1742-6588, 1742-6596. doi: 10.1088/1742-6596/595/1/012017.
URL `https://iopscience.iop.org/article/10.1088/1742-6596/595/1/012017`.

Anna Klos, Addisu Hunegnaw, Felix Norman Teferle, Kibrom Ebuy Abraha, Furqan Ahmed,
and Janusz Bogusz. Statistical significance of trends in Zenith Wet Delay from re-processed
GPS solutions. *GPS Solut*, 22(2):51, April 2018. ISSN 1080-5370, 1521-1886. doi: 10.1007/
s10291-018-0717-y. URL `http://link.springer.com/10.1007/s10291-018-0717-y`.

Stefan Kneifel, Stephanie Redl, Emiliano Orlandi, Ulrich Löhnert, Maria P. Cadeddu, David D.
Turner, and Ming-Tang Chen. Absorption Properties of Supercooled Liquid Water between 31
and 225 GHz: Evaluation of Absorption Models Using Ground-Based Observations. *Journal of
Applied Meteorology and Climatology*, 53(4):1028–1045, April 2014. ISSN 1558-8424, 1558-8432.
doi: 10.1175/JAMC-D-13-0214.1. URL `https://journals.ametsoc.org/view/journals/`
`apme/53/4/jamc-d-13-0214.1.xml`.

A. Kokori, A. Tsiaras, B. Edwards, M. Rocchetto, G. Tinetti, L. Bewersdorff, Y. Jongen,
G. Lekkas, G. Pantelidou, E. Poultourtzidis, A. Wünsche, C. Aggelis, V. K. Agnihotri,
C. Arena, M. Bachschmidt, D. Bennett, P. Benni, K. Bernacki, E. Besson, L. Betti, A. Biagini,
P. Brandebourg, M. Bretton, S. M. Brincat, M. Caló, F. Campos, R. Casali, R. Ciantini,
M. V. Crow, B. Dauchet, S. Dawes, M. Deldem, D. Deligeorgopoulos, R. Dymock, T. Eenmäe,
P. Evans, N. Esseiva, C. Falco, S. Ferratfiat, M. Fowler, S. R. Futcher, J. Gaitan, F. Grau
Horta, P. Guerra, F. Hurter, A. Jones, W. Kang, H. Kiiskinen, T. Kim, D. Laloum, R. Lee,
F. Lomoz, C. Lopresti, M. Mallonn, M. Mannucci, A. Marino, J.-C. Mario, J.-B. Marquette,
J. Michelet, M. Miller, T. Mollier, D. Molina, N. Montigiani, F. Mortari, M. Morvan, L. V.
Mugnai, L. Naponiello, A. Nastasi, R. Neito, E. Pace, P. Papadeas, N. Paschalis, C. Pereira,
V. Perroud, M. Phillips, P. Pintr, J.-B. Pioppa, A. Popowicz, M. Raetz, F. Regembal, K. Rickard,
M. Roberts, L. Rousselot, X. Rubia, J. Savage, D. Sedita, D. Shave-Wall, N. Sioulas, V. Školník,
M. Smith, D. St-Gelais, D. Stouraitis, I. Strikis, G. Thurston, A. Tomacelli, A. Tomatis,
B. Trevan, P. Valeau, J.-P. Vignes, K. Vora, M. Vrašťák, F. Walter, B. Wenzel, D. E.
Wright, and M. Zíbar. ExoClock project II: A large-scale integrated study with 180 updated
exoplanet ephemerides. *ApJS*, 258(2):40, February 2022. ISSN 0067-0049, 1538-4365. doi:
10.3847/1538-4365/ac3a10. URL `http://arxiv.org/abs/2110.13863`. arXiv:2110.13863
[astro-ph].

Joshua Krissansen-Totton, Stephanie Olson, and David C. Catling. Disequilibrium biosignatures
over Earth history and implications for detecting exoplanet life. *Sci. Adv.*, 4(1):eaao5747,
January 2018. ISSN 2375-2548. doi: 10.1126/sciadv.aao5747. URL `https://www.science.`
`org/doi/10.1126/sciadv.aao5747`.

David B. Kunkee, Gene A. Poe, Donald J. Boucher, Steven D. Swadley, Ye Hong, John E.
Wessel, and Enzo A. Uliana. Design and Evaluation of the First Special Sensor Microwave
Imager/Sounder. *IEEE Trans. Geosci. Remote Sensing*, 46(4):863–883, April 2008. ISSN
0196-2892. doi: 10.1109/TGRS.2008.917980. URL `http://ieeexplore.ieee.org/document/`
`4475705/`.

Kenneth R. Lang. *Astrophysical formulae*. Astronomy and astrophysics library. Springer, Berlin,
3rd enlarged and revised ed edition, 2006. ISBN 978-3-540-29692-8.

Ulrike Langematz. Stratospheric ozone: down and up through the anthropocene. *ChemTexts*, 5(2):8, June 2019. ISSN 2199-3793. doi: 10.1007/s40828-019-0082-7. URL `http://link.springer.com/10.1007/s40828-019-0082-7`.

Adam B. Langeveld, Nikku Madhusudhan, Samuel H. C. Cabot, and Simon T. Hodgkin. Assessing telluric correction methods for Na detections with high-resolution exoplanet transmission spectroscopy. *Monthly Notices of the Royal Astronomical Society*, 502(3):4392–4404, February 2021. ISSN 0035-8711, 1365-2966. doi: 10.1093/mnras/stab134. URL `http://arxiv.org/abs/2101.05283`. arXiv:2101.05283 [astro-ph].

Belinda Linden. Basic Blue Skies Research in the UK: Are we losing out? *J Biomed Discov Collaboration*, 3(1):3, 2008. ISSN 1747-5333. doi: 10.1186/1747-5333-3-3. URL `http://j-biomed-discovery.biomedcentral.com/articles/10.1186/1747-5333-3-3`.

Manasvi Lingam and Abraham Loeb. Is Life Most Likely Around Sun-like Stars? 2017. doi: 10.48550/ARXIV.1710.11134. URL `https://arxiv.org/abs/1710.11134`. Publisher: arXiv Version Number: 2.

Kai-Xing Lu, Zhi-Xiang Zhang, Ying-Ke Huang, An-Bing Ren, Liang Xu, Hai-Cheng Feng, Yu-Xin Xin, Xu Ding, Xiao-Guang Yu, and Jin-Ming Bai. A correction method for the telluric absorptions and application to Lijiang Observatory. *Res. Astron. Astrophys.*, 21 (7):183, August 2021. ISSN 1674-4527. doi: 10.1088/1674-4527/21/7/183. URL `http://arxiv.org/abs/2103.08136`. arXiv:2103.08136 [astro-ph].

N. Madhusudhan and S. Seager. A Temperature and Abundance Retrieval Method for Exoplanet Atmospheres. *ApJ*, 707(1):24–39, December 2009. ISSN 0004-637X, 1538-4357. doi: 10.1088/0004-637X/707/1/24. URL `http://arxiv.org/abs/0910.1347`. arXiv:0910.1347 [astro-ph].

Nikku Madhusudhan. Exoplanetary Atmospheres: Key Insights, Challenges and Prospects. *Annu. Rev. Astron. Astrophys.*, 57(1):617–663, August 2019. ISSN 0066-4146, 1545-4282. doi: 10.1146/annurev-astro-081817-051846. URL `http://arxiv.org/abs/1904.03190`. arXiv:1904.03190 [astro-ph].

Shunde Mao and Bohdan Paczynski. Gravitational microlensing by double stars and planetary systems. *ApJ*, 374:L37, June 1991. ISSN 0004-637X, 1538-4357. doi: 10.1086/186066. URL `http://adsabs.harvard.edu/doi/10.1086/186066`.

C. Matzler and J. Morland. Refined Physical Retrieval of Integrated Water Vapor and Cloud Liquid for Microwave Radiometer Data. *IEEE Trans. Geosci. Remote Sensing*, 47(6):1585–1594, June 2009. ISSN 0196-2892, 1558-0644. doi: 10.1109/TGRS.2008.2006984. URL `http://ieeexplore.ieee.org/document/4760271/`.

Thomas G. Mayerhöfer, Susanne Pahlow, and Jürgen Popp. The Bouguer-Beer-Lambert Law: Shining Light on the Obscure. *ChemPhysChem*, 21(18):2029–2046, September 2020. ISSN 1439-4235, 1439-7641. doi: 10.1002/cphc.202000464. URL `https://onlinelibrary.wiley.com/doi/10.1002/cphc.202000464`.

Michel Mayor and Didier Queloz. A Jupiter-mass companion to a solar-type star. *Nature*, 378 (6555):355–359, November 1995. ISSN 0028-0836, 1476-4687. doi: 10.1038/378355a0. URL `https://www.nature.com/articles/Art1`.

Tsevi Mazeh, Omer Tamuz, and Shay Zucker. The Sys-Rem Detrending Algorithm: Implementation and Testing, December 2006. URL `http://arxiv.org/abs/astro-ph/0612418`. arXiv:astro-ph/0612418.

D. B. McLaughlin. Some results of a spectrographic study of the Algol system. *ApJ*, 60:22, July 1924. ISSN 0004-637X, 1538-4357. doi: 10.1086/142826. URL `http://adsabs.harvard.edu/doi/10.1086/142826`.

Jordi Miralda-Escude. Orbital Perturbations of Transiting Planets: A Possible Method to Measure Stellar Quadrupoles and to Detect Earth-Mass Planets. *ApJ*, 564(2):1019–1023, January 2002. ISSN 0004-637X, 1538-4357. doi: 10.1086/324279. URL `https://iopscience.iop.org/article/10.1086/324279`.

G. Morello, A. Tsiaras, I. D. Howarth, and D. Homeier. High-precision Stellar Limb-darkening in Exoplanetary Transits. *AJ*, 154(3):111, August 2017. ISSN 1538-3881. doi: 10.3847/1538-3881/aa8405. URL `https://iopscience.iop.org/article/10.3847/1538-3881/aa8405`.

Fionn Murtagh and André Heck. *Multivariate Data Analysis*, volume 131 of *Astrophysics and Space Science Library*. Springer Netherlands, Dordrecht, 1987. ISBN 978-90-277-2426-7 978-94-009-3789-5. doi: 10.1007/978-94-009-3789-5. URL `https://link.springer.com/10.1007/978-94-009-3789-5`.

R. E. Neale, P. W. Barnes, T. M. Robson, P. J. Neale, C. E. Williamson, R. G. Zepp, S. R. Wilson, S. Madronich, A. L. Andrady, A. M. Heikkilä, G. H. Bernhard, A. F. Bais, P. J. Aucamp, A. T. Banaszak, J. F. Bornman, L. S. Bruckman, S. N. Byrne, B. Foereid, D.-P. Häder, L. M. Hollestein, W.-C. Hou, S. Hylander, M. A. K. Jansen, A. R. Klekociuk, J. B. Liley, J. Longstreth, R. M. Lucas, J. Martinez-Abaigar, K. McNeill, C. M. Olsen, K. K. Pandey, L. E. Rhodes, S. A. Robinson, K. C. Rose, T. Schikowski, K. R. Solomon, B. Sulzberger, J. E. Ukpebor, Q.-W. Wang, S.-Å. Wängberg, C. C. White, S. Yazar, A. R. Young, P. J. Young, L. Zhu, and M. Zhu. Environmental effects of stratospheric ozone depletion, UV radiation, and interactions with climate change: UNEP Environmental Effects Assessment Panel, Update 2020. *Photochem Photobiol Sci*, 20(1):1–67, January 2021. ISSN 1474-905X, 1474-9092. doi: 10.1007/s43630-020-00001-x. URL `https://link.springer.com/10.1007/s43630-020-00001-x`.

J. David Neelin, Cristian Martinez-Villalobos, Samuel N. Stechmann, Fiaz Ahmed, Gang Chen, Jesse M. Norris, Yi-Hung Kuo, and Geert Lenderink. Precipitation Extremes and Water Vapor: Relationships in Current Climate and Implications for Climate Change. *Curr Clim Change Rep*, 8(1):17–33, February 2022. ISSN 2198-6061. doi: 10.1007/s40641-021-00177-z. URL `https://link.springer.com/10.1007/s40641-021-00177-z`.

Hieu Nguyen, Jaehoon Jung, Jungbin Lee, Sung-Uk Choi, Suk-Young Hong, and Joon Heo. Optimal Atmospheric Correction for Above-Ground Forest Biomass Estimation with the ETM+ Remote Sensor. *Sensors*, 15(8):18865–18886, July 2015. ISSN 1424-8220. doi: 10.3390/s150818865. URL `http://www.mdpi.com/1424-8220/15/8/18865`.

A. E. Niell, A. J. Coster, F. S. Solheim, V. B. Mendes, P. C. Toor, R. B. Langley, and C. A. Upham. Comparison of Measurements of Atmospheric Wet Delay by Radiosonde, Water Vapor Radiometer, GPS, and VLBI. *J. Atmos. Oceanic Technol.*, 18(6):830–850, June 2001. ISSN 0739-0572, 1520-0426. doi: 10.1175/1520-0426(2001)018⟨0830:COMOAW⟩2.0.CO;2. URL `http://journals.ametsoc.org/doi/10.1175/1520-0426(2001)018<0830:COMOAW>2.0.CO;2`.

S. Noll, W. Kausch, M. Barden, A. M. Jones, C. Szyszka, S. Kimeswenger, and J. Vinther. An atmospheric radiation model for Cerro Paranal: I. The optical spectral range. *A&A*, 543:A92, July 2012. ISSN 0004-6361, 1432-0746. doi: 10.1051/0004-6361/201219040. URL `http://www.aanda.org/10.1051/0004-6361/201219040`.

M. Oshagh, A. H. M. J. Triaud, A. Burdanov, P. Figueira, A. Reiners, N. C. Santos, J. Faria, G. Boue, R. F. Diaz, S. Dreizler, S. Boldt, L. Delrez, E. Ducrot, M. Gillon, A. Guzman

Mesa, E. Jehin, S. Khalafinejad, S. Kohl, L. Serrano, and S. Udry. Activity induced variation in spin-orbit angles as derived from Rossiter-McLaughlin measurements. *A&A*, 619:A150, November 2018. ISSN 0004-6361, 1432-0746. doi: 10.1051/0004-6361/201833709. URL `http://arxiv.org/abs/1809.01027`. arXiv:1809.01027 [astro-ph].

Leonardo A. Paredes, Todd J. Henry, Samuel N. Quinn, Douglas R. Gies, Rodrigo Hinojosa-Goñi, Hodari-Sadiki James, Wei-Chun Jao, and Russel J. White. The Solar Neighborhood XLIX: Nine Giant Planets Orbiting Nearby K Dwarfs, and the CHIRON Spectrograph's Radial Velocity Performance. *AJ*, 162(5):176, November 2021. ISSN 0004-6256, 1538-3881. doi: 10.3847/1538-3881/ac082a. URL `http://arxiv.org/abs/2111.15028`. arXiv:2111.15028 [astro-ph].

Vivienne H. Payne, Eli J. Mlawer, Karen E. Cady-Pereira, and Jean-Luc Moncet. Water Vapor Continuum Absorption in the Microwave. *IEEE Trans. Geosci. Remote Sensing*, 49(6): 2194–2208, June 2011. ISSN 0196-2892, 1558-0644. doi: 10.1109/TGRS.2010.2091416. URL `http://ieeexplore.ieee.org/document/5680661/`.

Francesco Pepe, Didier Queloz, and Michel Mayor. Search and Characterization of Extrasolar Planets Using VLT/VLTI Instrumentation. In Jacqueline Bergeron and Guy Monnet, editors, *Scientific Drivers for ESO Future VLT/VLTI Instrumentation*, pages 334–339, Berlin, Heidelberg, 2002. Springer Berlin Heidelberg. ISBN 978-3-662-43215-0.

M. A. C. Perryman. *The exoplanet handbook*. New York : Cambridge University Press, Cambridge, first paperback edition edition, 2014. ISBN 978-1-107-66856-0 978-0-521-76559-6.

George M. Phillips. *Interpolation and approximation by polynomials*. Number 14 in CMS books in mathematics. Springer, New York, NY, softcover repr. of the hardcover 1. ed edition, 2011. ISBN 978-1-4419-1810-9.

Ulrich Platt and Jochen Stutz. *Differential Optical Absorption Spectroscopy*. Physics of Earth and Space Environments. Springer Berlin Heidelberg, Berlin, Heidelberg, 2008. ISBN 978-3-540-21193-8 978-3-540-75776-4. doi: 10.1007/978-3-540-75776-4. URL `http://link.springer.com/10.1007/978-3-540-75776-4`.

Robin M. Pope and Edward S. Fry. Absorption spectrum (380–700 nm) of pure water II Integrating cavity measurements. *Appl. Opt.*, 36(33):8710, November 1997. ISSN 0003-6935, 1539-4522. doi: 10.1364/AO.36.008710. URL `https://opg.optica.org/abstract.cfm?URI=ao-36-33-8710`.

René Preusker, Cintia Carbajal Henken, and Jürgen Fischer. Retrieval of Daytime Total Column Water Vapour from OLCI Measurements over Land Surfaces. *Remote Sensing*, 13(5):932, March 2021. ISSN 2072-4292. doi: 10.3390/rs13050932. URL `https://www.mdpi.com/2072-4292/13/5/932`.

David A Randall, Richard A Wood, Sandrine Bony, Robert Colman, Thierry Fichefet, John Fyfe, Vladimir Kattsov, Andrew Pitman, Jagadish Shukla, Jayaraman Srinivasan, Ronald J Stouffer, Akimasa Sumi, Karl E Taylor, K AchutaRao, R Allan, A Berger, H Blatter, C Bon, C Bretherton, A Broccoli, V Brovkin, P Dirmeyer, C Doutriaux, H Drange, A Frei, A Ganopolski, P Gent, P Gleckler, H Goosse, R Graham, J M Gregory, R Gudgel, A Hall, S Hallegatte, H Hasumi, A Henderson-Sellers, H Hendon, K Hodges, M Holland, A A M Holtslag, E Hunke, P Huybrechts, W Ingram, F Joos, B Kirtman, S Klein, R Koster, P Kushner, J Lanzante, M Latif, T Pavlova, Russian Federationi, V Petoukhov, T Phillips, S Power, S Rahmstorf, S C B Raper, H Renssen, D Rind, M Roberts, A Rosati, A Schmittner, J Scinocca, D Seidov, A G Slater, J Slingo, D Smith, B Soden, W Stern, D A Stone, K Sudo, T Takemura, G Tselioudis, M Webb, M Wild, Elisa Manzini, Taroh Matsuno, and Bryant McAvaney. Climate Models

and Their Evaluation. *ClimateChange2007:ThePhysicalScienceBasis.Contributionof Working-GroupItotheFourthAssessmentReportoftheIntergovernmentalPanelonClimateChange*, Cambridge University Press, Cambridge, United Kingdom and New York, NY, USA., 2007.

M. Rast, J. L. Bezy, and S. Bruzzi. The ESA Medium Resolution Imaging Spectrometer MERIS a review of the instrument and its mission. *International Journal of Remote Sensing*, 20(9): 1681–1702, January 1999. ISSN 0143-1161, 1366-5901. doi: 10.1080/014311699212416. URL `https://www.tandfonline.com/doi/full/10.1080/014311699212416`.

Timo Reinhold, Alexander I. Shapiro, Sami K. Solanki, Benjamin T. Montet, Nathalie A. Krivova, Robert H. Cameron, and Eliana M. Amazo-Gomez. The Sun is less active than other solar-like stars. *Science*, 368(6490):518–521, May 2020. ISSN 0036-8075, 1095-9203. doi: 10.1126/science.aay3821. URL `http://arxiv.org/abs/2005.01401`. arXiv:2005.01401 [astro-ph].

M. A. Richards, Jim Scheer, William A. Holm, and William L. Melvin, editors. *Principles of modern radar*. SciTech Pub, Raleigh, NC, 2010. ISBN 978-1-891121-52-4 978-1-891121-53-1 978-1-891121-54-8 978-1-61353-201-0.

Philip W. Rosenkranz. Water vapor microwave continuum absorption: A comparison of measurements and models. *Radio Sci.*, 33(4):919–928, July 1998. ISSN 00486604. doi: 10.1029/98RS01182. URL `http://doi.wiley.com/10.1029/98RS01182`.

Lee J. Rosenthal, Benjamin J. Fulton, Lea A. Hirsch, Howard T. Isaacson, Andrew W. Howard, Cayla M. Dedrick, Ilya A. Sherstyuk, Sarah C. Blunt, Erik A. Petigura, Heather A. Knutson, Aida Behmard, Ashley Chontos, Justin R. Crepp, Ian J. M. Crossfield, Paul A. Dalba, Debra A. Fischer, Gregory W. Henry, Stephen R. Kane, Molly Kosiarek, Geoffrey W. Marcy, Ryan A. Rubenzahl, Lauren M. Weiss, and Jason T. Wright. The California Legacy Survey I. A Catalog of 178 Planets from Precision Radial Velocity Monitoring of 719 Nearby Stars over Three Decades. *ApJS*, 255(1):8, July 2021. ISSN 0067-0049, 1538-4365. doi: 10.3847/1538-4365/abe23c. URL `http://arxiv.org/abs/2105.11583`. arXiv:2105.11583 [astro-ph].

R. A. Rossiter. On the detection of an effect of rotation during eclipse in the velocity of the brigher component of beta Lyrae, and on the constancy of velocity of this system. *ApJ*, 60:15, July 1924. ISSN 0004-637X, 1538-4357. doi: 10.1086/142825. URL `http://adsabs.harvard.edu/doi/10.1086/142825`.

L.S. Rothman, I.E. Gordon, A. Barbe, D.Chris Benner, P.F. Bernath, M. Birk, V. Boudon, L.R. Brown, A. Campargue, J.-P. Champion, K. Chance, L.H. Coudert, V. Dana, V.M. Devi, S. Fally, J.-M. Flaud, R.R. Gamache, A. Goldman, D. Jacquemart, I. Kleiner, N. Lacome, W.J. Lafferty, J.-Y. Mandin, S.T. Massie, S.N. Mikhailenko, C.E. Miller, N. Moazzen-Ahmadi, O.V. Naumenko, A.V. Nikitin, J. Orphal, V.I. Perevalov, A. Perrin, A. Predoi-Cross, C.P. Rinsland, M. Rotger, M. Šimečková, M.A.H. Smith, K. Sung, S.A. Tashkun, J. Tennyson, R.A. Toth, A.C. Vandaele, and J. Vander Auwera. The HITRAN 2008 molecular spectroscopic database. *Journal of Quantitative Spectroscopy and Radiative Transfer*, 110(9-10):533–572, June 2009. ISSN 00224073. doi: 10.1016/j.jqsrt.2009.02.013. URL `https://linkinghub.elsevier.com/retrieve/pii/S0022407309000727`.

L.S. Rothman, I.E. Gordon, Y. Babikov, A. Barbe, D. Chris Benner, P.F. Bernath, M. Birk, L. Bizzocchi, V. Boudon, L.R. Brown, A. Campargue, K. Chance, E.A. Cohen, L.H. Coudert, V.M. Devi, B.J. Drouin, A. Fayt, J.-M. Flaud, R.R. Gamache, J.J. Harrison, J.-M. Hartmann, C. Hill, J.T. Hodges, D. Jacquemart, A. Jolly, J. Lamouroux, R.J. Le Roy, G. Li, D.A. Long, O.M. Lyulin, C.J. Mackie, S.T. Massie, S. Mikhailenko, H.S.P. Müller, O.V. Naumenko, A.V. Nikitin, J. Orphal, V. Perevalov, A. Perrin, E.R. Polovtseva, C. Richard, M.A.H. Smith,

E. Starikova, K. Sung, S. Tashkun, J. Tennyson, G.C. Toon, Vl.G. Tyuterev, and G. Wagner. The HITRAN2012 molecular spectroscopic database. *Journal of Quantitative Spectroscopy and Radiative Transfer*, 130:4–50, November 2013. ISSN 00224073. doi: 10.1016/j.jqsrt.2013.07.002. URL `https://linkinghub.elsevier.com/retrieve/pii/S0022407313002859`.

Tapio Schneider, Paul A. O'Gorman, and Xavier J. Levine. WATER VAPOR AND THE DYNAMICS OF CLIMATE CHANGES. *Rev. Geophys.*, 48(3):RG3001, July 2010. ISSN 8755-1209. doi: 10.1029/2009RG000302. URL `http://doi.wiley.com/10.1029/2009RG000302`.

Norbert Schorghofer. Thermodynamics of Surface-Bounded Exospheres, April 2020. URL `http://arxiv.org/abs/1810.00165`. arXiv:1810.00165 [astro-ph].

S. Seager and D. D. Sasselov. Theoretical Transmission Spectra During Extrasolar Giant Planet Transits. *ApJ*, 537(2):916–921, July 2000. ISSN 0004-637X, 1538-4357. doi: 10.1086/309088. URL `http://arxiv.org/abs/astro-ph/9912241`. arXiv:astro-ph/9912241.

Sara Seager. The future of spectroscopic life detection on exoplanets. *Proc. Natl. Acad. Sci. U.S.A.*, 111(35):12634–12640, September 2014. ISSN 0027-8424, 1091-6490. doi: 10.1073/pnas. 1304213111. URL `https://pnas.org/doi/full/10.1073/pnas.1304213111`.

Elyar Sedaghati, Ryan J. MacDonald, Núria Casasayas-Barris, H. Jens Hoeijmakers, Henri M. J. Boffin, Florian Rodler, Rafael Brahm, Matías Jones, Alejandro Sánchez-López, Ilaria Carleo, Pedro Figueira, Andrea Mehner, and Manuel López-Puertas. A Spectral Survey of WASP-19b with ESPRESSO. *Monthly Notices of the Royal Astronomical Society*, 505 (1):435–458, May 2021. ISSN 0035-8711, 1365-2966. doi: 10.1093/mnras/stab1164. URL `http://arxiv.org/abs/2103.12858`. arXiv:2103.12858 [astro-ph].

Merrill I. Skolnik, editor. *Radar handbook*. McGraw-Hill, New York, 2nd ed edition, 1990. ISBN 978-0-07-057913-2.

A. Smette, H. Sana, S. Noll, H. Horst, W. Kausch, S. Kimeswenger, M. Barden, C. Szyszka, A. M. Jones, A. Gallenne, J. Vinther, P. Ballester, and J. Taylor. Molecfit: A general tool for telluric absorption correction. I. Method and application to ESO instruments. *A&A*, 576:A77, April 2015. ISSN 0004-6361, 1432-0746. doi: 10.1051/0004-6361/201423932. URL `http://arxiv.org/abs/1501.07239`. arXiv:1501.07239 [astro-ph].

Ignas A. G. Snellen, Remco J. de Kok, Ernst J. W. de Mooij, and Simon Albrecht. The orbital motion, absolute mass, and high-altitude winds of exoplanet HD209458b. *Nature*, 465 (7301):1049–1051, June 2010. ISSN 0028-0836, 1476-4687. doi: 10.1038/nature09111. URL `http://arxiv.org/abs/1006.4364`. arXiv:1006.4364 [astro-ph].

Herschel B. Snodgrass and Roger K. Ulrich. Rotation of Doppler features in the solar photosphere. *ApJ*, 351:309, March 1990. ISSN 0004-637X, 1538-4357. doi: 10.1086/168467. URL `http://adsabs.harvard.edu/doi/10.1086/168467`.

Richard Cliffe Ssenyunzi, Bosco Oruru, Florence Mutonyi D'ujanga, Eugenio Realini, Stefano Barindelli, Giulio Tagliaferro, Axel von Engeln, and Nick van de Giesen. Performance of ERA5 data in retrieving Precipitable Water Vapour over East African tropical region. *Advances in Space Research*, 65(8):1877–1893, April 2020. ISSN 02731177. doi: 10.1016/j.asr.2020.02.003. URL `https://linkinghub.elsevier.com/retrieve/pii/S027311772030079X`.

Steven William Stahler and Francesco Palla. *The formation of stars*. Physics textbook. Wiley-VCH, Weinheim, 2004. ISBN 978-3-527-40559-6.

Keivan G. Stassun, Karen A. Collins, and B. Scott Gaudi. Accurate, Empirical Radii and Masses of Planets and their Host Stars with Gaia Parallaxes. *AJ*, 153(3):136, March 2017.

ISSN 1538-3881. doi: 10.3847/1538-3881/aa5df3. URL `http://arxiv.org/abs/1609.04389`. arXiv:1609.04389 [astro-ph].

K. G. Strassmeier, I. Ilyin, A. Järvinen, M. Weber, M. Woche, S. I. Barnes, S. M. Bauer, E. Beckert, W. Bittner, R. Bredthauer, T. A. Carroll, C. Denker, F. Dionies, I. DiVarano, D. Döscher, T. Fechner, D. Feuerstein, T. Granzer, T. Hahn, G. Harnisch, A. Hofmann, M. Lesser, J. Paschke, S. Pankratow, V. Plank, D. Plüschke, E. Popow, D. Sablowski, and J. Storm. PEPSI: The high-resolution echelle spectrograph and polarimeter for the Large Binocular Telescope. 2015. doi: 10.48550/ARXIV.1505.06492. URL `https://arxiv.org/abs/1505.06492`. Publisher: arXiv Version Number: 1.

K. G. Strassmeier, I. Ilyin, and M. Steffen. PEPSI deep spectra. I. The Sun-as-a-star. 2017. doi: 10.48550/ARXIV.1712.06960. URL `https://arxiv.org/abs/1712.06960`. Publisher: arXiv Version Number: 1.

O. Tamuz, T. Mazeh, and S. Zucker. Correcting systematic effects in a large set of photometric light curves. *Monthly Notices of the Royal Astronomical Society*, 356(4):1466–1470, February 2005. ISSN 00358711, 13652966. doi: 10.1111/j.1365-2966.2004.08585.x. URL `https://academic.oup.com/mnras/article-lookup/doi/10.1111/j.1365-2966.2004.08585.x`.

G. Torres, J. N. Winn, and M. J. Holman. Improved parameters for extrasolar transiting planets. *ApJ*, 677(2):1324–1342, April 2008. ISSN 0004-637X, 1538-4357. doi: 10.1086/529429. URL `http://arxiv.org/abs/0801.1841`. arXiv:0801.1841 [astro-ph].

Kevin E. Trenberth. Conceptual Framework for Changes of Extremes of the Hydrological Cycle with Climate Change. *Climatic Change*, 42(1):327–339, 1999. ISSN 01650009. doi: 10.1023/A:1005488920935. URL `http://link.springer.com/10.1023/A:1005488920935`.

Amaury H. M. J. Triaud. The Rossiter-McLaughlin effect in Exoplanet Research. pages 1375–1401. 2018. doi: 10.1007/978-3-319-55333-7_2. URL `http://arxiv.org/abs/1709.06376`. arXiv:1709.06376 [astro-ph].

Alessio Turchi, Elena Masciadri, Florian Kerber, and Gianluca Martelloni. Forecasting water vapour above the sites of ESO's Very Large Telescope (VLT) and the Large Binocular Telescope (LBT). *Monthly Notices of the Royal Astronomical Society*, October 2018. ISSN 0035-8711, 1365-2966. doi: 10.1093/mnras/sty2668. URL `https://academic.oup.com/mnras/advance-article/doi/10.1093/mnras/sty2668/5113488`.

S. Ulmer-Moll, P. Figueira, J. J. Neal, N. C. Santos, and M. Bonnefoy. Telluric correction in the near-infrared: Standard star or synthetic transmission? *A&A*, 621:A79, January 2019. ISSN 0004-6361, 1432-0746. doi: 10.1051/0004-6361/201833282. URL `http://arxiv.org/abs/1811.08915`. arXiv:1811.08915 [astro-ph].

William D. Vacca, Michael C. Cushing, and John T. Rayner. A Method of Correcting Near-Infrared Spectra for Telluric Absorption. *PUBL ASTRON SOC PAC*, 115(805):389–409, March 2003. ISSN 0004-6280, 1538-3873. doi: 10.1086/346193. URL `http://arxiv.org/abs/astro-ph/0211255`. arXiv:astro-ph/0211255.

Tim Van Hoolst, Lena Noack, and Attilio Rivoldini. Exoplanet interiors and habitability. *Advances in Physics: X*, 4(1):1630316, January 2019. ISSN 2374-6149. doi: 10.1080/23746149.2019.1630316. URL `https://www.tandfonline.com/doi/full/10.1080/23746149.2019.1630316`.

Francesco Vespe, Jens Wickert, Catia Benedetto, and Rosa Pacione. Derivation of the Water Vapor Content from the GNSS Radio Occultation Observations. In Christoph Reigber, Hermann
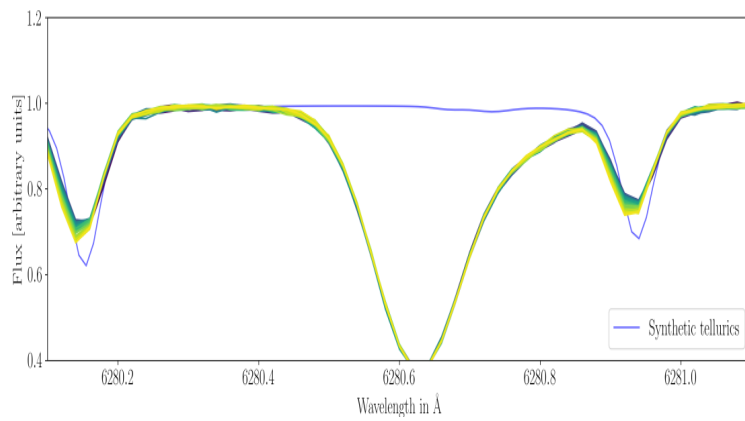
Lühr, Peter Schwintzer, and Jens Wickert, editors, *Earth Observation with CHAMP: Results from Three Years in Orbit*, pages 537–542. Springer Berlin Heidelberg, Berlin, Heidelberg, 2005. ISBN 978-3-540-26800-0. doi: 10.1007/3-540-26800-6_85. URL `https://doi.org/10.1007/3-540-26800-6_85`.

Ji Wang, Debra A. Fischer, Elliott P. Horch, and Xu Huang. ON THE OCCURRENCE RATE OF HOT JUPITERS IN DIFFERENT STELLAR ENVIRONMENTS. *ApJ*, 799 (2):229, January 2015. ISSN 1538-4357. doi: 10.1088/0004-637X/799/2/229. URL `https://iopscience.iop.org/article/10.1088/0004-637X/799/2/229`.

Shuaimin Wang, Tianhe Xu, Wenfeng Nie, Chunhua Jiang, Yuguo Yang, Zhenlong Fang, Mowen Li, and Zhen Zhang. Evaluation of Precipitable Water Vapor from Five Reanalysis Products with Ground-Based GNSS Observations. *Remote Sensing*, 12(11):1817, June 2020. ISSN 2072-4292. doi: 10.3390/rs12111817. URL `https://www.mdpi.com/2072-4292/12/11/1817`.

Derek Ward-Thompson and Anthony P. Whitworth. *An Introduction to Star Formation*. Cambridge University Press, 1 edition, February 2011. ISBN 978-0-521-63030-6 978-0-521-63967-5 978-0-511-97402-1 978-1-107-48352-1. doi: 10.1017/CBO9780511974021. URL `https://www.cambridge.org/core/product/identifier/9780511974021/type/book`.

Randolph H. Ware, David W. Fulker, Seth A. Stein, David N. Anderson, Susan K. Avery, Richard D. Clark, Kelvin K. Droegemeier, Joachim P. Kuettner, J. Bernard Minster, and Soroosh Sorooshian. SuomiNet: A Real–Time National GPS Network for Atmospheric Research and Education. *Bull. Amer. Meteor. Soc.*, 81(4):677–694, April 2000. ISSN 0003-0007, 1520-0477. doi: 10.1175/1520-0477(2000)081⟨0677:SARNGN⟩2.3.CO;2. URL `http://journals.ametsoc.org/doi/10.1175/1520-0477(2000)081<0677:SARNGN>2.3.CO;2`.

Claus Weitkamp, editor. *Lidar: range-resolved optical remote sensing of the atmosphere*. Number 102 in Springer series in optical sciences. Springer, New York, 2005. ISBN 978-0-387-40075-4.

Richard C. Willson and Hugh S. Hudson. The Sun's luminosity over a complete solar cycle. *Nature*, 351(6321):42–44, May 1991. ISSN 0028-0836, 1476-4687. doi: 10.1038/351042a0. URL `https://www.nature.com/articles/351042a0`.

Anna E. Windle, Hayley Evers-King, Benjamin R. Loveday, Michael Ondrusek, and Greg M. Silsbe. Evaluating Atmospheric Correction Algorithms Applied to OLCI Sentinel-3 Data of Chesapeake Bay Waters. *Remote Sensing*, 14(8):1881, April 2022. ISSN 2072-4292. doi: 10.3390/rs14081881. URL `https://www.mdpi.com/2072-4292/14/8/1881`.

Joshua N. Winn. Exoplanets and the Rossiter-McLaughlin Effect, December 2006. URL `http://arxiv.org/abs/astro-ph/0612744`. arXiv:astro-ph/0612744.

W. M. Wood-Vasey, Daniel Perrefort, and Ashley D. Baker. GPS Measurements of Precipitable Water Vapor Can Improve Survey Calibration: A Demonstration from KPNO and the Mayall z-band Legacy Survey. *AJ*, 163(6):283, June 2022. ISSN 0004-6256, 1538-3881. doi: 10.3847/1538-3881/ac63bb. URL `https://iopscience.iop.org/article/10.3847/1538-3881/ac63bb`.

Andrew T. Young. Rayleigh scattering. *Appl. Opt.*, 20(4):533, February 1981. ISSN 0003-6935, 1539-4522. doi: 10.1364/AO.20.000533. URL `https://opg.optica.org/abstract.cfm?URI=ao-20-4-533`.

Yinxin Zhang, Wanzhuo Li, Wenhao Duan, Zhanhua Huang, and Huaidong Yang. Echelle Grating Spectroscopic Technology for High-Resolution and Broadband Spectral Measurement. *Applied Sciences*, 12(21):11042, October 2022. ISSN 2076-3417. doi: 10.3390/app122111042. URL `https://www.mdpi.com/2076-3417/12/21/11042`.

I. Zhivanovich, A. A. Solov'ev, and V. I. Efremov. Differential Rotation of the Sun, Helioseismology Data, and Estimation of the Depth of Superconvection Cells. *Geomagn. Aeron.*, 61(7):940–948, December 2021. ISSN 0016-7932, 1555-645X. doi: 10.1134/S0016793221070264. URL `https://link.springer.com/10.1134/S0016793221070264`.

Wei Zhu and Subo Dong. Exoplanet Statistics and Theoretical Implications. *Annu. Rev. Astron. Astrophys.*, 59(1):291–336, September 2021. ISSN 0066-4146, 1545-4282. doi: 10.1146/annurev-astro-112420-020055. URL `http://arxiv.org/abs/2103.02127`. arXiv:2103.02127 [astro-ph].
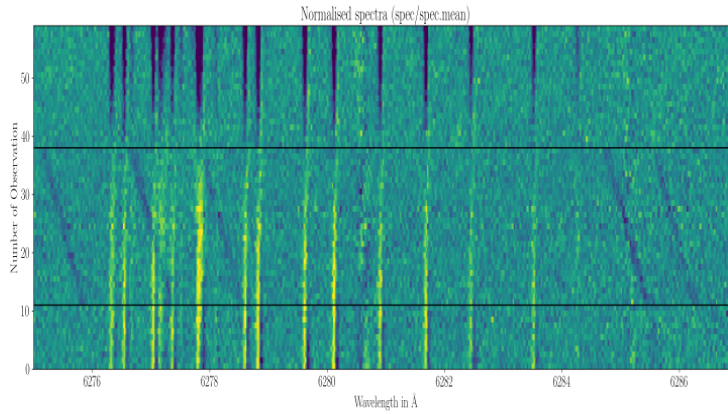
Appendix A

Appendix

A.1   PEPSI processing

A.2   Geo Analysis
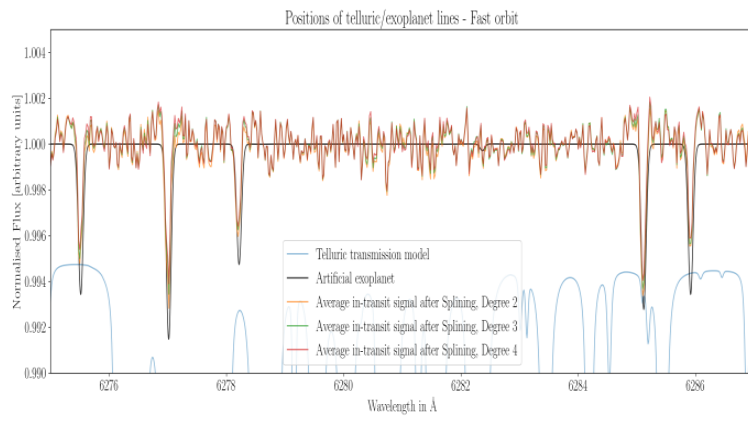
Residual Transmission Spectra - Stellar/Earth Rest Frame - First Observation

Residual Transmission Spectra - Stellar/Earth Rest Frame - Last Observation

A.3 Objective 3 Analysis

Spline normalised spectrum - Stellar Rest Frame

Splined normalised spectrum - shifted: Exoplanet Rest Frame

Normalised spectra (spec/spec.mean)
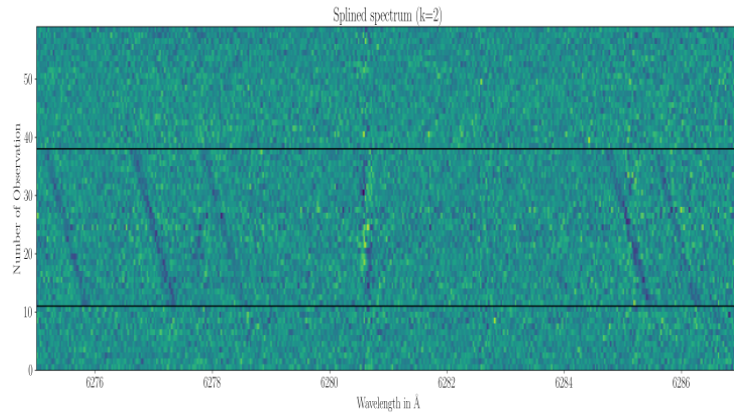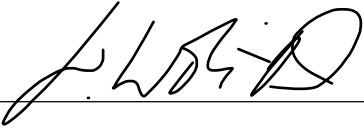
Splined spectrum (k=2)

Positions of telluric/exoplanet lines - Fast orbit
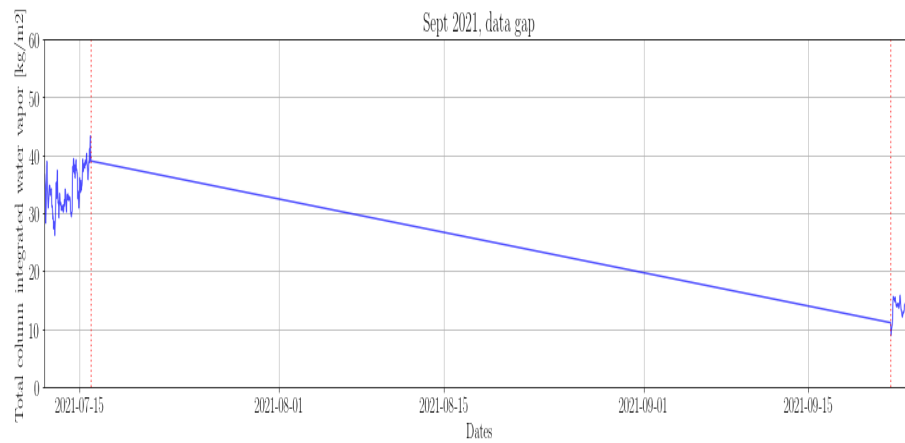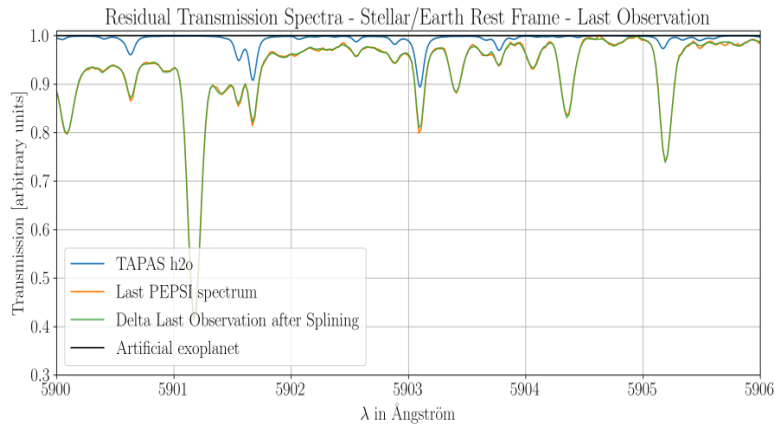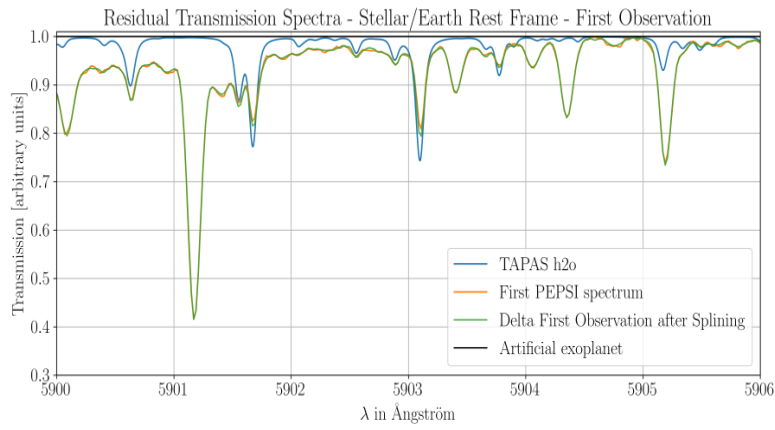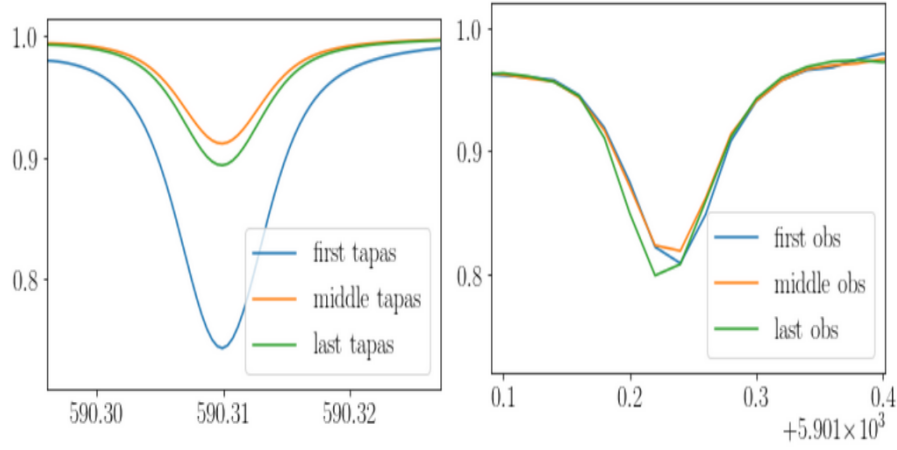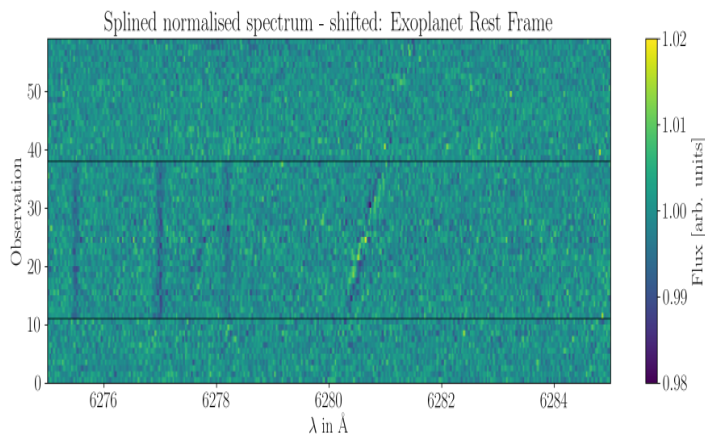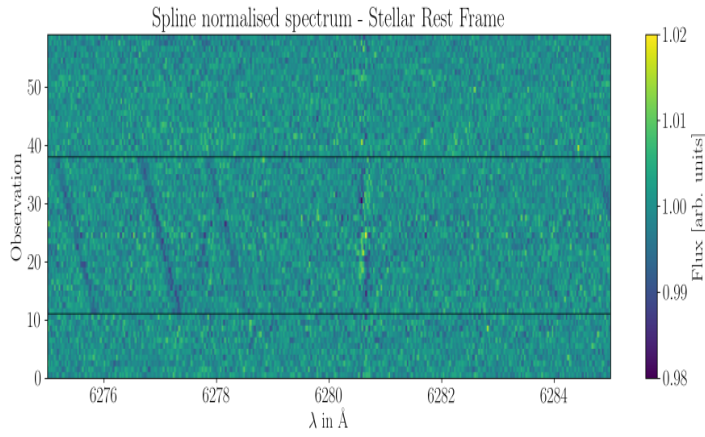
Erklärung

Ich erkläre, dass ich die vorliegende Arbeit oder Teile davon nicht für andere Prüfungs- und Studienleistungen eingereicht, selbständig und nur unter Verwendung der angegebenen Literatur und Hilfsmittel angefertigt habe. Sämtliche fremde Quellen inklusive Internetquellen, Grafiken, Tabellen und Bilder, die ich unverändert oder abgewandelt wiedergegeben habe, habe ich als solche kenntlich gemacht. Mir ist bekannt, dass Verstöße gegen diese Grundsätze als Täuschungsversuch bzw. Täuschung geahndet werden.

Joana Wokittel, Berlin, den 26.07.2023